Micromachining Metrology: Measurement and Analysis of Dynamic Tool-tip Trajectory when using Ultra-High-Speed Spindles

Submitted in partial fulfillment of the requirements for

the degree of

Doctor of Philosophy

in

Mechanical Engineering

Sudhanshu Nahata

B.Tech., Production and Industrial Engineering, Indian Institute of Technology, Delhi

Carnegie Mellon University
Pittsburgh, PA

May, 2018

To my parents,
Alka and Sanjay Kumar Nahata,
and my wife,
Priyanka Pincha

Acknowledgements

This thesis marks the completion of my journey as a graduate student, which would not have been fruitful and memorable without the help, support and inspiration of many. I wish to thank all these people who have helped me in this journey.

First and foremost, I want to express my sincere gratitude to my advisor Prof. Burak Ozdoganlar for giving me this wonderful opportunity to pursue my dreams in a state-of-the-art facility at Carnegie Mellon University. His guidance, encouragement and his commitment towards my development has been outstanding. He has been more than patient with me and has given me ample chances to correct all my mistakes. One of the most important skills that he taught me was to think out of the box and to constantly think - to come up with a variety of ideas. Many a times during our discussion, he would bring in "crazy" ideas - which sometimes would feed infeasible. The intent however, is to constantly look for solutions and never give up. He also taught me how to write complex ideas/concepts in simple and unambiguous manner. I cannot agree enough that he really knows how to bring the best out from his students.

I wish to thank Drs. Alkan Donmez and Shawn Moylan for their technical guidance on the various aspects of my research. I greatly appreciate their time in brainstorming despite their busy schedule. I have immensely benefitted from their vast experience through interactions on both metrology and additive manufacturing related work. In addition, I want to specially thank Dr. Alkan Donmez for serving as one of my committee members. His involvement has brought this work to new heights.

I wish to thank my committee members, Prof. Rahul Panat and Prof. Mark Bedillion for serving on my committee and providing helpful suggestions regarding my research and its presentation.

Although, their involvement was little late, but they brought a fresh perspective to my research. Their questions and comments has helped me refine my work and obtain an important perspective on the applicability of my research.

I wish to thank Prof. Yoosuf Picard for being a wonderful collaborator for my material science related work. He personally took time to train me on EBSD and encouraged me to participate in workshops and conferences to gain more exposure. The fruitful discussions I had with him regarding microscopy work has immensely helped me in appreciating material behavior and its properties. I also wish to thank Dr. Marzyeh Moradi for helping me with collecting EBSD data and in analyzing and forming insightful discussions.

I want to thank Jim Dillinger, John Fulmer and Ed Wojciechowski of the Mechanical Engineering machine shop for their help in training me on the machine tools and also in fabricating parts for my experimental setups. I want to specially thank Ed for listening and acting promptly to lab related issues. I want to thank Larry Hayhurst of the Chemical Engineering machine shop for helping me design and manufacture my parts for my experiments. I want to thank Tom Nuhfer and William Pingitore of Material Science for their assistance in various microscopy techniques and sample preparation. I want to thank Bobbi Kostyak, Ginny Barry, and Chris Hertz of Mechanical Engineering for their assistance in purchasing and administrative issues.

I wish to thank the lab veterans Nithyanand Kota, Prashanth Anandan, Arda Gozen and Bekir Bediz for guiding me in various aspects of the lab work. A special thanks to Emrullah Korkmaz for a great company over the past seven years and his eagerness to participate in discussions and guiding me on numerous occasions. I like to extend a special thanks to Recep Onler whom I have interacted the most at MMDL. I will always cherish his support, help and encouragement which made me reach this far. I wish to thank Shivang Shekhar for bringing new ideas and fresh air during the past couple of years which certainly made me feel a little younger. I also like to thank the optical table users - Wei Chen and Shivang Shekhar - for their understanding in sharing instruments and helping each other during tedious experiments. I would also like to express my thanks to all other (past and present) members of the MMDL, Shin Hyung Song, JuEun Lee, Gerardo Salas Bolanos, Rakesh Khilwani, Pallavi Gunalan, Kadri Bugra Ozutemiz, Jonelle Yu, Ezgi Pinar Yalcintas, Toygun Cetinkaya, Ant Yucesoy, Lisha White, Elaine Sung, Yusuf Mert, Ali Alp Gurer, Bin Shen, H. Sinan Bank, Bohan Hao, Hao Li and Muneeb Hai for their friendship and help throughout my Ph.D.

My stay in Pittsburgh has been wonderful and enjoyable in the company of many many friends. Their support and care helped me enjoy life outside or work, overcome setbacks and stay focused on my graduate study. A very special thanks to the "chai club" consisting of Lakshminarayan

Ramasubramanian, Prince Singh, Shivang Shekhar and myself - where we discussed from philosophy to politics to sports to academics to basically everything. I wish to thank my MechE friends Ramesh Shreshta, Changho Oh, Mabaran Rajaraman, Ankit Jain, Arjun Kumar, Deepak Patil, Prathamesh Desai, Wee-Liat Ong, Sneha Narra, Colt Montgomery, Patcharapit Promoppatum, Shraddha Joshi and many more for great discussions and helping me out with many things. I wish to thank the past members of Indian Graduate Student Association for a fun filled social life. I wish to thank my squash coach Vivek Seshadri for teaching me some of the key techniques which helped me improve my skills and appreciate the sport better. I like to thank my amazing flat-mate Matharishwan Naganbabu for a wonderful company and tolerating me for more than five years and teaching me stellar baking skills which I will always cherish. I would like to thank my friends Varoon Shankar, Rohit Padmanabhan, Harsh Ghesani, Jay Nahata, Payas Gupta, Manu Nahar, Vaibhav Agrawal, Ankita Mangal, Arka Prabha Roy, Pratiti Mandal, Hardik Shah, Anurag Jakhotia, Shashank Sharma, Sudipto Mandal, Ashwati Krishnan, Divya Sharma, Divya Hariharan, Niranjani Rajagopalan, Sumon Chatterjee and many more who made my stay at Pittsburgh lively and happening.

I am forever indebted to my parents Alka and Sanjay Kumar Nahata, my brother Himanshu Nahata, and my wife Priyanka Pincha for their constant love and encouragement throughout my life. Without their countless sacrifices towards my education and career, this journey would not have been possible. Without my wife's diligent support, sacrifices, love, encouragement and understanding during the past three years, it would have been much more difficult to complete my thesis. I would like to especially thank her for tolerating me during these years. I would like to thank my in-laws for a greater understanding and believing in me and my dreams. I wish to thank my batchmates from IITD a.k.a. my “family” in the States - Harshit Sodhani and Pratik Mital for standing by me during all times. I greatly value their friendship and feel lucky to have them by my side. I would also like to thank all my relatives and friends back home for their understanding, love and support.

Lastly, I would like to greatly acknowledge the financial support of the National Institute of Standards and Technology (70NANB12H208), Research for Advanced Manufacturing in Pennsylvania (RAMP), America Makes (FA8650-12-2-7230) and National Science Foundation Student Travel Awards.

Abstract

There is a growing demand for miniature, high-precision components and devices with micro-scale features for applications in biomedical systems, aerospace structures, and energy storage/conversion systems. Mechanical micromachining has become a leading approach to address this demand. In micromachining, a micro-scale cutting tool, such as a micro-endmill with a diameter as small as 10 μm, is rotated by an ultra-high-speed (UHS) spindle (speeds greater than 60,000 rpm, reaching up to 500,000 rpm) to mechanically remove the material from a workpiece. Although micromachining resembles the traditional computer numerically controlled (CNC) machining processes, the micron-scale cutting tools, ultra-high-speed (UHS) spindles, and considerably tighter tolerance requirements bring unique challenges to micromachining.

A specific challenge related to the process accuracy and reproducibility is the characterization of the non-ideal motions of the micro-tool tip when rotated using UHS spindles. The tool tip trajectory dictates both the dimensional accuracy and the surface roughness of micromachined features, and thus, must be well-characterized to satisfy the stringent quality requirements. The deviation of the tool tip trajectory from the ideal trajectory arises from (1) geometric errors of the micro-tools; (2) imperfect interfaces within the tool-collet-spindle assembly (resulting in setup errors); (3) manufacturing errors of the spindle (imperfect bearings, non-straightness of the spindle shaft); (4) the changes in spindle's structure (deflections) and bearing preloads when forces from machining are in effect; and (5) vibrations caused by the system components or environmental effects. Although many works in the literature have addressed the aforementioned aspects towards understanding the errors in tool-tip trajectory for *macro-scale machining processes*, very limited effort has been devoted to addressing those for *micromachining* with its unique challenges. As such, a comprehensive understanding of tool-tip error motions and their effect on dimensional and

surface quality parameters in micromachining is still lacking.

To address this need, ***the objective of this doctoral research*** is to develop experimental methods and the associated analysis tools to characterize the non-ideal motions of the tool tip, as well as to evaluate the impact of those motions on dimensional and surface quality of micromachined features. The non-ideal tool tip trajectory is described by the *radial throw*, which refers to the radial motions of the tool axis as well as those reflected at the individual cutting edges of the tool. We address our research objective through four thrust areas: (1) Development and evaluation of a measurement approach to characterize the spindle-speed-dependent radial throw when using an UHS spindle; (2) Characterization of changes in radial throw under static loading of the UHS spindle; (3) Development of a measurement approach and a statistical characterization of geometric errors of micro-tools; and (4) Development of a simulation tool to determine the effect of radial throw on the dimensional and surface quality of the micromachined features. Each of these thrust areas are briefly described below.

First, a measurement approach to obtain magnitude and orientation of radial throw *at the tool-tip* is developed. The approach involves measuring the radial throw using laser Doppler vibrometers (LDVs) from two axial locations on *the tool shank* at a given spindle speed, and then using a vectorial approach to calculate the radial throw at each cutting point along the cutting edges of the micro-tool. To this end, a method to relate the orientation of radial throw with respect to the cutting edges of the microtool is devised. The developed approach is experimentally validated by comparing predicted and measured radial throw at the tip of a custom-fabricated microtool blank. Following the validation, radial throw at tool-tip for a commercial microtool is experimentally studied for a range of operating conditions, *viz.*, varying spindle speeds, tool attachment/detachment cycles, and thermal cycling of the spindle. The uncertainty of the approach is also evaluated through a statistical analysis. Finally, an approach to relate the speed dependence of radial throw to the dynamic response of the spindle is proposed and demonstrated.

Second, the changes in radial throw arising from static loading of the spindle is studied. It is well known that loads applied on a spindle can alter its motion and error characteristics. Since such loads are present in micromachining processes (thrust and radial forces), understanding the changes in radial throw arising from axial and radial loading of the spindle is important. To this end, we created an experimental facility, where radial and axial loads are applied to the spindle using permanent magnets, which enable providing controlled and repeatable forces to the spindle in a non-contact fashion. To aid in selection of magnet type, dimensions and its placement, a finite-element based model of magnet-to-magnet and magnet-to-artifact interactions is developed in COMSOL Multiphysics and experimentally validated. The effect of external loading on all frequency components of radial throw (i.e., fundamental, synchronous and asynchronous) are studied.

The results are presented in both the time and the frequency domain.

Third, a metrology approach to assess the geometric errors of microtools is developed and demonstrated. The geometric errors of microtools, particularly the misalignment between the shank and tool-tip axis and inaccuracies of the positions of cutting edges, directly affect the tool-tip motions. An optical approach including high-magnification objectives and high-resolution rotary states is used for measuring tool geometry in three-dimensions. Novel measurement approaches and post-processing techniques are developed to measure the geometric axis of the tool-shank and the axis-offset between the shank and the fluted region of the microtool.

And ***fourth***, results from different error sources are combined to obtain the total radial throw, and its effects on dimensional and surface quality parameters of the micromachined features are studied through numerical simulations. A three-dimensional tool model (with geometric errors) is considered, where the radial throw is calculated and added at each axial location to accurately represent the trajectory of the cutting edges. The magnitude and orientation of radial throw is varied (corresponding to experimental observations) to evaluate its effects on peripheral (sidewall) surface roughness, dimensional errors and changes in the uncut chip thickness.

Contents

List of Figures

List of Tables

CHAPTER 1

Introduction

This chapter introduces the thesis by presenting the research motivation. The subsequent section provides a brief background on the radial throw and its components, per ISO 230-7:2015. This is followed by a brief overview of the literature on (a) the measurement of radial throw/run-out when using miniature ultra-high-speed (UHS) spindles, (b) the measurement of spindle error motions in UHS spindles, and (c) the evaluation of manufacturing errors in micro-tools, is presented. Lastly, research objectives for the thesis work are outlined followed by research contributions.

1.1 Research Motivation

Mechanical micromachining processes, such as micromilling, have been increasingly used by many industries to manufacture meso- and micro-scale parts and devices with three-dimensional (3D) micro-scale features [1–4]. In micromachining, micro-scale (as small as 10 μm in diameter) cutting tools are used to create the features on high precision miniature machine tools (MMTs) (see Fig. 1.1(a)-(d)). MMTs are commonly equipped with an ultra-high speed (UHS) spindle (>60,000 revolutions per minute) to attain the effective material removal rates while using micron-scale tooling (see Fig. 1.1(e)). Although micromachining is perceived as a scaled-down version of conventional machining, the smaller cutting tools and higher spindle speeds bring critical and unique challenges to application of micromachining .

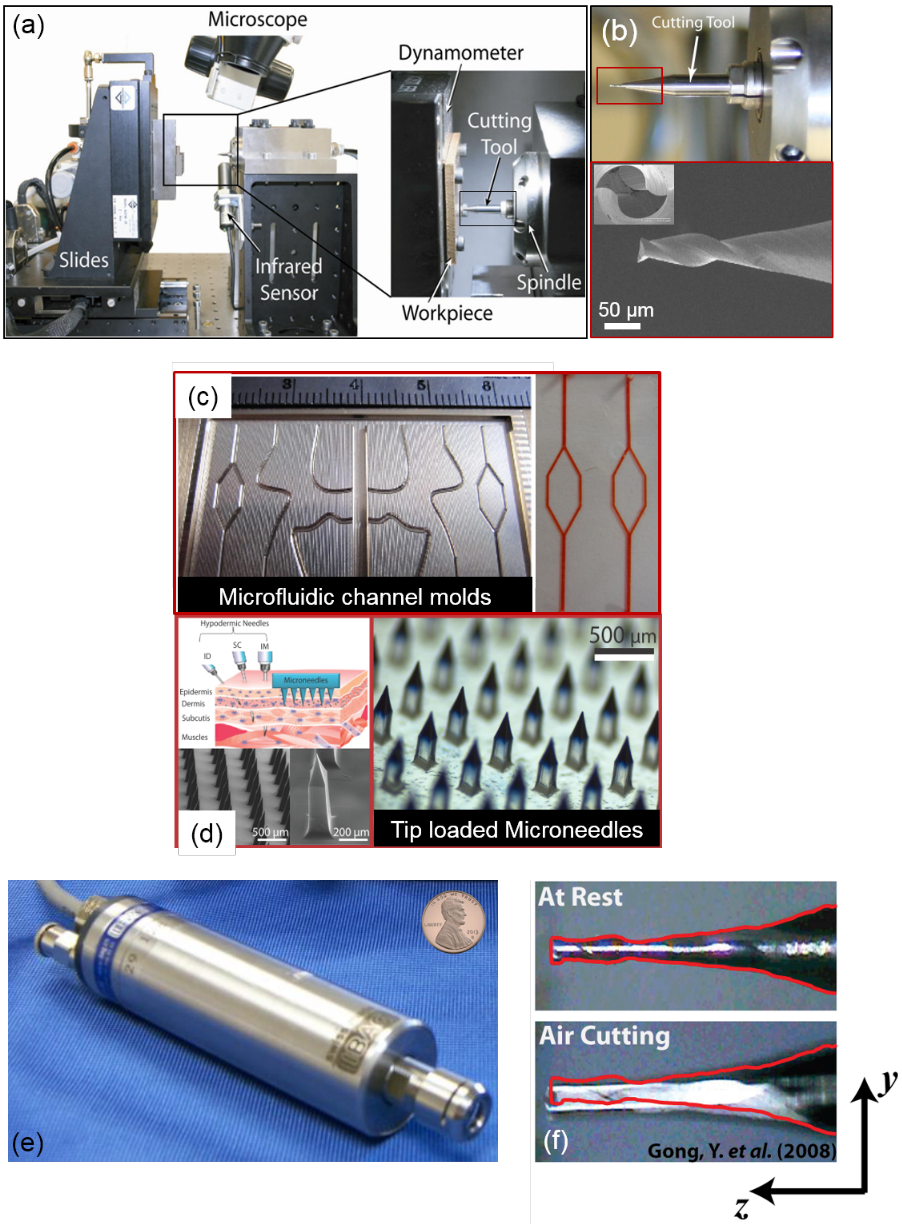

Figure 1.1: *A miniature machine tool (MMT): (a) the physical setup [5], (b) a micro-endmill, (c and d) parts fabricated with MMT [6], (e) an ultra-high-speed spindle [7], and (f) the tool-tip during rotation of the spindle [8].*

Absolute tolerance requirements for micromachining processes are very strict due to micron-scale dimensions of the fabricated features. One of the key issues that affects the accuracy of a micromachining process is the unideal trajectory of the cutting edges at the tool tip (see Fig. 1.1(f)). The motion at the cutting edges of the tools rotated in the UHS spindles is highly correlated with the attainable dimensional accuracy and surface roughness, as well as with the cutting forces [9]. One of the major contributors to dimensional/form errors and surface roughness of the micromachined features is the radial throw of tool-axis. In contrast to *run-out*, which is the total displacement of a rotating surface within a full rotation at a given axial location along a given direction (as described in [10]), *radial throw of an axis* depends on the rotational angle and indicates the instantaneous position of geometric axis at a given axial location [10].

The radial throw (of tool axis) translates to each cutting point of the micro-tool through an orientation angle, and causes the deviation of the trajectory of that cutting point from the ideal trajectory (i.e., a circular trajectory with a diameter equal to the tool diameter at that cutting point). In micromachining, the magnitude of radial throw can be commensurate with the prescribed feed value. Hence, in addition to impacting practical aspects of dimensional, form, and surface accuracy, radial throw also alters the instantaneous chip thickness significantly [9], and thus, is critical for process-modeling efforts. However, accurate determination of radial throw at the cutting points is very challenging due to the micron-scale tool dimensions and high rotational speeds used in micromachining processes.

The effect of radial throw can be seen via the output quality of the micromachined components and the resulting tool-wear. Figure 1.2 presents the motion at the tip of a micro-tool during a slot milling operation. In the ideal case, the cutter produces a trajectory with a diameter equal to the tool-diameter (Fig. 1.2(a)-(c)). However, in the presence of radial throw, the trajectory is altered and in consequence, one cutting edge participates more than the other (see Fig. 1.2(d)-(f)). This is further highlighted by comparing the machined slots with a simulation, and also confirmed by the one-sided tool wear. In this case, an average radial throw of 10 μm could introduce a 17.75 μm dimensional error in the machined part, apart from affecting the resulting surface quality.

The deviation of the trajectory of a cutting point from its ideal trajectory results from both the kinematic and dynamic errors [10, 11]. The kinematic errors arise from the geometric inaccuracies of the tool-collet-spindle assembly, as well as of the interfaces between the components of the assembly. When measured at low rotational speeds, the radial throw only reflects those geometric inaccuracies. On the other hand, dynamic errors arise from the rotation of the spindle (i.e., spindle error motions) and associated dynamic response (i.e., rotating unbalance and the associated dynamic response of the assembly), thereby rendering the radial throw speed-dependent [12]. Furthermore, since the dynamic behavior of the assembly is not axisymmetric at every frequency

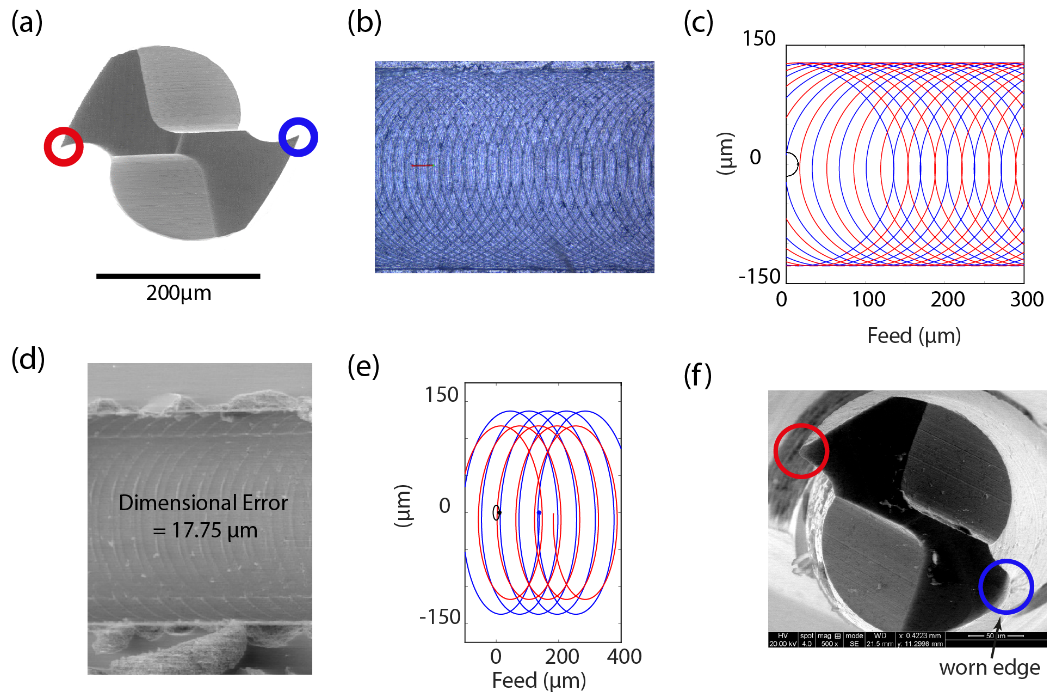

Figure 1.2: *Machining (feed) marks and the associated tool wear: (a) an unused micro-endmill, (b)-(c) feed marks without radial throw, (d)-(e) feed marks showing greater participation of one cutting edge, and (f) one-sided tool wear.*

(i.e., it is not identical in two mutually-perpendicular directions), the form of the radial throw will deviate from a circular trajectory at those frequencies [11–13]. As a result, for UHS micromachining processes, the radial throw must be measured at different spindle speeds simultaneously along two mutually-perpendicular directions, and the contributions to the radial throw from the tool-collet-spindle assembly and the dynamic response should be understood. As such, novel measurement and analysis approaches are needed to quantify the kinematic and the dynamic errors to fully understand the dynamic tool-tip trajectory (i.e., speed-dependent radial throw) when using ultra-high-speed spindles.

The trajectory of cutting points also deviate from the ideal when the tool-collet-spindle assembly experiences external load during micromachining . Such loads (or forces) are applied in both the thrust (axial) and the radial directions. Accordingly, to understand the changes in radial throw arising from axial and radial loading of the spindle, measurements must be conducted both with and without loading.

In addition to the external loads, any inaccuracies in the geometry of a micro-tool, particularly the misalignment between the shank and tool-tip axis, directly alters the resulting trajectory of the cutting points. Therefore, the micro-cutting tools must be characterized for geometric inaccuracies that affect the trajectory of the cutting points.

To summarize, to gain a complete understanding of the dynamic tool-tip trajectory, novel measurement and analysis approaches are required to obtain the speed-dependent radial throw, both with the without forces along with the tool-geometry errors. Furthermore, their effects on the resulting dimensional accuracy, sidewall surface roughness and changes in the uncut chip thickness should be quantified.

1.2 Background

In this section, we review the definition of the *radial throw of tool axis* and how it is different from the traditionally *run-out* definition. Further, the radial throw is divided into various components and a review of the terminology used to classify them is presented. This classification is conducted in both the angular and the frequency domain for complete understanding. The frequencies are typically specified as undulations per revolution (UPR) [14] for rotational systems (i.e., rotational or fundamental frequency = 1 UPR etc.).

To describe the radial throw of the tool axis, first, an *axis average line* is defined. The axis average line is defined as a straight line segment representing the average location of the axis of rotation over one of more revolutions [10]. An xyz cartesian reference frame is set up such that the z axis coincides with the axis average line. Motions perpendicular to the z-axis (i.e., motions projected to the $x-y$ plane) are defined as radial motions. According to the ISO standards [10], *radial throw of a rotary axis at a given point* is defined as the "distance between the geometric axis of a part (or test artifact) connected to a rotary axis and the axis average line, when the two axes do not coincide." This is further explained using Figure 1.3.

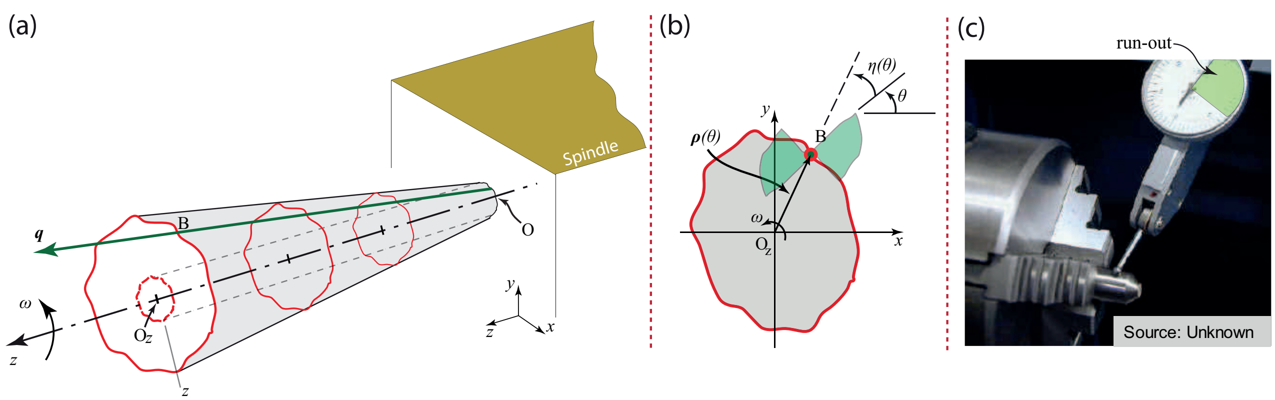

Figure 1.3: *Difference between the radial throw of tool axis and the run-out is highlighted: (a) 2D trajectory of radial throw at various* $x-y$ *planes, (b) radial throw magnitude* $\boldsymbol{\rho}(\theta)$ *and orientation* $\eta(\theta)$*, and (c) a sample run-out measurement.*

Figure 1.3(a) describes a tool-axis $\boldsymbol{q}$ rotated along an axis Oz. Ideally, the tool-axis coincides with the rotation axis; presence of radial throw causes the tool-axis to deviate from its ideal position. The instantaneous position of tool-axis at a particular $x - y$ plane is described by a vector O_zB in Fig. 1.3(b). This instantaneous vector is termed as radial throw of tool-axis, and is a function of rotation angle θ.

Where radial throw $\boldsymbol{\rho} = \boldsymbol{\rho}(\theta)$ provide instantaneous trajectory of the tool axis (i.e., it depends on the rotational angle θ), run-out (or equivalently the total indicator reading (TIR)) is limited to a single value representing the peak-to-peak amplitude of the motions sensed by an indicator, and along a specific direction during one or more revolutions of the spindle (see Fig. 1.3(c)). Therefore, analysis of the trajectory at the tool-tip is best conducted through determination of the radial throw.

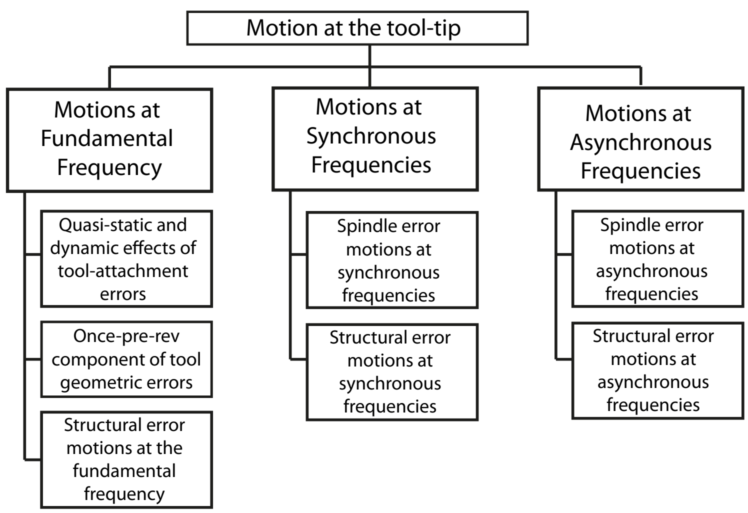

Figure 1.4: *Motion at the tool-tip and its components at various frequencies.*

The radial throw (of tool axis) at the tool tip can be divided into different frequency components. Such a classification is presented in Fig. 1.4 by means of a flowchart. This flowchart is supported by a schematic diagram in Fig 1.5 representing an average motion (or trajectory T_i) of tool axis over multiple revolutions in an $x - y$ plane. In an ideal case, the tool axis will coincide with the z-axis which is represented by a point T_I. Next, the quasi-static fundamental motion (i.e., 1 UPR) is generated as a result of inaccurate tool-attachment and once-per-rev component of tool-geometric errors, which is represented by T_{QS}. This trajectory further extends to T_D to include the dynamic effects arising from the rotation of the spindle. These dynamic effects include rotating unbalance effects, response to frequency response functions of the spindle and once-per-rev component of structural vibrations.

The high-frequency components (i.e., n UPR, where $n \neq 1$) of radial throw contains the error motions of the spindle and the structural vibrations. The sources of spindle error motions are discussed here in brief. A spindle, in kinematic terms, is a device constrained in five degrees of freedom (3 translations and 2 rotational). Therefore, an *ideal* spindle only contains a single degree of freedom, i.e., pure rotation. However, to provide stiffness, it is over-constrained through line contacts provided by spindle bearings and housing, that results in small motions in each of the constrained degrees of freedom. These give rise to *spindle error motions*. These error motions can also be caused as a response to an external influence, such as thermal gradient, applied forces, external vibrations etc. As these quantities change when the spindle speed changes, therefore, spindle error motions are strongly dependent on spindle speed. They can be further classified into synchronous error and asynchronous error components [10]. The synchronous error component is obtained by taking a mean of the tool-tip trajectory over the number of revolutions (shown as T_{DS}). This synchronous error motion component can be subtracted from each revolution of the measured data to obtain the asynchronous error motion component (not-shown).

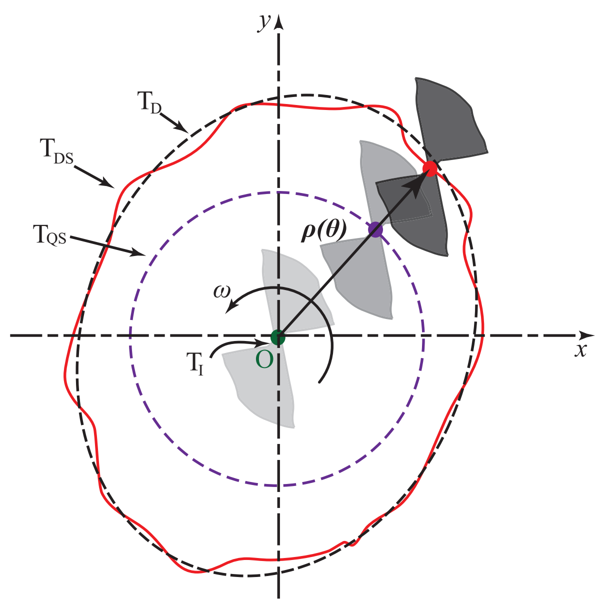

Figure 1.5: *Evolution of the trajectory of the radial throw.*

The radial throw measurements are typically conducted by using a precision test artifact rotated on the spindle. The motion of the tool-axis is then measured using a displacement measurement instrument. Since the instrument only captures the deviation in the radial direction, it is insensitive to the actual diameter of the part or test artifact. For this reason, the deviation directly reflect the motion of the tool-axis and/or the form error of the artifact, at the measurement plane. These motions may decomposed into various frequency components such as fundamental, synchronous and asynchronous. It is noted that the relative contribution of the various frequency components depend on the type of spindle, collet and tool combination.

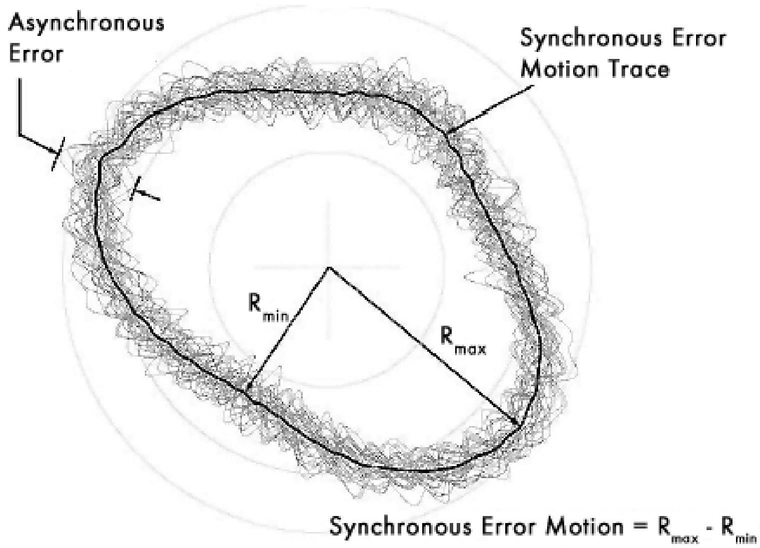

Figure 1.6: *Spindle error motions: synchronous and asycnhronous [15].*

There are a number of ways to quantify the fundamental component of radial throw. Lu *et. al.*[11] considered the elliptical trajectory as a sum of two vectors rotating in opposite directions at 1 UPR. Alternatively, the elliptical motion can be described by three distinct variables (major-axis, minor-axis, and ellipse orientation, i.e., orientation of the major-axis with respect to the x-axis). The quantification of synchronous and asynchronous error motions is standardized by [10]. The range of synchronous error motions is quantified by a *synchronous error motion value*, which is defined as the difference between the maximum and minimum synchronous error motions within a full revolution. This value is equivalent to calculation of the difference in radii between two concentric circles, centered at the least-squares circle center, that are just sufficient to contain the entire synchronous radial error motions (see Fig. 1.6). Similarly, the range of asynchronous error motions is quantified by a *asynchronous error motion value*, which is defined as "the maximum scaled width of the asynchronous error motion polar plot, measured along a radial line through the polar chart center." This method is susceptible to outliers in the measured data and can over-estimate the range. For this reason, as asynchronous error motions typically show a normal distribution, a $\pm 3\sigma$ band centered around zero provides a more robust estimate of the range of asynchronous error motions values.

1.3 Literature Review

1.3.1 Radial throw/run-out in micro-machining

This section reviews literature towards the identification of fundamental component of radial throw or the traditionally measured run-out. A number of approaches have been presented in the literature in the context of determining run-out when using micromachining spindles. Many researchers used static measurement methods (e.g., dial-gage and optical microscope based techniques) to measure run-out from the surface of the tool-shank (see Fig. 1.6(a)) or by observing the tool from the top, as the tool is rotated by hand [8, 16–19]. However, those methods failed to capture the speed-dependent behavior of radial throw, which was shown to have significant effect on radial throw magnitude [12].

A few studies attempted to address this issue by estimating dynamic run-out using indirect methods such as analysis of cutting forces [20, 21] or machining marks [22]. In case of estimation through observed machining forces, a mechanistic model is used with run-out as an unknown parameter. The run-out values that best fits the model is considered. For example, in Fig. 1.7(b) And in the case of estimating run-out from the machining marks (see Fig. 1.7(c)), the maximum diameter of the machined hole is considered as run-out. However, those indirect methods have yielded poor accuracy results, mainly due to the lack of effective approaches to measure output parameters (e.g., cutting forces) with sufficiently high accuracy and to isolate the run-out from other parameters (e.g., elastic deflections of the micro-tools and workpiece material variability) from the measurements of cutting forces and/or feed marks.

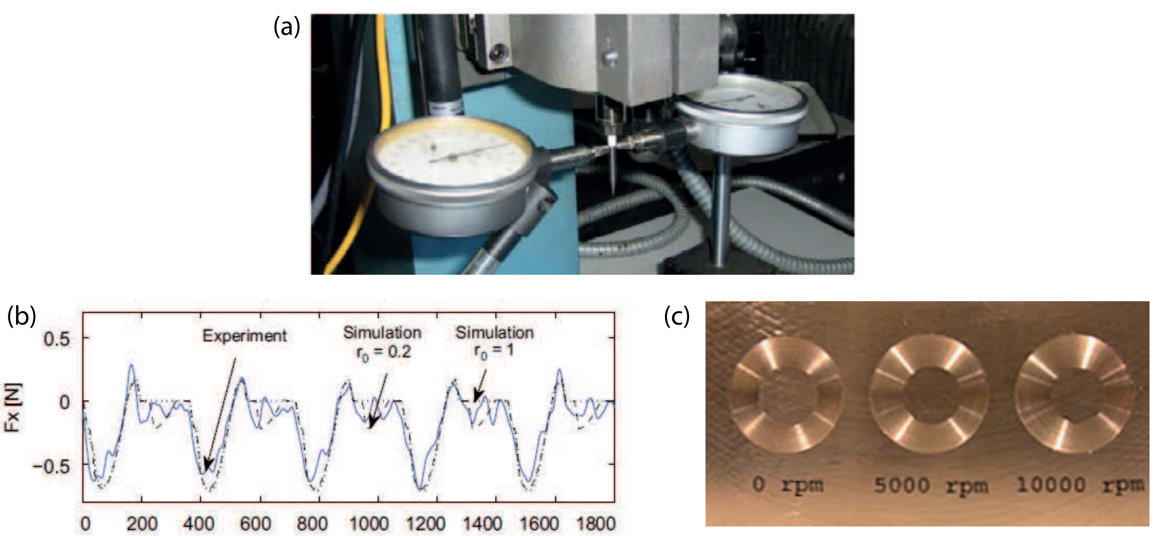

Figure 1.7: *Indirect methods to obtain run-out: (a) using dial gage [8], (b) estimating through machining forces [21], and (c) by observing machining marks [22].*

A few researchers have adapted high-accuracy measurement approaches to obtain and analyze the radial motions of rotating artifacts and/or micro-tools at varying spindle speeds. Liu *et. al.*[23] used a capacitive probe based method to measure run-out and the orientation of the maximum radial throw (which they referred to as the run-out) from a single point on the tool shank at varying spindle speeds. Similarly, Anandan *et. al.*[24] conducted radial measurements from a single point on the surface of a custom-made sphere-on-stem precision artifact using an LDV-based technique, and analyzed speed-dependent fundamental (one-per-rev) and spindle-error (synchronous and asynchronous) motions from those measurements. More recently, Lee *et. al.*[13] developed a optical system utilizing curved-edge diffraction to measure radial throw profile at a single location on the tool-shank at 3200 rpm spindle speed. Although those measurements captured the effect of spindle speed, since the tilts and cutting-edge orientations (with respect to the measured radial motions) were not obtained, they did not satisfy the requirements for accurate and comprehensive measurements of the radial throw.

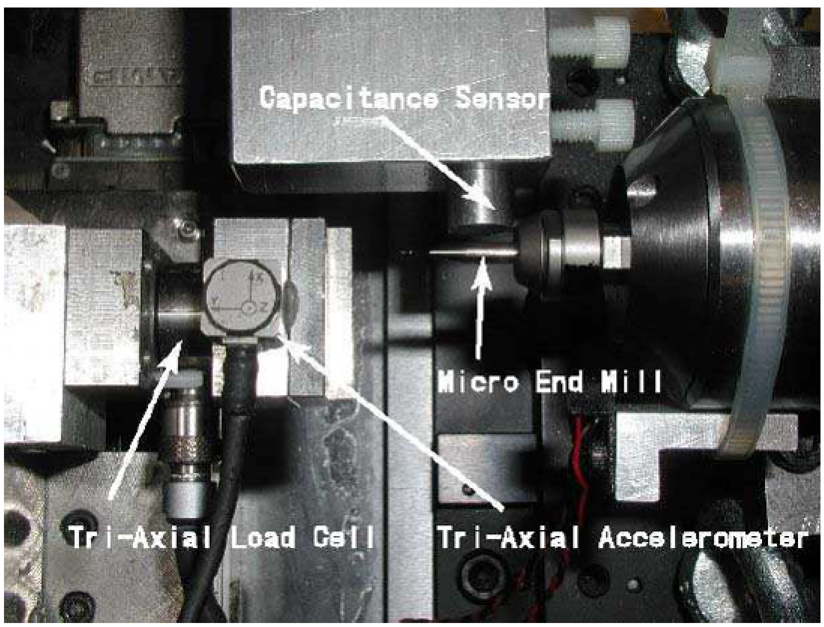

Figure 1.8: *Capacitive probe used by [23] for run-out measurement.*

Jun *et. al.*[25] performed single-axis measurements of run-out at multiple points on the surface of the micro-tool shank using a capacitance probe. From those measurements, they predicted the run-out and its orientation at the micro-tool tip to calculate the instantaneous chip loads toward investigating the dynamics of micromilling. They considered the contributions of the eccentricity and tilt in tool-attachment, and the additional eccentricity resulting from the tool-geometry errors. More recently, Anandan *et. al.*[26] used an LDV based technique and conducted measurements at two different axial planes on the surface of a cylindrical gage pin for obtaining the tilt information in addition to the radial motions. Although the aforementioned studies provided a foundation for measuring radial motions from micro-tool surfaces, a comprehensive, experimentally validated approach to determine the radial throw at each cutting point and the associated analysis to reveal the effects of spindle speed, dynamics, and statistical variation of radial-throw parameters has yet to be completed.

1.3.2 Spindle error motions in ultra-high-spindles

This section focuses on identification of high frequency (both synchronous and asynchronous) components of radial throw for miniature UHS spindles. Although this thesis focuses on the micro-scale spindles used for micro-machining applications, it is worth mentioning the Spindle Error Analyzer (SEA) − a commercial product to measure radial throw and its components in macro-scale spindles. This system uses multiple capacitive probes for displacement measurements on a macro-scale test artifact attached to the spindle. The system outputs both the synchronous and asynchronous motions as well as tilt error motions which can be used to determine resulting error motion at the tool tip. However, the capacitive sensors used in SEA cannot be used for accurate determination of radial throw in the case of miniature spindle systems. This is due to the non-linearity of the charge between a curved surface and a flat plate (sensing area) and a curved surface (measuring target area) and the effective sensing area being larger than the measuring target area [27, 28].

One of the important aspects in accurate determination of spindle error motion is the separation of artifact form errors. As mentioned earlier, the displacement measurement is insensitive to the diameter of the test artifact used for the measurement, but it is sensitive to the high frequency form errors of the test artifact. As depicted in Fig 1.9 [29], depending on the surface smoothness of the artifact, the artifact form errors can be comparable or an order of magnitude higher than the spindle error motions. Therefore, accurate measurement of spindle error motions necessities a procedure to separate the artifact form errors from the displacement measurements. In this regard, various techniques have been developed in literature for error separation, that can be classified into: (1) reversal techniques, (2) multi-probe techniques, and (3) multi-step techniques. A thorough description of these techniques is provided in [30].

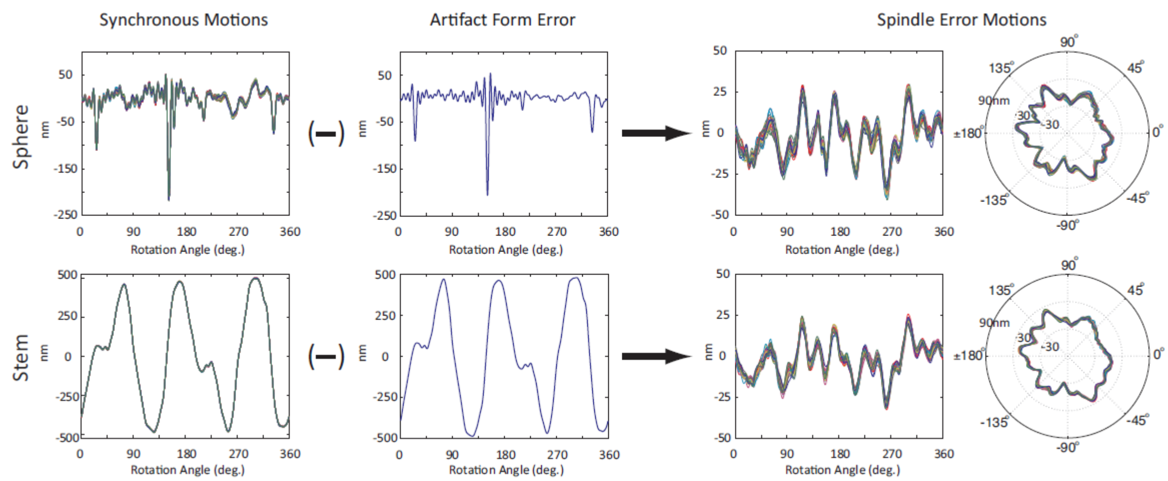

Figure 1.9: *A multi-step error separation method implemented by [29] where both sphere and stem portions are part of a custom made sphere-on-stem precision artifact.*

To solve the limitation of the capacitive-type displacement sensors, some optical measurement systems are discussed in literature to measure the spindle error motions in micro-scale spindles. Fujimaki *et. al.*[31] used an optical measurement method based on auto-collimation, which evaluates the radial error motion according to the movements of a laser beam reflected from a target sphere attached to the spindle end. Similarly, Murakami *et. al.*[32] developed an optical measurement system using a rod lens, a ball lens and photo-diodes for simultaneous measurement of five-degree-of-freedom error motions of an UHS spindle. However, both the techniques do not separate the form errors of the test artifact which significantly affects the measurement accuracy.

A few studies attempt to separate form errors of the test artifact towards accurate measurement of spindle error motions in UHS spindles. Castro [33] used a high-precision sphere as test artifact and developed a laser interferometery based measurement technique to measure the radial error motions of the spindle. The roundness of the sphere (12 mm diameter) was measured using a high accuracy roundness tester and the profile is input to the software for subtraction. More recently, Anandan *et. al.*[29] implemented a multi-orientation error separation technique to separate the artifact form error using laser Doppler vibrometers. The radial error motions were quantified at various spindle speeds. These studies are promising in obtaining the true spindle error motions of the UHS spindle after separating the form errors of the artifact. However, in both the studies, the error motions are measured under no load conditions. When an external load is applied, such as the forces experienced during micromachining processes, a change in the behavior of error motions could be observed [34]. Furthermore, the amount of changes in the error motions could be different at different rotational speeds [29]. Therefore, a complete understanding of spindle behavior demands the error motions to be measured and quantified under a range of loading conditions and at various rotational speeds.

Few studies in literature discusses the effect of loading on error motions of a macro-scale spindle. Sharma and Patterson [35] loaded upper and lower bearings of a macro-scale spindle by applying static load in axial direction and studied axial and radial spindle error motions. The axial error motions remain unchanged on application of external loads up to 140lbs. Similar behavior was obtained for asynchronous radial error motions except for measurement at 1000 rpm where appreciable increase was noticed on loading. ASME B89.3.4M [36] prescribes the use of master axis method to load spindle for dynamic compliance measurements. In [34], master axis was used to characterize radial spindle error motions of a macro-scale spindle under load. In this work, a master axis was attached to the rotor of the spindle under test via a rigid connection. Static load was applied to the stator of the master axis, kept stationary, to load the spindle in radial direction. The characteristics of synchronous error motions were found to vary with load as well as with spindle speed. However, in case of UHS spindles, the use of master axis is not suitable as the radial stiffness of these spindles are very low and in many cases, ambiguous. Even a slight misalignment with the master axis would cause permanent damage to the spindle bearings. Hence, a non-contact loading approach is required.

In conclusion, there are many different approaches discussed for the measurement of error motions of in UHS spindles. Yet, none of the studies focused on spindle error motions under the application of external forces. Further, there is a lack of well characterized loading devices to apply non-contact loading to the generally fragile UHS spindles. Therefore, it is important to develop non-contact static loading approaches to study the effect of external loading on the the spindle error motions, and on the changes in the radial throw of tool axis.

1.3.3 Geometric errors in micro-tools

The last component in completely understanding the motion at the tool-tip is the tool-geometric errors. Due to the complex nature of a micro-tool profile, there could be a large number of features to assess. However, the features affecting the radial throw at the cutting edges include: (1) the non-straight tool-axis, (2) the imprecise tool diameter, and (3) the inaccuracy in the location of the cutting edges. Therefore, the methods discussed here are limited to the determination of the selected features.

To estimate the contribution of tool-geometric errors, both online and offline methods are prevalent. An online measurement include measurement of *effective tool diameter* at the tip of the tool. The effective tool diameter consists of both the radial throw of the tool axis and the tool-geometric errors. On the other hand, in an offline measurement approach, the tool is measured outside of the machine tool spindle to measure/estimate individual geometric errors and are later combined with the radial throw to obtain the dynamic tool-tip trajectory.

There are various approaches available in the literature for an online measurement of effective tool diameter. Some commercial products such as tool-setters (e.g., Marposs) and vision systems (e.g., Dyna Vision) are being used to measure effective diameter of the tool when it is installed on the spindle. However, the usage of these commercial products are limited to low spindle speeds. Inoue *et. al.*[37] proposed an optical method to measure the tool diameter using laser diffraction. The results were promising when measured during hand rotation but not at spindle rotation speeds. This could be due to low camera frame rate which is unable to cope up with the high spindle speeds.

For offline measurement, currently, the scanning electron microscopy (or SEM), appears to be the most common tool of investigation used in assessment of tools [38]. With suitable post processing, it can provide both the tool-diameter and the inaccuracy in the location of the cutting edges at the tool-tip. Other approaches include some form of optical microscopy at high magnifications, followed by post processing. The measurement of non-straightness of the tool is relatively challenging due to complex 3D profile of the tool and micron scale tool diameter.

Marsh *et. al.*[39] characterized cylindrical micro-tools with 50 μm diameter and 1.5 mm in length using scanning white light interferometery. In this work, they analyzed the surface of the cylinder along its axis for inaccuracies in surface profile. Standard height and shape parameters were computed from the roughness, waviness and form profiles. Because of the lack of rotation arrangement, full 3D profile of the cylindrical tip could not be measured. Later Marsh *et. al.*[40, 41] developed a precision instrument based on scanning probe microscopy for measurement of roundness profiles of micro shafts. However, this procedure measures one cross-section at a time which could be time consuming to measure the length of the shank portion, and is only limited to axially-symmetric micro-components.

More recently, the focus variation based optical microscopy [42], in conjunction with a motorized rotation stage, is able to capture the tool profiles in 3D. It does so by measuring multiple arcs of the tool along its length, one at a time, and then stitches the data together with the help of software capabilities. Such a measurement of a drilling tool is presented in Fig. 1.10. The standard deviation of in the measurement of major radius of the drill was in the nanometer range. Thus, focus variation based microscopy is seen as a strong contender to quantify non-straight tool axis.

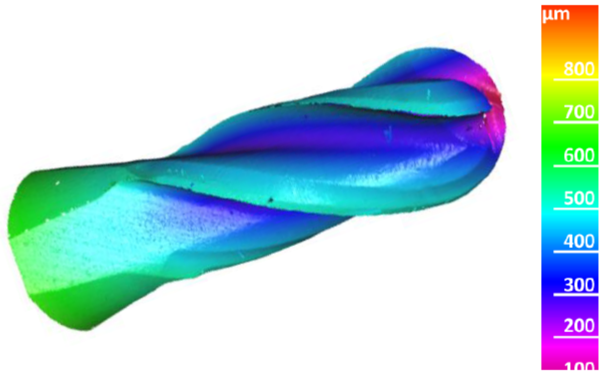

Figure 1.10: *3D dataset of a micro milling cutter [42].*

From the presented literature, the common metrology equipment are only suitable for 2D measurements and/or limited 3D profile measurement. The focus variation microscopy shows promise in capturing the 3D profile of a micro-tool and therefore, more research is needed to assess the technology and to develop appropriate measurement and post-processing techniques to extract the geometric errors in the tool-axis and its contribution to the radial throw.

1.4 Research Objectives

To date, the dynamic tool tip trajectory when using UHS spindles has not been studied comprehensively. Prior research mainly focused on measurement of single-axis tool run-out, which cannot be used to obtain instantaneous trajectory of the cutting edges of the tool. Towards gaining a better understand and characterize the dynamic motions of the tool tip (dynamic tool-tip trajectory) when using UHS spindles, the specific objectives of this doctoral research are:

1. **Measurement and analysis of radial throw when using UHS spindles**: An approach to determine the trajectory of the cutting edges of a micro-tool in the presence of radial throw is presented. The approach involves (1) a mathematical framework to determine the trajectory of the cutting edges from measurements of the radial throw at two locations on the tool shank (see Chapter 3), and (2) an experimental method, based on non-contact displacement measurements, for simultaneous radial throw measurements on the tool shank at two mutually-perpendicular radial directions (see Chapter 4). The dynamic response of the spindle at different spindle speeds and its relation to the trajectory (form, magnitude, and orientation) of the radial throw are investigated. A statistical analysis of radial throw param-

eters for repeated attachment-detachment of a micro-tool on an UHS spindle is performed. Subsequently, a study is conducted to determine the main contributors of the radial throw orientation within the tool-collet-spindle assembly. The results are presented in Chapter 4.

2. **Effect of static loading on the radial throw when using UHS spindles**: As the rotational motion (errors) of the spindle is expected to change when external loads (i.e., micormachining forces) are applied, an experimental method is devised to measure the spindle-error motions when the spindle is under axial and radial loading. In this regard, a non-contact force application setup is constructed using permanent magnets. For different loads, the resulting changes in the radial throw components—fundamental (one-per-rev), synchronous and asynchronous—are analyzed. The results from this study are presented in Chapter 5.

3. **Assessment of geometric errors in microtools**: The geometric errors of the microtools, specially the non-straight tool axis, the variations on the tool diameter, and the inaccuracy in the location of the cutting edges, directly affect the radial throw at (and the trajectory of) the cutting edges. Accordingly, a measurement approach to to quantify the geometric errors of microtools is developed. Subsequently, the mathematical framework presented in Chapter 3 is also extended to integrate tool-geometric errors towards a precise determination of the radial throw at the cutting edges of the tool. The results from this study are presented in Chapter 6.

4. **Effect of radial throw on the quality parameters of the micromachined part**: This study integrates the obtained knowledge (and results) from all the error sources and systematically studies their effects on dimensional and surface quality parameters of the micromachined features through numerical simulations. A 3D tool model (with geometric errors) is created in MATLAB where the radial throw is calculated and added at each axial location to accurately represent the trajectory of the cutting edges. The results from this study are presented in Chapter 7.

1.5 Research Contributions

The specific contributions of this thesis research include [43–48]:

1. A mathematical formulation to capture the radial throw at the tool-tip.

2. Development and validation of a laser Doppler vibrometer (LDV)-based methodology to measure speed-dependent radial throw (magnitude and orientation) at the tool-tip. Obtaining

accurate measurements required design and installation of a epoxy-granite metrology frame for low uncertainty measurements.

3. A simplified model to predict the speed-dependence of radial throw of the tool-axis based on dynamic response of the UHS spindle.

4. Design and development of a novel magnet based loading setup to apply axial and radial loading to the UHS spindles. This required implementation of a multi-probe error-separation technique to remove the artifact form error and obtain the true spindle error motions.

5. A microscopy-based technique to measure the geometric errors (axis offset between the shank and the tip portion) of the micro-endmills.

6. A MATLAB based 3D tool simulation to study the effect of radial throw on surface location error (SLE), peripheral surface roughness and uncut chip thickness.

CHAPTER 2

Design of a Metrology Frame for Low Uncertainty Measurements

2.1 Introduction

This task focuses on enhancing the accuracy and repeatability of LDV-based measurements by reducing the effect of noise and vibrations originating from rotating spindle and surrounding environment. Earlier, a measurement frame constructed from extruded aluminum (80-20 Inc.) pieces was used on which the LDVs were mounted to characterize UHS micromachining spindles. The vibration damping characteristics of aluminum frame is a concern when taking precise measurements. Therefore, a material with better vibration damping than aluminum is considered, upon recommendation by Dr. Gregory Vogl (NIST).

2.2 Material - Epoxy Granite

Polymer granite has excellent vibration damping characteristics compared to aluminum and other structural materials such as cast iron and natural granite. It can be casted into any shape and the cast can also be integrated with threaded inserts which provides a means to attach fixtures/instruments to the frame. A comparison of key mechanical properties for both aluminum alloy (6105-T5) and epoxy granite (also known as Castinite [49]) is presented in Table 2.1.

Table 2.1: Comparison of material properties between Al 6105-T5 and epoxy granite.

Property	Al 6105-T5	Epoxy Granite
Density (kg/m^3)	2700	2300
Modulus of Elasticity (GPa)	69	31
Poisson's ratio	0.33	0.25
Damping ratio [50]	∼0.0004	∼0.05

2.3 Frame Design and Analysis

The functional requirements for the metrology frame can be listed as:

1. Isolate the natural frequencies from the operating range of the spindle, between 800 — 3000 Hz.
2. Drive down the first ten natural frequencies of the frame below the lower bound (i.e., <800 Hz).
3. Modular design to mount various instruments.
4. The frame can be used as a machine tool frame at the end-of-life (i.e., completion of measurements).

To achieve this, a number of different frame designs (see Fig. 2.1) were conceptualized and subsequently analyzed in ANSYS. For each design, harmonic analysis was conducted to compare the frequency response functions (FRFs). The frame is divided into 10-node tetrahedral elements and is harmonically excited from the base between 1 — 3000 Hz (corresponding to speeds from 0 — 180,000 rpm). The response was measured at two different locations, points A and B, corresponding to the LDV mounting positions (see Fig. 2.2). For each design, FRFs were generated for points A and B from the simulation data. The design with the minimum number of peaks falling between the spindle operating frequencies, i.e., 833 — 3000 Hz (which corresponds to 50,000 — 180,000 rpm) is selected. After the selection of design, an design of experiments (DOE) study was conducted by varying the major dimensions of the frame in order to minimize the amplitude of the peaks in FRFs.

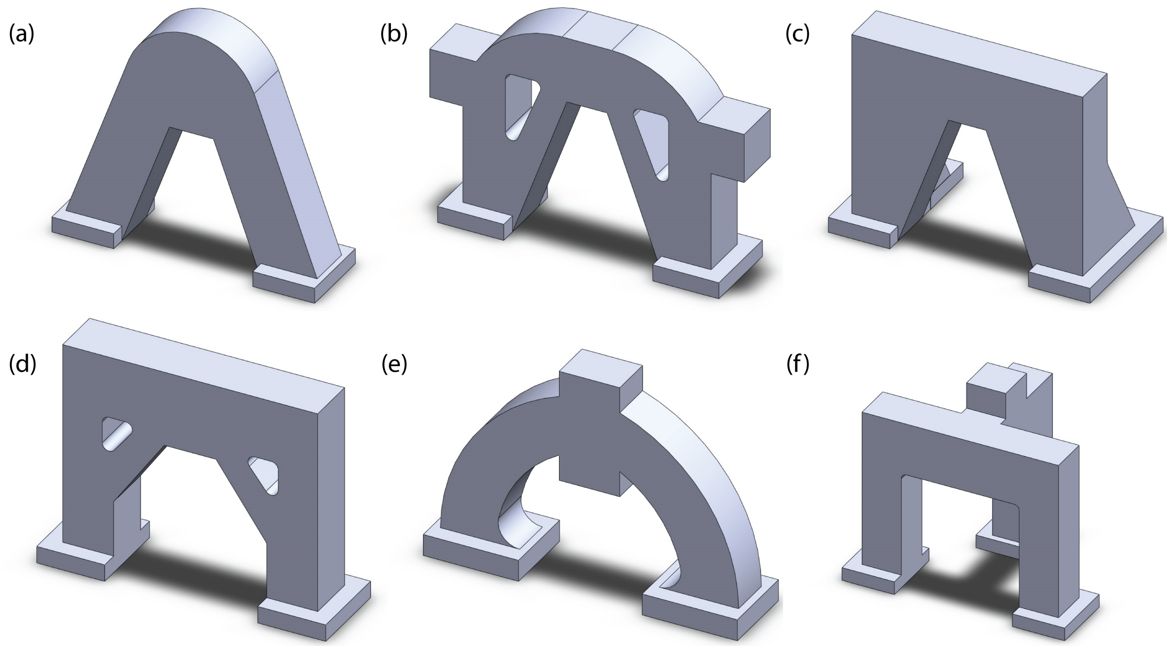

Figure 2.1: *Various frame designs considered for the analysis.*

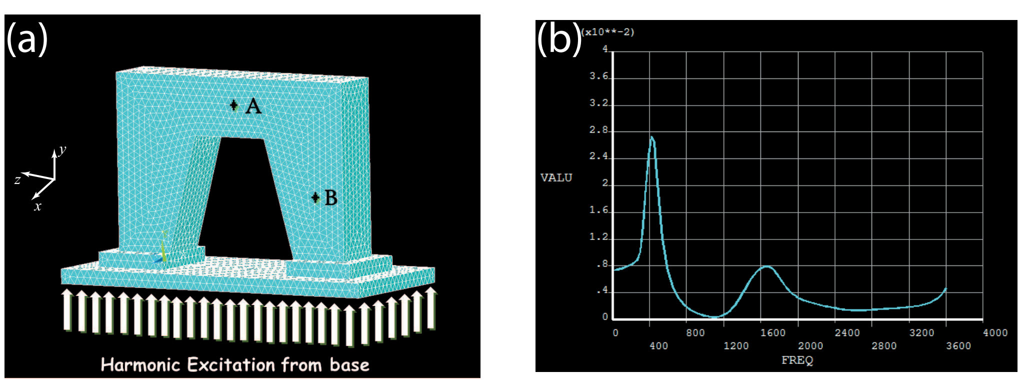

Figure 2.2: *Harmonic analysis of the frame (a) setup in ANSYS APDL, and (b) frequency response function (FRF) at Point A along z-direction.*

2.4 Manufacturing and Testing

After selecting the design and finalizing the frame dimensions, detailed drawings were created with appropriate location and orientation tolerances (see Fig. 2.3(a)). The metrology frame was manufactured by Precision Polymer Casting, LLC and was installed on the vibration isolation table replacing the existing aluminum frame. After installation, an experimental modal analysis was conducted to find out natural frequencies of the frame. A modally tuned impact hammer (PCB 086B03) was used to excite the structure and the response was measured with the help of a single-axis accelerometer (PCB U352C66) placed close to the impact location. Three separate measurements were taken from different locations corresponding to three mutually orthogonal directions (x, y and z), as shown by the yellow dots on the frame in Fig. 2.3(b). An acceleration-to-force FRF were obtained in each of the measurement direction and they were combined to get a resultant FRF as shown in Fig. 2.4. From the FRFs, three distinct regions (I, II and III) were identified which can lead to increased vibration amplitudes in the frame during measurements. Thus, during experiments, we will be aware of these ranges which could increase the measurement uncertainty.

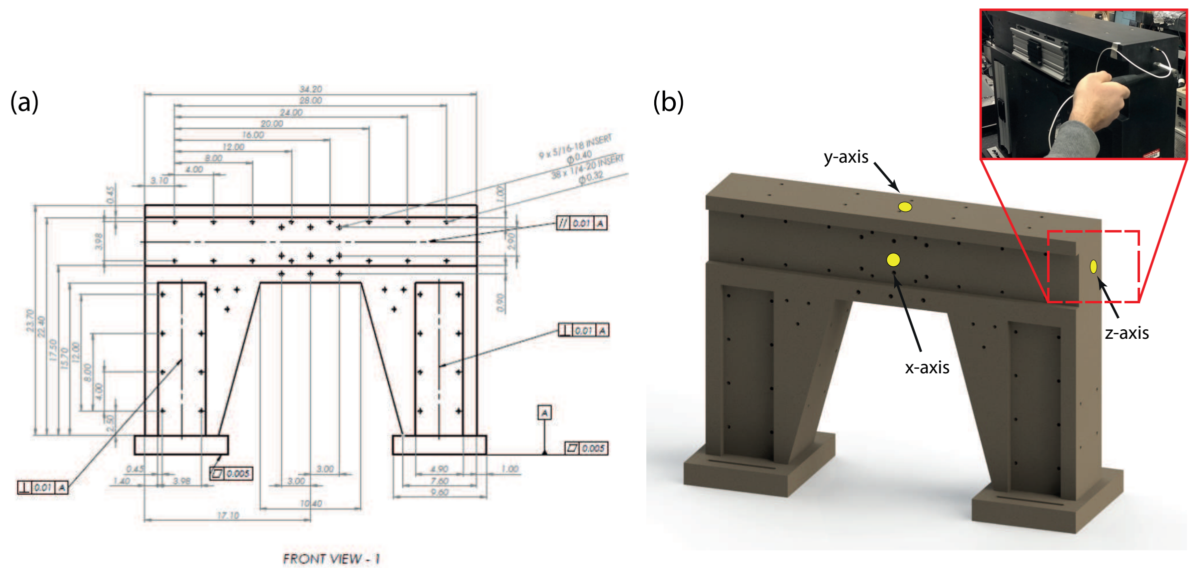

Figure 2.3: *(a) One of the drawings for the frame indicating dimensions and tolerances, and (b) modal testing after installation.*

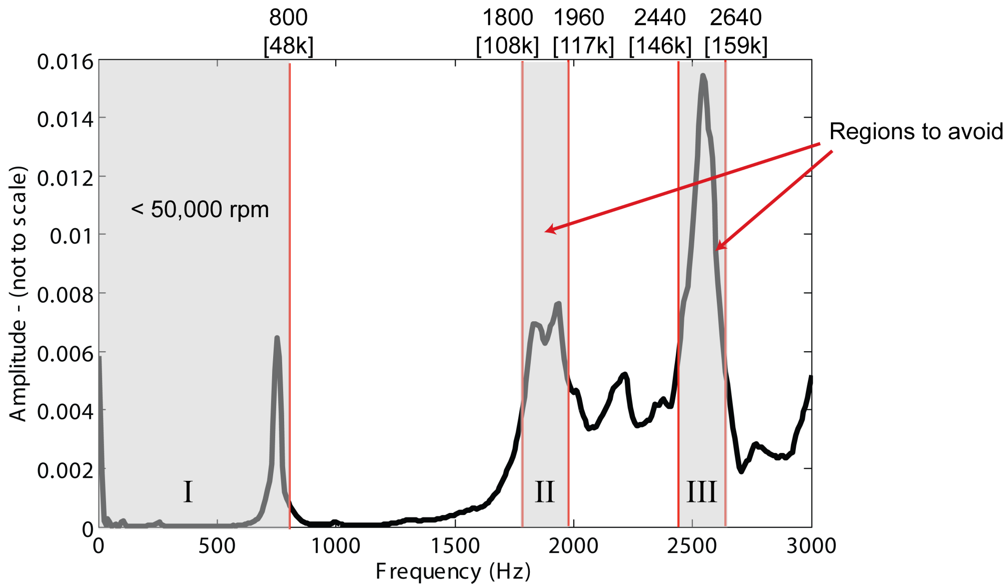

Figure 2.4: *Resuls from the modal testing of the frame.*

2.5 Summary

1. A new spindle-metrology frame (and the associated auxiliary components) was designed to reduce the noise and vibrations and their influence on the measurements, thereby, reducing the uncertainties of the LDV-based measurement technique. All testbed components were fabricated from cast epoxy-granite, which possesses superior vibration damping properties with respect to commonly used structural materials.

2. An experimental modal analysis was conducted to determine the natural frequencies of the structure. Based on the results, two ranges of frequencies within the frequency ranges of interest were recommended to be avoided since those ranges could cause larger uncertainty in measurements. Although the machining process may generate excitation beyond 3000 Hz (higher harmonics), due to the large mass of the frame, it will be increasingly difficult to excite it at higher frequencies.

CHAPTER 3

Mathematical Framework to Determine Radial Throw

In this chapter, we present a general mathematical framework to calculate the trajectory of the cutting edges of a microtool in the presence of radial throw. The framework uses a vectorial approach that relates the radial throw measured at two distinct axial location of the tool-shank to the radial throw at the tool-tip. Subsequently, the radial throw at the tool-tip is translated to the cutting edges through an orientation angle.

3.1 Mathematical Description of Radial Throw

Figure 3.1 illustrates the end of a cutting tool rotated on a spindle. The tool rotates about an axis z, which is referred to as the rotational axis or the axis average line. Two mutually-orthogonal axes, x and y, defined perpendicular to the z axis constitute the plane illustrated in Fig. 3.1. As will be described in the next section, x and y axes are our measurement axes. The radial throw of the (tool) axis is defined by the vector $\boldsymbol{\rho}(z,\theta)$, where θ is the angle of rotation of the tool (referenced at the "first" bottom cutting edge or C_1) measured from the x axis and z is the axial location of the z plane measured from the spindle nose. Subsequently, the trajectory of the m^{th} flute $\boldsymbol{p_m}$, on the z plane can be written as,

$$\boldsymbol{p_m}(z,\theta) = \big(\rho_x(z,\theta) + r\cos(\theta + 2\pi(m-1)/n)\big)\boldsymbol{i} + \big(\rho_y(z,\theta) + r\sin(\theta + 2\pi(m-1)/n)\big)\boldsymbol{j}, \quad (3.1)$$

where $\boldsymbol{i}$ and $\boldsymbol{j}$ are the unit vectors along the x and y directions, respectively. Variables ρ_x and ρ_y are the x and y components of $\boldsymbol{\rho}$, r is the radius of the cutting tool and n is the number of cutting flutes. The radial throw of each cutting point can be obtained by subtracting the actual trajectory $\boldsymbol{p_m}$ with the ideal one (i.e., circular trajectory with diameter equal to the twice the tool-radius). At any rotation angle θ, the orientation of radial throw is denoted by $\eta_z = \eta_z(\theta)$ and is defined as the counterclockwise angle from the reference cutting edge towards the radial throw vector at a given axial location z. As described in the following section in this work, θ is determined from separate angular measurements of the tool cutting edge with respect to a reference mark on the tool shank.

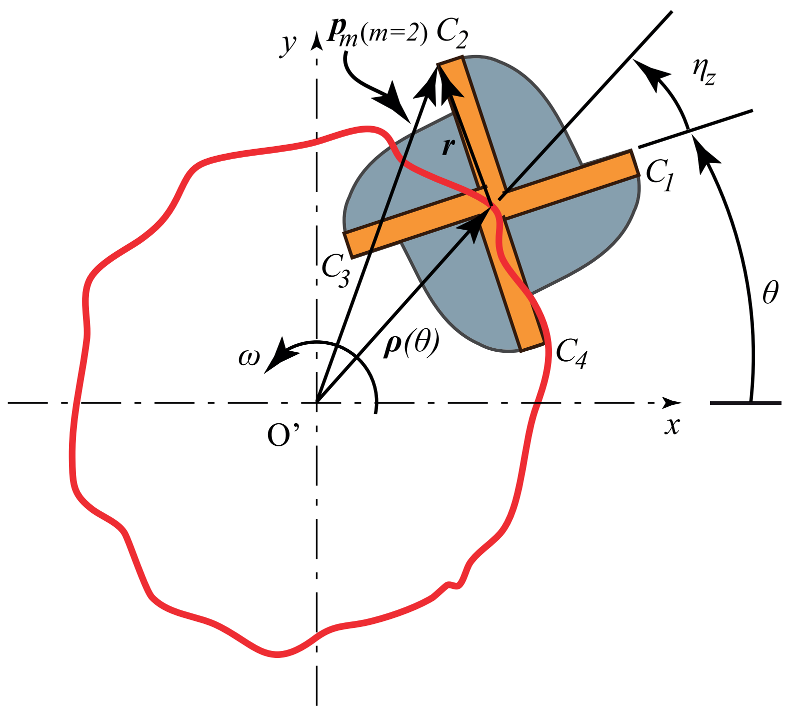

Figure 3.1: *Description of radial throw, $\boldsymbol{\rho}(\theta)$. The magnitude of radial throw is significantly exaggerated in this figure to help the visualization. C_m indicates the m^{th} cutting edge.*

Figure 3.2(a) describes the tool axis and its relation to the rotational axis z. The tool axis, which is assumed to be straight, is defined with a vector $\boldsymbol{q}$, which extends out of the spindle nose (from point A). The eccentricity vector, $\boldsymbol{e}$, is the radial throw of the (tool) axis at the $z = 0$ plane (see Fig. 3.2(b)). The angle η_z, which is the orientation of $\boldsymbol{\rho}(z, \theta)$ with the reference cutting edge, changes with axial location z and rotation angle θ due to tilt and change in the magnitude of radial throw, respectively. In general, the effect of tilt at any axial location z can be represented by a projection vector (or tilt vector) $\boldsymbol{EB}$ (as shown in Fig. 3.2(c) where points A and E are coincident), obtained by projecting $\boldsymbol{q}$ on the xy plane, and it is oriented at a counterclockwise angle δ to the eccentricity vector $\boldsymbol{O_z E}$ (also coincident with $\boldsymbol{OA}$).

Determination of the trajectory $\boldsymbol{p_m}$ at each cutting point entails calculation of each of the

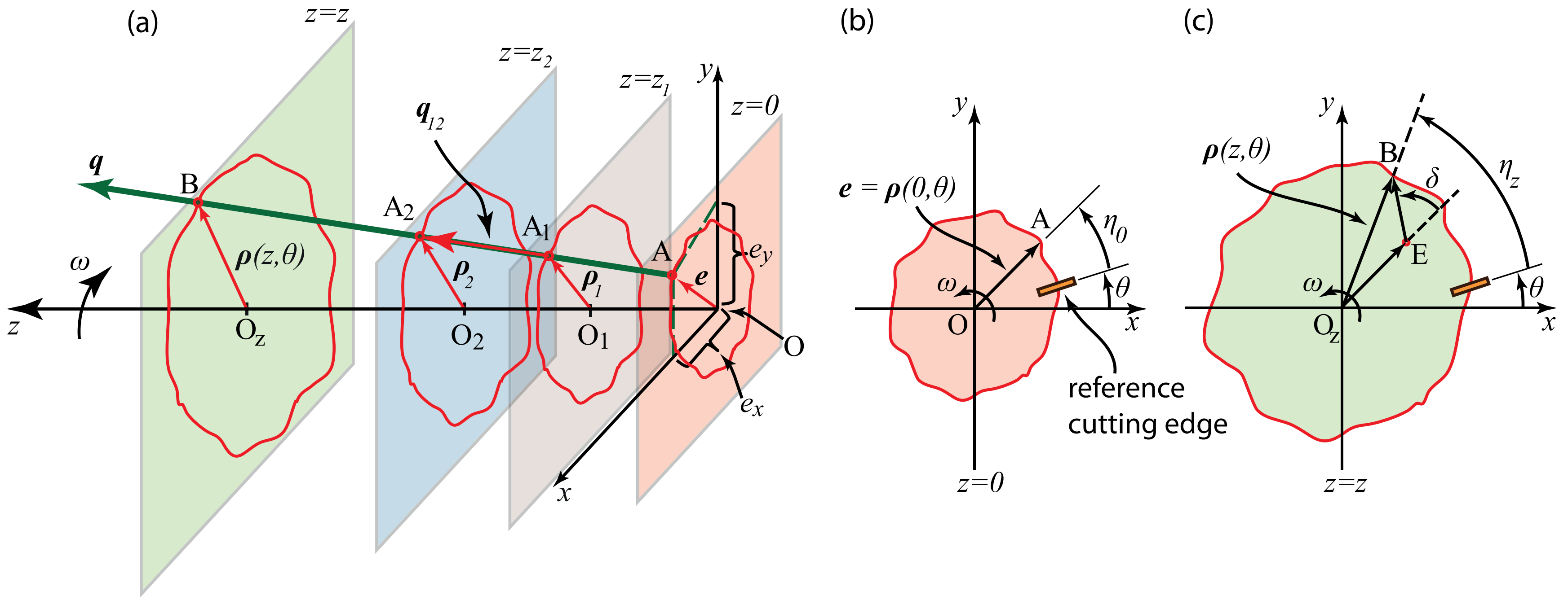

Figure 3.2: *(a) Radial throw and its relation to the rotational axis, (b)-(c) parameters of radial throw for two x-y planes located at z=0 and z=z, respectively.*

parameters in Eq. (3.1) from the measurements performed at two axial positions (z_1 and z_2) of the tool shank along the x and y directions. Those measurements provide x and y components of $\boldsymbol{\rho}$ at the two axial locations, i.e.,

$$\boldsymbol{\rho}_1 = \boldsymbol{\rho}(z_1, \theta) = \rho_{1x}\boldsymbol{i} + \rho_{1y}\boldsymbol{j}, \quad \text{and} \quad \boldsymbol{\rho}_2 = \boldsymbol{\rho}(z_2, \theta) = \rho_{2x}\boldsymbol{i} + \rho_{2y}\boldsymbol{j}. \tag{3.2}$$

In general, any component of $\boldsymbol{\rho}$ at any z location (e.g., ρ_{1x}) could contain many frequency components, each could be represented by a sine with a magnitude (e.g., σ_{1x_k}) and a phase (e.g., ϕ_{1x_k}), where k is a multiple of the rotational frequency. From Fig. 3.2(a) (see inset for clarity), a vectorial equation

$$\boldsymbol{\rho}_1 + \boldsymbol{q}_{12} = (z_2 - z_1)\boldsymbol{k} + \boldsymbol{\rho}_2 \tag{3.3}$$

can be written, where $\boldsymbol{q}_{12} = \boldsymbol{q}_{12}(\theta)$ indicates the vector along the tool axis, spanning from the z_1 plane to the z_2 plane and $\boldsymbol{k}$ is the unit vector along the z direction. Since $\boldsymbol{\rho_1}$, $\boldsymbol{\rho_2}$ and $(z_2 - z_1)$ are known, using Eq. (3.3), the unit vector $\boldsymbol{e_q} = \boldsymbol{e_q}(\theta)$ along the tool axis (i.e., along $\boldsymbol{q}$) can be calculated from

$$\boldsymbol{e_q} = \frac{\boldsymbol{q}_{12}}{|\boldsymbol{q}_{12}|} = \frac{\boldsymbol{\rho}_2 - \boldsymbol{\rho}_1 + (z_2 - z_1)\boldsymbol{k}}{|\boldsymbol{\rho}_2 - \boldsymbol{\rho}_1 + (z_2 - z_1)\boldsymbol{k}|}. \tag{3.4}$$

Furthermore, the tilt angle (not shown), which is the acute angle between the rotational axis z and the tool axis, can be determined from

$$\zeta(\theta) = \cos^{-1}\left(\boldsymbol{e_q} \cdot \boldsymbol{k}\right), \tag{3.5}$$

where "$\cdot$" indicates the inner product operation.

At this point, finding the eccentricity vector $\boldsymbol{e}$ from the measurements will simplify the determination of the radial throw at any cutting point along the flutes. To determine the eccentricity vector from the measurements, we again consider Fig. 3.2(a) and write the vectorial equation

$$\boldsymbol{e} + \boldsymbol{q}_{01} = z_1\boldsymbol{k} + \boldsymbol{\rho}_1, \quad \text{yielding} \quad \boldsymbol{e} = z_1\boldsymbol{k} + \boldsymbol{\rho}_1 - \boldsymbol{q}_{01} \tag{3.6}$$

Here, $\boldsymbol{q}_{01}$ is the vector along the tool axis spanning from the spindle nose ($z = 0$ plane) to the z_1 plane and can be calculated as

$$\boldsymbol{q}_{01} = \frac{z_1}{\cos\left(\zeta(\theta)\right)}\boldsymbol{e_q} \tag{3.7}$$

The radial throw of the axis at any axial location z satisfy the vectorial equation (refer to Fig. 3.2(a))

$$\boldsymbol{\rho}(z, \theta) + z\boldsymbol{k} = \boldsymbol{q}_{0z} + \boldsymbol{e} \tag{3.8}$$

where $\boldsymbol{q_{0z}} = \big(z/\cos\zeta(\theta)\big)\boldsymbol{e_q}$. Thus, $\boldsymbol{\rho}(z,\theta)$ can now be written as

$$\boldsymbol{\rho}(z,\theta) = \frac{z}{\cos\zeta(\theta)}\boldsymbol{e_q} + \boldsymbol{e} - z\boldsymbol{k}. \tag{3.9}$$

Therefore, trajectory of a cutting point can now be determined by finding $\rho_x(z,\theta) = \boldsymbol{\rho}(z,\theta)\cdot\boldsymbol{i}$ and $\rho_y(z,\theta) = \boldsymbol{\rho}(z,\theta)\cdot\boldsymbol{j}$ from Eq. (3.9) and substituting them into Eq. (3.1). The orientation of $\boldsymbol{\rho}(z,\theta)$ can now be given as

$$\eta_z = \cos^{-1}\left(\frac{\boldsymbol{\rho}(z,\theta)}{\big|\boldsymbol{\rho}(z,\theta)\big|}\cdot\boldsymbol{i}\right) - \theta. \tag{3.10}$$

CHAPTER 4

Measurement and Analysis of Radial Throw of the Tool-axis

In this chapter, we present a detailed measurement approach for accurate determination of the trajectory of the cutting points of micro-scale cutting tools while rotating at ultra-high-speeds. The approach involves a non-contact LDV based displacement measurement method to obtain radial throw characteristics at two locations on the tool shank along two mutually-perpendicular radial directions (to obtain parameters of Eq. 3.2). Afterwards, the equations presented in the Section 3 can be used to obtain radial throw at the tool tip. The measurement approach is validated through custom-devised experiments (i.e., by comparing the predicted and independently measured radial throw when rotating a micro-tool blank on a hybrid ceramic ball bearing miniature spindle at varying rotational speeds). Subsequently, the validated approach is used to measure the speed-dependent radial throw when rotating a commercially-available micro-scale cutting tool on the same spindle.

4.1 Introduction

In this chapter, we focus on the fundamental component of radial throw. The major contributors of radial throw in micromachining arises from the mechanical interfaces involving spindle-collet-tool and the dynamic behavior of the spindle structure [12, 24, 51]. These contributions are reflected as motions at the fundamental rotational frequency. The spindle error motions and the effect of tool-geometric errors will be discussed in later chapters. As such, this chapter presents an approach that allows incorporation of all the contributors of radial throw (i.e., fundamental component, spindle error motions, and tool-geometric errors), and focuses on accurate determination of its major component i.e., radial throw at the fundamental rotational frequency.

The factors affecting the magnitude and orientation of radial throw such as tool-attachment and inaccuracies in the tool-collet-spindle interface are studied. Subsequently, a study is conducted to analyze the contribution of spindle-dynamics on radial throw. As such, the presented comprehensive approach can be used for accurate determination of the spindle-speed dependent radial throw of tool-axis and its contribution towards the trajectory of cutting points for a micro-tool rotated on an UHS spindle.

4.2 Experimental Methods

4.2.1 Experimental setup

The experimental setup used in this work is shown in Fig. 4.1. The radial motions are measured using two laser Doppler vibrometers (LDVs) with fiber-optic laser heads. Each fiber-optic carrier terminates at an objective that allows focusing the laser on the target. Each objective is attached to a 6-axis precision mount (Thorlabs, K6X) with high-resolution rotational and translational motions, facilitating precise adjustments of the laser position and orientation. The kinematic mounts are attached on a single-axis linear stage (Newport 423, angular deviation < 200 μrad) to enable translating the lasers axially to selected positions along the rotational axis (the *axis average line*). The two lasers are arranged in a mutually-perpendicular orientation within a plane (i.e., *the plane of measurement*, which is perpendicular to the axis average line) by following the procedure described in [52]. The x and y measurement axes are set by the orientations of the two lasers. The vertical (y) laser is attached to a custom-made polymer granite arch (see Sec. 2), which is specially designed to provide a high level of damping and minimal vibrations. The horizontal (x) laser is attached to a polymer granite block. The spindle is housed in a cast iron holder, which is bolted onto another polymer granite block. Each of the polymer granite components are then fixed to an optical table (Newport RS 4000 with tuned damping). A tube microscope (1,667X magnification; 180 x 135 mm field of view) with a charge-coupled device (CCD, Sentech-07H6491) camera is also placed on the optical table to assist in axial placement of the tools while clamping them on the spindle.

The LDV systems (Polytec OFV-552 with fiber-optic sensor head) are used with a displacement decoder (DD-500 analog displacement decoder), providing a frequency bandwidth of 350 kHz and a resolution of few picometers [53]. For accurate LDV measurements, the lasers are required to be perpendicular to and focused on the measurement surface. The procedure in [52] was used to

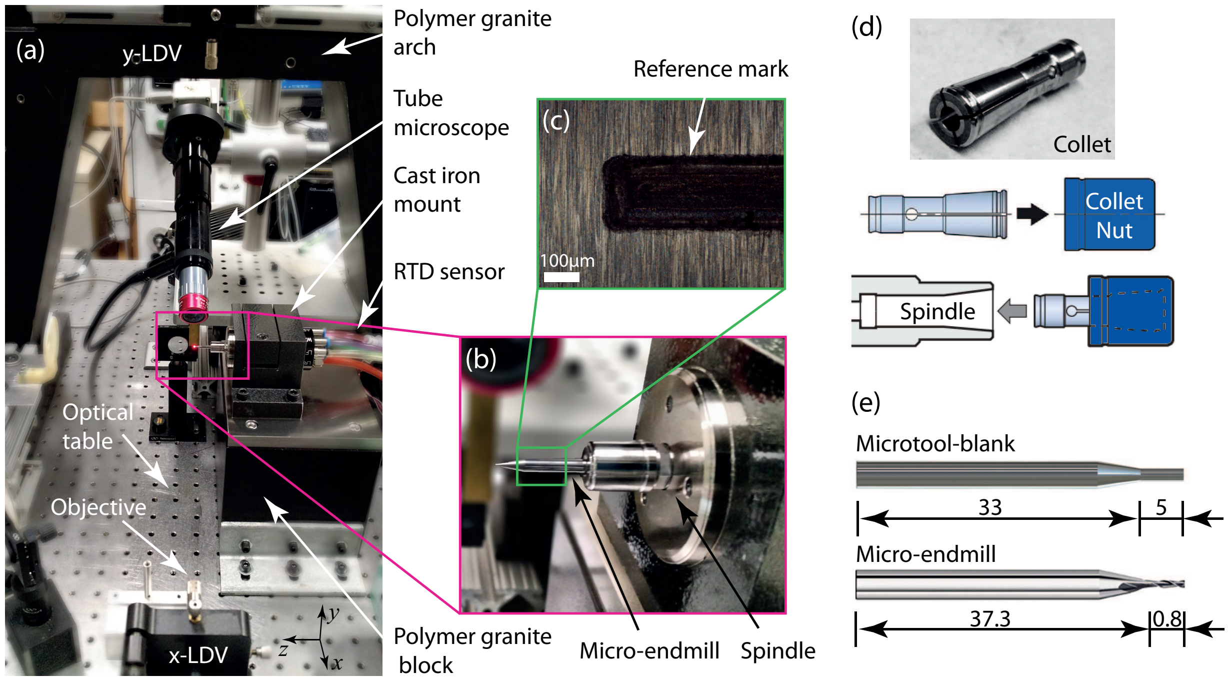

Figure 4.1: *(a) The experimental setup used for the measurement of radial throw, (b) a micro-endmill is attached to the spindle, (c) reference mark on the tool, (d) a four-jaw collet and clamping of collet using a collet nut, and (e) microtool-blank and micro-endmill used in this work. (dimensions not to scale)*

align and focus the lasers on the measurement surfaces by adjusting the 6-axis mounts and the objectives, respectively. For this purpose, the strength of the reflecting laser light was monitored using a voltage indicator provided by the LDV system.

Although the approach presented in this work is applicable to any microtool-collet-spindle assembly with an ultra-high-speed spindle, the experiments presented in this study were performed on an electrically driven, hybrid ceramic ball bearing miniature spindle (IBAG HT 45S140) with a maximum rotational speed of 140 krpm. The axial and radial static stiffness values at the spindle nose are specified by the manufacturer as 21 N/μm and 24 N/μm, respectively [7]. The spindle is water cooled to maintain the internal temperature at 27°$\pm$ 2°C through an external chiller unit. The spindle works with a MEGA4S collet system for clamping the tools (see Fig. 4.1(d)). The collet features a four-jaw design, and a collet nut is used to attach microtools onto the spindle. A collet wrench is used to tighten the collet nut to the recommended torque of 10 Nm.

For the radial throw measurements presented in this work, a commercial micro-endmill (254 μm diameter tool with a 3.175 mm shank diameter) and a custom-fabricated microtool blank (1.5 mm diameter at tip with a 3.175 mm shank diameter) were used (see Fig. 4.1(e)). For each of the two samples, the form errors were estimated to be below $\pm$500 nm from radial throw measurements at multiple locations at the shank portions. Since the overhang length of the tools affect the radial throw due to the tilt errors, the overhang length between different tests were kept within 5 μm. For this purpose, the tube microscope is used to determine the edge position of the sample attached to the spindle, and subsequent adjustments to the attachment length are made until the overhang length is within $\pm 5\mu$m of the desired length of 15 mm. Before attaching each tool to the collet, and prior to taking each measurement, the tools are cleaned with pure ethyl alcohol using foam swabs.

The angular orientation of the spindle, θ, must be recorded simultaneously with the radial throw measurements. This is critical not only for correlating the radial throw with the rotation angle, but also for synchronizing separate measurements from multiple axial locations, as required for the determination of the tilt angle. For this purpose, an infrared (IR) sensor (Monarch Instrument, IRS-W) with a binary voltage output of 0 V or 5 V is used. The sensor outputs a 5 V signal when the infrared light is reflected from the surface to the sensor, and the signal sharply drops down to 0 V when a non-reflective surface, such as a small engraved mark, is encountered. On each tool shank, a 200μm-wide reference mark parallel to the tool-axis (see Fig. 4.4 in Sec. 3.3) was created using laser engraving (LPKF ProtoLaser U3). For this mark width, a sharp voltage drop occurs within two sampling points of the IR sensor, corresponding to a response time of 2 x 10^{-7} seconds. By tracking the voltage-drop location along the measured rotating surface, the start and end of each revolution can be detected with an angular resolution better than 0.08 deg. for spindle speeds up to 130 krpm. The "reference" angle, θ_{IR}, measured by the IR sensor is directly related to the rotation angle θ, which is defined based the reference (first) cutting edge of the tool. The relationship between these two angles are described in the following section.

Although the cooling system retains the coolant temperature within $\pm 2°$C, this small temperature variations could still cause variations to radial motions of the spindle [24]. To assess the effect of spindle (coolant) temperature and the associated thermal cycles on radial throw measurement, a miniature resistance temperature detector (RTD, with $\pm 0.1°$C accuracy) is integrated into the coolant outlet line at 50 mm from the spindle outlet.

4.2.2 Data collection and post processing

Although the radial throw includes many frequency components, in the majority of UHS micromachining spindles, the radial motions are dominated by the one-per-rev components. As such, in this work, we focus on the one-per-rev (fundamental) component of the radial throw. In this section, we describe the post-processing of the measured data for obtaining one-per-rev radial throw magnitude and orientation at *any* location along the tool axis.

The radial throw variations due to thermal cycling were first assessed. For all the measurements presented in this work, the spindle was thermally stabilized by operating it for a 30 min warm-up period prior to any measurements. After the warm-up period, the thermal fluctuations and the associated changes in radial throw (at $z = 5$ mm) within a thermal cycle were obtained at two speeds. The temperature fluctuations follow a cyclic pattern with a period of 16 mins for 60 krpm and 8 mins for 120 krpm, respectively. Within each cycle, the fundamental component was seen to vary less than ± 42 nm at 60 krpm and ± 90 nm at 120 krpm, respectively. The variations in x and y directions were within 5 nm of each other. In reporting the results below, we provide the radial throw values obtained by averaging five measurements that are uniformly distributed within the entire thermal cycle for the selected spindle speed.

To determine the radial throw of the rotational axis at a given z position, the radial motions from the x and y directions at two separate axial positions (z_1 and z_2) of the tool shank must be measured while the tool is rotated at the selected speed. The angular orientation θ_{IR} is simultaneously obtained from the IR sensor measurements. A LabVIEW$^{\mathrm{TM}}$ code was written to manage and synchronize the measurements.

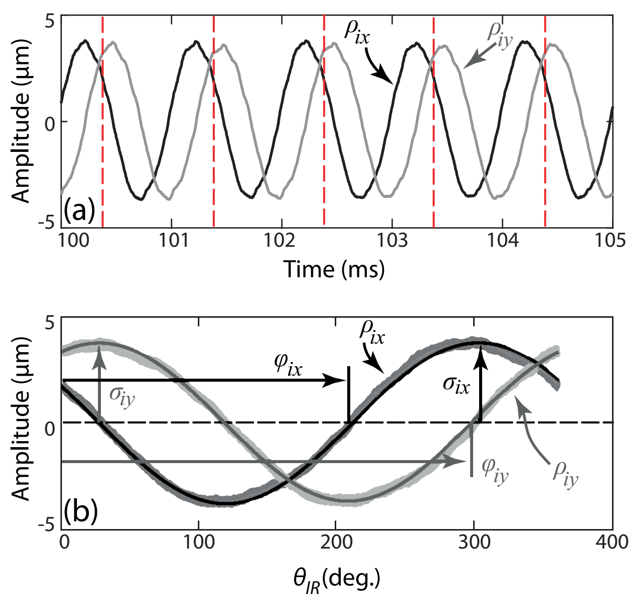

Figure 4.2: *The post-processing steps to obtain amplitude and phase of best fit sine: (a) raw displacement data along the x and y axes as ρ_{ix} and ρ_{iy}, respectively, (b) cycle-by-cycle averaged data, and the sinusoidal fit to obtain amplitude and phase of displacement components along x and y axes.*

The construction of radial throw from the measurements involves several post-processing steps before using the formulation described in the previous section. First, a 10 Hz non-causal high-pass filter is used remove any LDV-related drift from the measured displacement data. Second, the IR sensor data is used to identify each rotation cycle (dashed lines in Fig. 4.2(a)) on the measured displacements. Third, the displacement from at least 500 cycles are superimposed to obtain the displacements in the angular domain as seen in Fig. 4.2(b). In this step, the angles (θ_{IR}) calculated from the IR sensor are transformed into rotational angle θ using the approach outlined below. Fourth, following the formulation in [10], the synchronous motion at a given rotation angle is calculated from the mean of the superimposed data at that angle. A sine function is then fitted to the synchronous motion in the least square sense to extract the amplitude (ρ_{ix}, ρ_{iy}) and phase (φ_{ix}, φ_{iy}), of the fundamental (one-per-rev) motions for each of the two measurement planes $i = 1, 2$ (see Fig. 4.2(b)). The obtained amplitude and phase values are then substituted in the formulation to obtain the radial throw magnitude and orientation of an axis or of a cutting edge at any axial plane z.

4.2.3 Determination of the rotation angle

The rotational angle, θ, is defined as the angular orientation of the reference cutting edge at the bottom of the tool—labeled as the *first* cutting edge—and is zero when the first cutting edge is passing through the positive x axis. Since θ cannot be directly obtained during the experiments, the angular orientation is measured with respect to the reference mark using the IR sensor data. In this section, we describe an approach for transforming the measured angular orientation θ_{IR} to the rotation angle θ.

Figure 4.3 depicts a radial throw measurement. The IR sensor is located at an angle λ from the x axis, and the angle β identifies the orientation of the first cutting edge with respect to the reference mark. The rotation angle θ can be calculated as $\theta = \theta_{IR} + \lambda + \beta - 2\pi$. Thus, obtaining θ from θ_{IR} necessitates determining the angles β and λ.

The angle β indicates the relative orientation of the first cutting edge to the reference mark on the tool shank. As such, β is a property of the particular tool (with the reference mark) and is independent from the rotation angle. To find β for the micro tools used in our experimentation, a focus-variation microscope (Alicona G4 Infinite Focus) is used (see Fig.-4.4). The microscope is equipped with objectives up to 100X magnification and with a high-precision rotation unit that provides roll and pitch motions. First, the microtool is attached on the rotation unit, and the alignment of the reference mark with respect to the edges of the tool shank is measured. Considering less than 500 nm of form error on both tools, this measurement indicated that the reference mark is aligned with the tool axis within 0.5 deg. Second, with the help of the microscope software, the orientation of the rotation unit is adjusted using micrometers to align the reference mark with the lateral direction of the field of view within 0.1 deg. This position was set as the reference position of the rotary stage. Third, the rotation unit is used to apply a 90 deg. rotation about an axis perpendicular to a plane created by the reference mark and the tool axis. This makes the field of view to be normal to the tool axis, thus enabling viewing the bottom (cutting edges) of the tool. And fourth, the angle β is measured as the angle between the horizontal axis (where the reference mark was aligned) and the first cutting edge (see Fig.-4.4(c)). For each tool, the measurement is repeated five times, which indicated that the angle β is determined within ± 0.2 deg. using this approach.

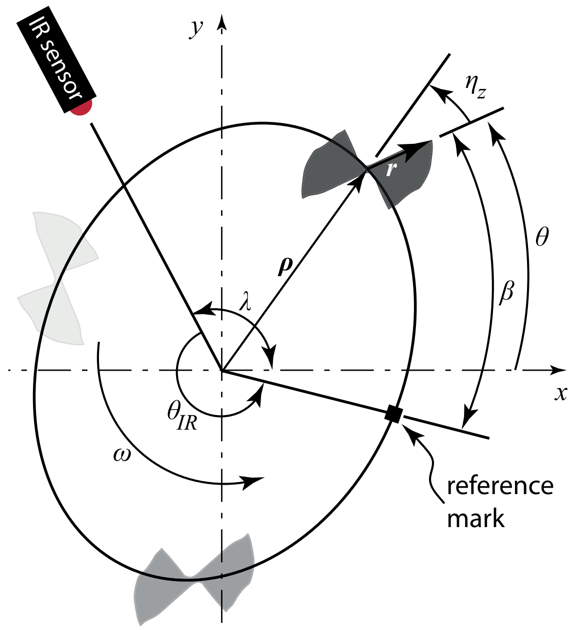

Figure 4.3: *$x - y$ plane at tool-tip to obtain orientation of radial throw with respect to cutting edge of the tool. For clarity, the cutting tool is drawn at a much smaller dimension than the magnitude of radial throw.*

To determine the angle λ (the orientation of the IR sensor with respect to the x axis), the x-axis LDV and the IR sensor are simultaneously used to measure the orientation of the reference mark. For this purpose, the single axis linear stage is used to move the LDV along the tool axis until the laser spot is centered along the length of the reference mark. For this purpose, the reflectivity of the LDV is monitored to find the two lengthwise ends of the reference mark, and then the laser spot is moved to the center of the two ends using the precision stage. With this configuration, both the LDV (reflectivity signal) and the IR sensor monitors the reference mark. The spindle is then operated at a relatively low speed (30 krpm), and the LDV-reflectivity and IR-sensor data are simultaneously recorded. In the angular domain, the LDV and IR reflectivity measurements are superimposed. The angle λ is identified as the angle between two subsequent signal drops. Measurements at low spindle speeds increase the resolution of angular measurements for a given sampling rate. At 30 krpm spindle speed, this approach enables determining λ within ± 0.3 deg.

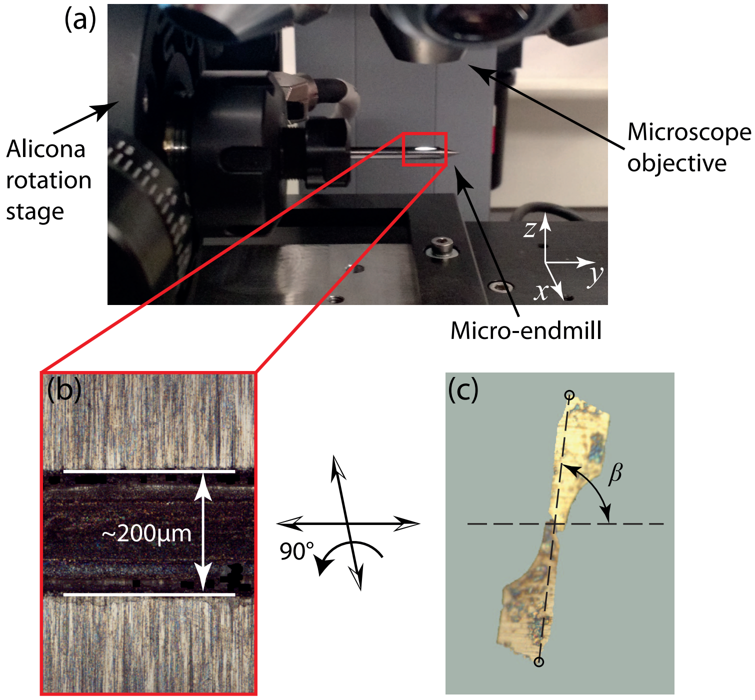

Figure 4.4: *Optical procedure to find angle β between the reference mark and the cutting edge of a micro-endmill: (a) micro-endmill clamped to the rotary stage of the Alicona measurement system, (b) reference mark on the tool shank, and (c) tool-tip view after rotating the micro-endmill by 90 deg.*

4.3 Analysis of Radial Throw and Experimental Validation

The formulation presented above requires measurement of the radial throw at two axial positions along the shank region of a tool to predict the radial throw at the tip region of the tool. Thermal fluctuations, tool form errors, and uncertainties arising from environmental sources induce variations in radial throw measurements, thereby causing variations on the predictions. Furthermore, those variations could change with spindle speed. In this section, we first analyze the variations on radial throw at different spindle speeds. We then experimentally validate the radial throw predictions at different spindle speeds using a microtool blank. It is important to note at this point that, due to the nature of the one-per-rev data, the radial throw follows a perfectly elliptical trajectory (including a circle being a special case of an ellipse).

4.3.1 Variations on radial throw predictions

Since we focus only the one-per-rev component of the radial throw, the post-processing of the data eliminates any variation or uncertainty that does not contribute to the one-per-rev component [10].

In other words, any uncertainty/variation at asynchronous frequencies and at (super-) harmonics of the spindle frequency is removed by the data processing. However, uncertainties/variations at the spindle frequency will cause variations to the radial throw predictions. As described in [26], among different sources of environmental and measurement uncertainties, the largest contribution to the one-per-rev component of the radial throw arises from the vibrations between the laser objectives and the spindle base. Since the spindle is the main driver of those vibrations, they depend on the spindle speeds. As discussed in [24], although controlled in a closed-loop fashion within ± 2 degrees, the temperatures within the spindles follow a cyclic pattern about the set temperature, yielding relatively large variations on radial throw. In microtool shanks, form errors could be as large as (or larger than) ± 500 nm. When measured from a single axial location, the form errors contribute only to the harmonics of the rotational frequency: that is, they do not contribute to the one-per-rev component of the radial throw. However, when the radial throw is measured from two axial positions, the measurements yield a different rotational center (axis average line) for each position. As such, any non-straightness of the tool axis contribute variation to the calculated tilt, and thus, to the radial throw predictions.

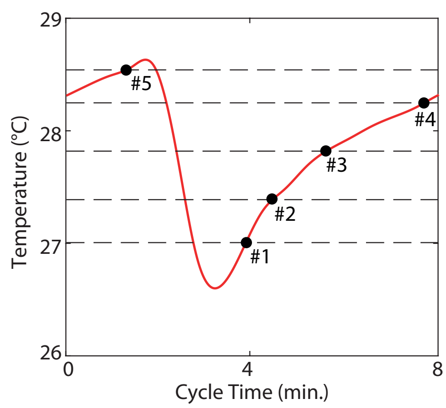

Figure 4.5: *Sample temperature variation with time at 120 krpm spindle speed. Five temperature points selected for radial throw measurements are represented.*

In this work, we followed an experimental approach to evaluate the aforementioned uncertainties and variations on radial throw predictions. The experiments were conducted using a commercial micro-endmill with 254 μm diameter, and the tool was not removed from the spindle during the entire experimentation after being clamped on the collet. *First*, the thermal cycling of the spindle is determined by measuring the coolant temperature on the outlet of the spindle. *Second*, the radial throw is measured from five axial locations along the shank of a commercial micro-endmill at five specific temperatures that span the thermal cycle (see Fig. 4.5). These measurements are done at five spindle speeds (60k, 80k, 100k, 120k and 130k rpm). In each case, the radial throw data were collected for at least 600 revolutions. *Third*, the radial throw data is divided into sections of 20 revolutions, and the post-processing is performed to obtain the one-per-rev component for that data section. Thus, for each given set of axial location, temperature, and spindle speed, at least 30 one-per-rev components are obtained (one per each of the 20-revolution data section). *Fourth*, for each given set of spindle speed and temperature, separate combinations of data are formed. Each combination include data from two axial locations (out of five) and the radial throw from one of the data sections (out of more than 30). All combinations of the data from are then used to predict the radial throw at 15 mm away from the spindle nose. *Fifth*, after compiling the data for each specific temperature, for a given spindle speed, all the radial throw predictions from the five temperatures are combined to determine the radial throw distribution for that spindle speed.

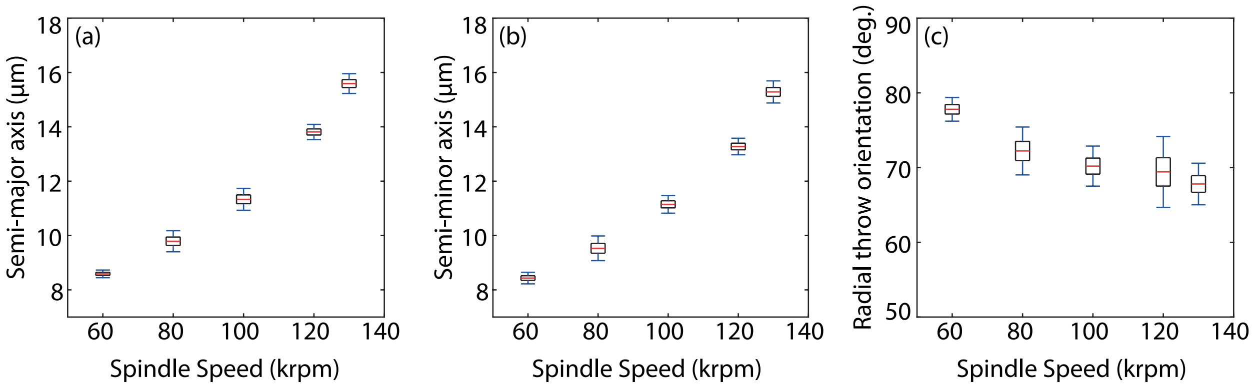

Figure 4.6: *(a) Semi-major, and (b) semi-minor axes and radial throw orientation (η) are presented as a function of spindle speeds.*

Figure 4.6 presents the predicted radial throw by providing the semi-major axis, semi-minor axis and radial throw orientation (at $\theta = 0$) at each of the tested spindle speeds. To represent the variations, a box-and-whisker plot is used. After removing the outliers using $\pm 2.5\bar{\sigma}$ approach [54], the median value is calculated, and the boxes are used to indicate the $\pm\bar{\sigma} = \pm 1.4826 \times \text{MAD}$, where MAD is the median absolute deviation [54]. In the case of normal distribution, $\bar{\sigma}$ is equal to the standard deviation. The whiskers are used to indicate the entire range after the outliers are removed.

As seen in Figs. 4.6(a)-(b), for this particular spindle-collet set, the difference between the semi-major and semi-minor axes is very small with respect to their average value. In other words, the trajectory closely resembles a circle. Since a circular trajectory has an arbitrary major axis, the orientation of major axes exhibits significant variations, spanning the entire 360 deg. in some cases. As such, the orientation of the major axis is excluded from the present analysis. For other spindle/collet combinations, when the trajectory is distinctly elliptical, this parameter should be analyzed. The range of variations in semi-major and semi-minor axes is seen to be within ±500 nm with $\bar{\sigma} = 200$ nm. As a percentage of the median values, this corresponds to a range of ±5% and a $\bar{\sigma}$ of 2%. The largest variation is observed for 80 krpm. The variations on radial throw orientation (at $\theta = 0$) were seen to reach ±5 deg. (at 120 krpm). Considering that these variations include those arising from thermal fluctuations, form errors, and environmental uncertainties, they are deemed reasonably small.

We will now assess the relative contribution from the three sources on radial throw variations ($2.5\bar{\sigma}$). First, to assess the contribution only from the thermal cycling, data from only two axial locations (the first and the fifth) are used, thereby eliminating the variations due to the form error. By using only the median values of radial throw parameters for the entire 600+ revolutions, rather than considering the data-sections, the effect of environmental uncertainties are eliminated. The variations (one-sided) in semi-major axis, semi-minor axis and radial throw orientation due to the temperature cycling at each speed is presented in the form of bar chart in Fig. 4.7. A maximum variation of 85 nm in semi-minor diameter is observed at 130 krpm and a variation of less than one deg. is observed in radial throw orientation across the tested speeds.

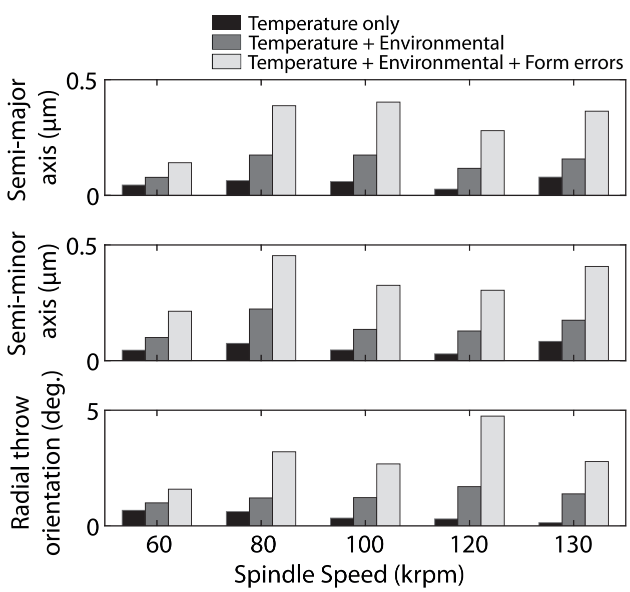

Figure 4.7: *One-sided variations ($2.5\bar{\sigma}$) due to various uncertainties (temperature, environmental and form errors) compounded one at a time for $z = 15$ mm.*

Next, the contribution of environmental effects as variations from data-section to data-section are added at each temperature step. Cumulative variations resulting from both the temperature and environmental effects are presented in Fig. 4.7. The variation in semi-major and semi-minor diameters increased by approximately 100 nm at most speeds when environmental effects are added.

The variability in radial throw orientation increases by up to 1.5 deg.

Lastly, the effect of form errors are added to the thermal cycling and environmental effects. Addition of form errors increases the variations in semi-major and semi-minor diameters by approximately 200 nm at all speeds except 60 krpm (only 100 nm increase.) Similarly, the variation in radial throw orientation is found to increase by up to 3 deg. at 120 krpm. From the presented analysis, it can be argued that the addition of form errors significantly increased the variations in the prediction of radial throw at the tool tip. Large variations due to form errors are expected because when two axial locations are sufficiently close to each other, small variations in the form will result in a larger variation at the tip because of the resulting larger tilt-angle variation.

4.3.2 The effect of spindle speed on radial throw parameters and associated variations

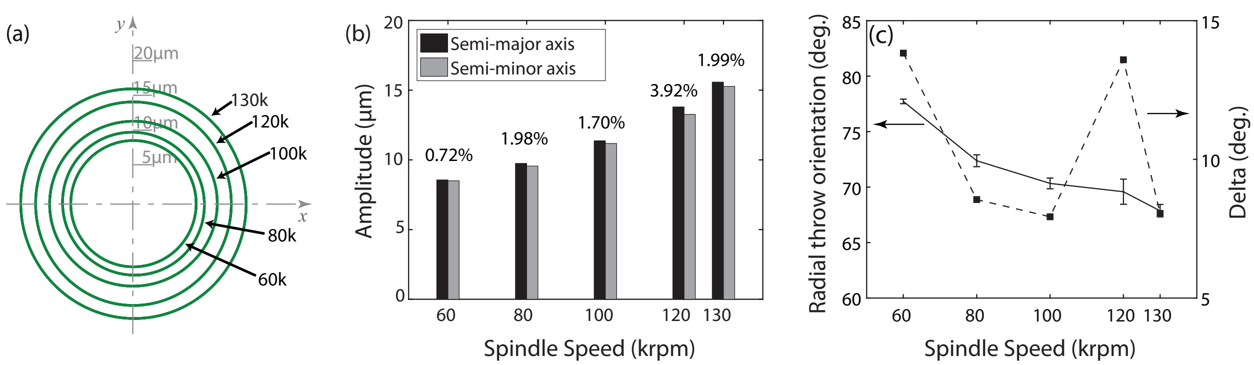

Figure 4.8: *The effect of spindle speed on radial throw: (a) polar plots in $x-y$ plane, where the center of the polar plot indicates the axis average line, (b) ratio of semi-major and semi-minor axes (as a ratio of their average), and (c) trends in radial throw orientation, η and angle between tool-axis and eccentricity in $x-y$ plane, δ. The presented data corresponds to $z = 15$ mm.*

Spindle speed directly affects the radial throw through the rotating eccentricity effect. This includes two components: the increase in radial force due to the rotating eccentricity, which changes with the square of the frequency of rotation, and the change in effective stiffness due to the speed-dependent dynamic response of the spindle. Later, we will discuss the effect of dynamic response by using the frequency response functions obtained from the spindle through modal testing. In any case, the effect of spindle speed on radial throw could be significant.

The effect of spindle speed on radial throw magnitude is presented in Figs. 4.8(a)-(b). For this figure, the data measured from the microtool is used and the radial throw trajectories at 15 mm away from the spindle nose are predicted. Fig. 4.8(a) provides the polar plots of the radial throw, and Fig. 4.8(b) provides the median values of semi-major and semi-minor axes (as a ratio of their average) at different speeds. A significant increase in radial throw magnitude (both semi-major and semi-minor axes) is observed. Indeed, the radial throw magnitude almost doubles from 8 μm to 16 μm when speed is increased from 60 krpm to 130 krpm. The largest difference in major and minor axes is seen at 120 krpm at 3.92%: the trajectories at 60 krpm, 80 krpm, 100 krpm, and 130 krpm may be considered circular. The trajectory at 120 krpm is somewhat elliptical, but still quite close to a circular.

Figure 4.8(c) shows the effect of spindle speed on radial throw orientation (solid line). The radial throw orientation is seen to decrease with increasing spindle speed. The radial throw orientation is determined from both the magnitudes of the radial throw at two measurement planes, and the relative phase between the two radial throw trajectories. In other words, the orientation of the radial throw depends on not only the eccentricity and tilt, but also relative angle between the two. In our formulation, this relative angle is represented at the spindle-nose ($z = 0$) plane by angle δ (the dotted line in Fig. 4.8(c)). For the present case, δ was seen to vary between 7.93 deg. and 13.83 deg. across tested speeds, and the magnitude of eccentricity (not shown) increased from 3.65 μm at 60 krpm to 7.49 μm at 130 krpm. These combination of parameters resulted in a decrease in radial throw orientation by approximately 10 deg. from 60 krpm to 130 krpm. When the radial throw trajectory is elliptical, the radial throw orientation also varies with the rotation angle because of the difference in the rotational speed of the angle θ and the radial throw ρ. For 120 krpm, the variation in radial throw orientation was seen to be within ± 2 deg. within a rotation.

4.3.3 Experimental validation of radial throw predictions

A set of experiments is conducted to validate the presented approach by comparing the predicted radial throw to that directly measured from the tip portion. Since the flutes on a micro-endmill preclude measurements from the tip portion, a custom precision-ground carbide microtool blank with a cylindrical tip portion (3.125 mm shank- and 1.5 mm tip-diameter) is used for the validation experiments.

To account for the uncertainties and variations, the same experimental approach described above for the micro-endmill is performed here for the tool blank. The only difference is that the measurements are obtained from eight (instead of five) axial locations along the shank portion, since the longer length of the tool blank allowed measuring from more axial locations. The radial throw at the tool tip (17.63 mm from the spindle nose) is measured for at least 600 revolutions, and the data is processed by using 20-revolution data sections to incorporate the variations in the measured radial throw. The formulation is used to predict the radial throw at the same location, along with the associated variations.

Figure 4.9 shows the semi-major axis, semi-minor axes, and the orientation (at $\theta = 0$) of the measured (black dots) and the predicted radial throw at the tip, where the predictions indicate the entire data range after removing the outliers. Since there are no cutting edges to use as a reference for the radial throw orientation, we used the reference mark as the reference position in the calculations. The predictions include all the variations due to thermal fluctuations, form errors, and environmental uncertainties, including a median value, $\pm\bar{\sigma}$ variations about the median (indicated with the box), and the entire data range (indicated with whiskers) after removal of the outliers. The maximum variation ($2.5\bar{\sigma}$) in measured data is found to be 150 nm for both semi-major and semi-minor axes, and 0.5 deg. for radial throw orientation. Since the variation in measured data is reasonably small compared to the that of the predictions, only the median values are plotted in Fig. 4.9. It is noted that the predictions and measurements from the tool blank demonstrated the same trends (e.g., increased radial throw with increased speed) as those from the micro-endmill.

As seen in the Fig. 4.9, all three radial throw parameters are predicted accurately, since the measured data falls within the median $\pm\bar{\sigma}$ ranges. The largest errors between the median values of the prediction and the direct measurements were 3.5%, 1.5%, and 0.3 deg. for the semi-major axis, semi-minor axis, and radial throw orientation, respectively. Based on these results, we conclude that the radial throw parameters are predicted accurately using the presented approach.

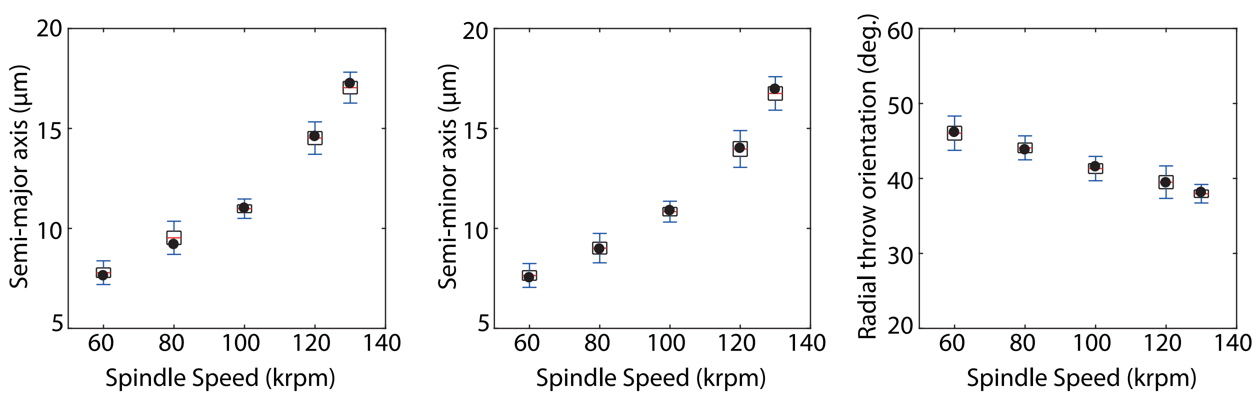

Figure 4.9: *(a) Semi-major, and (b) semi-minor axes and radial throw orientation (η) are presented as a function of spindle speeds for tool-blank at 17.63 mm. The black dots represent the median of measured values.*

4.4 The Effect of Tool-Attachment Reproducibility on Radial Throw Parameters

As outlined in the literature [24, 55], the nature and precision of micro-tool/collet/spindle interfaces strongly affect the radial throw (and error) motions, and this effect is largest for the one-per-rev component. In this section, we present a statistical analysis on the changes of radial throw parameters due to repeated attachment-detachment cycles of the tool to the spindle. To isolate the variations arising only due to the attachment, the study is conducted at a single spindle speed (60 krpm), at a constant temperature within the thermal cycle (27 deg.), from only two points along the shank of the micro-endmill, and without data-sectioning (that is, using the entire 600+ revolutions rather than 20-revolution sections). Since the radial throw trajectory closely resembles a circle at 60 krpm, the radial throw is only measured along the x direction, and the y direction radial throw is obtained by applying a 90 deg. phase shift to the x data. The data is collected from 18 attachment/detachment cycles. For each subsequent attachment, the tool is completely taken out of the collet, cleaned with alcohol swabs and slid inside the collet after a random rotation about its axis. While tightening the collet nut, the tool is left untouched to prevent any bias that could be introduced by the operator. The overhang length of the tool is kept at 15 mm $\pm$ 5 μm using a high magnification tube microscope.

We analyzed five parameters: the eccentricity e; the tilt angle ζ; the angle δ between the tool axis and eccentricity in the $x-y$ plane at $z = 0$; the radial throw magnitude ρ_{15}; and the orientation η_{15} at $z = 15$ mm from the spindle nose. Note that the radial throw parameters become independent of the rotation angle θ for a circular trajectory.

Figure 4.10 provides the histograms for each of the five parameters. The Anderson-Darling normality test indicated that all parameters except the radial throw orientation follow a normal distribution with $p > 0.05$. However, the variations of the radial throw orientation span from 0 to 360 degrees which indicate that it can practically take any value. We discuss the nature and source of radial throw orientation variations in the following section. The standard deviations (as a ratio of the mean value) of eccentricity and tilt angle was seen to be 7.4% and 7.3%, respectively. Although there is a significantly larger variation on δ ($\sigma_\delta/\bar{\delta} = 28.8\%$), the effect of δ on the predicted radial throw is indirect and depends on the eccentricity and tilt parameters. As a result, the predicted radial throw magnitude was seen to have a relative standard deviation of 6.8% with respect to its mean value of 8.17 μm. As expected, the attachment/detachment cycles were found to have a significant effect on radial throw parameters.

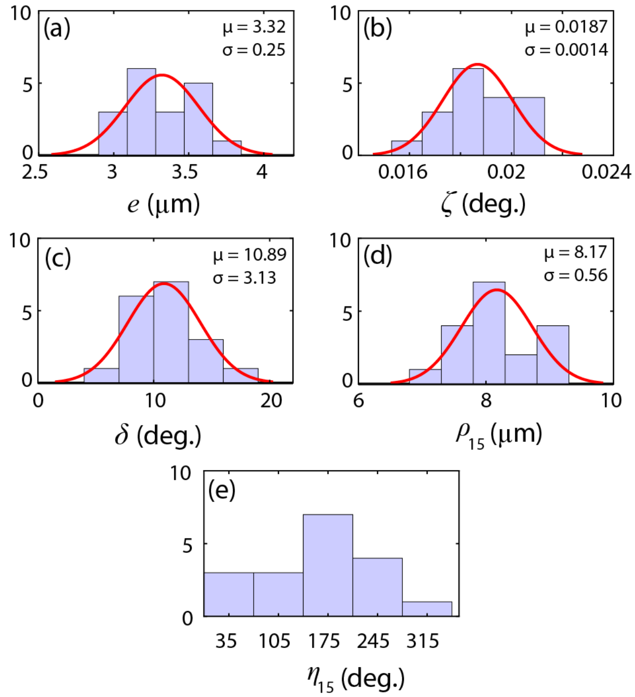

Figure 4.10: *Variation in the radial throw parameters: (a) eccentricity, e, (b) tilt angle, ζ, (c) angle between tool-axis and eccentricity in $x-y$ plane, δ, (d) magnitude of radial throw, ρ, and (e) orientation of radial throw, η, at $z = 15$ mm.*

4.5 Contribution of Spindle, Collet and Tool Interfaces on Radial Throw Orientation

The analysis presented in the previous section showed that the attachment/detachment cycles cause the radial throw orientation to vary considerably, spanning the entire range of 0 to 360 degrees. To better understand the nature and source of those variations, in this section, we present a study where the relative orientations between the spindle rotor (nose), collet, and microtool are specified, and the resulting changes in radial throw orientation are analyzed.

In reality, due to the limitations posed by the spindle and the collet, exact specification of the relative orientations is not feasible. For this reason, approximate orientations relative to the spindle rotor are provided to the collet and the tool as close to target orientations as possible, and then, the actual orientations are obtained through direct measurements. The orientation of the spindle is obtained using a laser sensor pointed at the hexagonal nut that is permanently attached to and rotates with the spindle rotor. Due to the limitations of the laser sensor (Monarch Instruments, ROLS-W) and discontinuous data obtained from the nut's surface, this arrangement has a limited bandwidth of approximately 665 Hz. For this reason, all measurements in this study were performed at a rotational speed of 30,000 rpm (500 Hz). The relative orientation of the microtool with respect to the spindle is obtained by simultaneously measuring the angles of the nut (using the laser sensor) and the reference mark on the tool shank (using the LDV). To obtain the collet orientation, measurement of which from the radial direction is infeasible due to the specific collet geometry and how it is attached to the spindle, the axial surface of one of the four jaws of the collet was painted in black. High resolution images from a digital camera (oriented in the axial direction) are then obtained when the spindle is stationary, and the images are post-processed using MATLAB Image Processing Toolbox to determine the relative orientation between the collet and the spindle rotor. During the measurements, the tool overhang length is kept at 15 mm ± 5 μm.

Table 4.1: Targeted and measured radial throw orientations.

Config	Collet, η_c (deg.)		Tool, η_t (deg.)		Radial Throw Orientation (deg.)	
	Targeted	Measured	Targeted	Measured	η	$\Delta\eta_t - \Delta\eta$
(I)	0	0	0	0.0	0.0	0
(II)	270	280.5	0	350.6	357.1	-6.4
(III)	180	192	0	331.2	343.8	-6.2
(IV)	180	195.6	90	61.4	68.3	5.7
(V)	180	196.6	180	150.8	155.8	2.0
(VI)	270	290.6	270	238.5	248.6	-5.1
(VII)	0	16.2	0	312.8	315.4	7.6

Figure 4.11 illustrates the seven different targeted configurations. In each configuration, different orientations of the collet and the tool are specified with respect to that of the spindle. Table 4.1 gives the targeted and measured orientations of the collet and the tool relative to configuration I. In each configuration, the radial throw was measured from the shank at two positions, and the tool-tip radial throw orientations were predicted. Since our reference for the radial throw orientation is the "first" cutting edge of the tool, when the tool is reoriented by an angle α, the radial throw orientation is expected to change directly by α since our measurement direction remains unchanged (see Fig. 4.3). Any other contributions due to the tool and collet *interfaces* will be superimposed to this direct change in orientation. Accordingly, the last column of Table 1 provides *the difference* between the change in orientation of the tool (from the previous configuration) and change in the radial throw orientation.

From configuration I to II and from configuration II to III, the tool orientation with respect to the spindle was kept approximately constant, while the collet was rotated by approximately 90 degrees

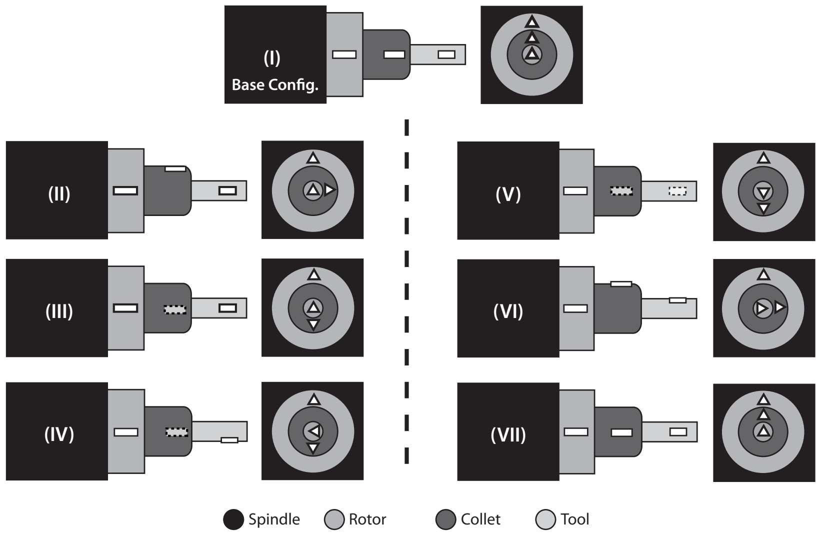

Figure 4.11: *Schematic representation of different spindle-collet-tool configurations. The white lines denote physical marks on each component.*

each time. Based on the last column of Table 4.1, these two 90-degree changes in collet orientation only brought 6.4 deg. and 6.2 deg. change to the radial throw orientation, respectively. From configuration III to IV and from configuration IV to V, the tool orientation is varied by 90 degrees each time while keeping the collet orientation constant (at approximately 180 deg.). Similarly, these modifications only provided 5.7 deg. and 2 deg. change to the radial throw orientation, respectively. From configuration V to VI and from configuration VI to VII, the tool *and* the collet were rotated together by 90 degrees each time with respect to the spindle. The relative change in radial throw orientation was seen to be 5.1 and 7.6 degrees, respectively.

Based on these results, we conclude that the relative orientations between the tool, collet and the spindle induces only small changes to the radial throw orientation. That is, in the previous study when the spindle orientation was arbitrary, we observed that the radial throw orientation spanned the entire 360 degrees. However, when the spindle orientation is kept constant here, the change in radial throw orientation from the relative spindle/collet/tool orientations were less than 7.6 degrees. This indicates that the major contribution to the radial throw orientation arises from imperfections of the spindle itself. For instance, the non-straightness of the spindle rotor, or a misaligned spindle nose (the collet fitting) could cause such radial throw orientations. As such, when the spindle orientation is kept constant between attachment/detachment cycles, significantly smaller variations to the radial throw orientation would be observed. Note that this conclusion is only valid for this particular spindle/collet combination.

Interestingly, this finding indicates that by specifying the orientation of the tool (i.e., the first cutting edge) with respect to that of the spindle, the radial throw orientation may be dictated within a broad range of angles (see the data from the previous section for radial throw magnitude). This may enable determining the most favorable radial throw orientation and setting that value during micromachining to reduce the surface location error, surface roughness, and/or chip thickness variations.

4.6 The Effect of Spindle Dynamics on Speed Dependence of Radial Throw

We previously hypothesized that the changes in radial throw with spindle speed are controlled to a large extent by the dynamics of the spindle through a rotating unbalance response. A comprehensive model to predict this phenomenon necessitates devising a three-dimensional dynamic model of the spindle/collet/tool assembly. Although such a model is beyond the scope of the current work, a simplified modeling approach is proposed here to capture the rotating unbalance effect and the associated dynamic response of the assembly. For this simplified approach, the force arising from the rotating unbalance effect is written as

$$F_e = \begin{Bmatrix} F_{ex} \\ F_{ey} \end{Bmatrix} = m\omega^2 \rho_{0d} \begin{Bmatrix} \mathrm{e}^{j\beta} \\ -j\mathrm{e}^{j\beta} \end{Bmatrix} \mathrm{e}^{j\omega t}, \tag{4.1}$$

where ω is the rotational frequency, m is the *effective* unbalance mass, ρ_{0d} is the *effective* dynamic eccentricity, and β is the *effective* phase between the geometric axis of the tool and the orientation of the *effective* unbalance mass. This rotating force excites the dynamics of the assembly, resulting in deflections—i.e., the dynamic components of radial throw—along the x and y directions. The resulting dynamic portion of the radial throw, ρ_d can be given as

$$\rho_d \mathrm{e}^{j\omega t} = \begin{Bmatrix} \rho_{dx} \\ \rho_{dy} \end{Bmatrix} \mathrm{e}^{j\omega t} = m\rho_{0d}\,\omega^2 \Big[H(j\omega)\Big]_\Omega \begin{Bmatrix} \mathrm{e}^{j\beta} \\ -j\mathrm{e}^{j\beta} \end{Bmatrix} \mathrm{e}^{j\omega t}, \tag{4.2}$$

where $[H(j\omega)]_\Omega$ is the spindle-speed dependent frequency response function (FRF) of the spindle in the form of receptance (displacement/force). This formulation assumes that the FRFs are obtained at different operational speeds Ω and thus capture the rotational effects on dynamics. The radial throw can now be written as

$$\rho \mathrm{e}^{j\omega t} = \begin{Bmatrix} \rho_x \\ \rho_y \end{Bmatrix} \mathrm{e}^{j\omega t} = \big(\rho_0 + \rho_d\big)\mathrm{e}^{j\omega t}, \tag{4.3}$$

where ρ_0 is radial throw measured at the "zero" speed. This zero-speed radial throw only arises from the kinematic motion of the geometric center (rather than the mass center), and during rotations, it can be expressed as

$$\rho_0 \mathrm{e}^{j\omega t} = \begin{Bmatrix} \rho_{0x}\mathrm{e}^{j\alpha_x} \\ \rho_{0y}\mathrm{e}^{j\alpha_y} \end{Bmatrix} \mathrm{e}^{j\omega t}. \tag{4.4}$$

This expression considers that, in general, the zero-speed radial throw follows an elliptical (rather than only a circular) trajectory, including magnitudes $\rho_{0x}e^{j\alpha_x}$ and $\rho_{0y}e^{j\alpha_y}$ in the x and y directions, respectively.

To apply this formulation to our case, two sets of information are needed: the speed-dependent FRFs $[H(j\omega)]_\Omega$, and the unbalance parameters $m\rho_{0d}$, β, ρ_{0x}, ρ_{0y}, α_x and α_y. As shown in our previous work [12], the dynamic response of UHS spindles vary with spindle speed. To obtain the speed-dependent frequency response function, we followed the spindle-dynamics characterization approach presented in [12]. The microtool used for the radial throw measurements was attached to the spindle. The spindle was then rotated at the desired speed, and the dynamic excitation to the system was provided to the microtool shank at 2 mm away from the spindle nose ($z = 2$ mm) in the x and y directions using a custom impact excitation device [56]. The ensuing dynamic response along the x and y directions was measured from the tool shank (at $z = 2$ mm) using the LDVs. This procedure was repeated for the five spindle speeds (60, 80, 100, 120, 130 krpm), and for each speed, the data was post-processed to obtain a 2x2 FRF matrix,

$$\Big[H(j\omega)\Big]_\Omega = \begin{bmatrix} H_{xx}(j\omega) & H_{xy}(j\omega) \\ H_{yx}(j\omega) & H_{yy}(j\omega) \end{bmatrix}, \tag{4.5}$$

which includes both direct and cross components.

The magnitude plots of the obtained speed-dependent FRFs are given in Figure 4.12. Although the rotational effects are most prominent in the vicinity of resonance frequencies (e.g., inducing mode splitting), the changes in spindle speed also cause relatively significant changes to FRF magnitudes at frequencies relevant to this work (see the insets). Since the radial throw measurements in this work focus on the one-per-rev component, the relevant frequencies are those that correspond to spindle speeds used during the measurements, e.g., 1 kHz for 60 krpm.

To determine the unbalance parameters, we followed a curve-fitting approach using the measured radial throw data from two of the spindle speeds (60 and 130 krpm). The total radial throw is given by substituting Eqs. (4.2) and (4.4) into Eq. (4.3). This radial throw equation was first separated into its real and imaginary parts for each of the x and y components. Corresponding to these four equations, the data from the two spindle speeds provided eight values (real and imaginary parts from each of the x and y components.) Since the current form of the equations are not linear, a linear regression approach cannot be used for curve fitting. For a select value of β, however, the

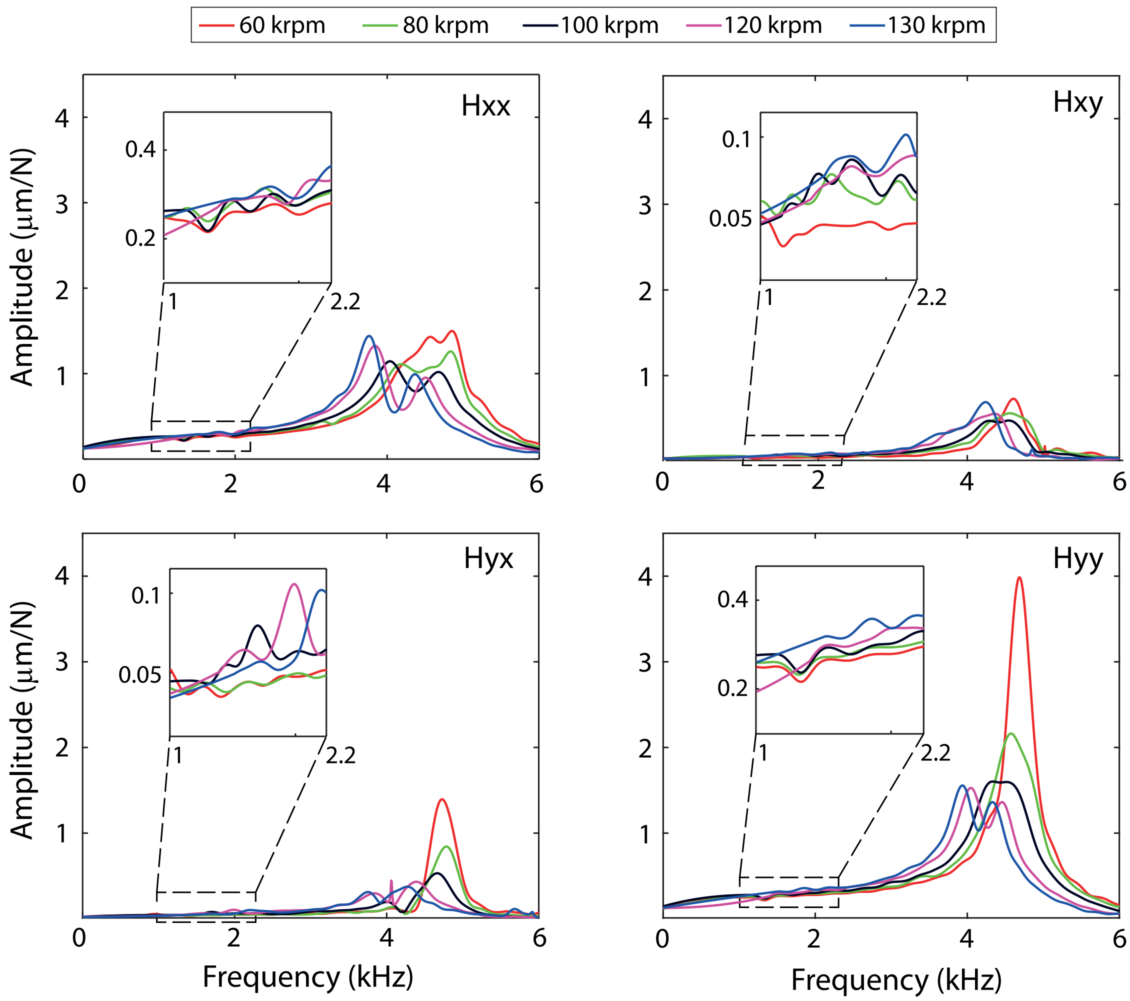

Figure 4.12: *Magnitude of* $[H(j\omega)]_\Omega$ *at different spindle speeds. For references to the colors used in, readers are referred to the web version of this paper.*

equations become linear, and a least-squares curve fitting can be applied. Accordingly, we varied β values from -90 deg. to 90 deg. with 0.1 deg. resolution, and for each β value, a least-squares curve fit was performed to determine the other unbalance parameters. The resulting least-square error for each β value was then calculated, and the final set of parameters is selected as the set which resulted in the minimum least-square error. Using this procedure, the following unbalance parameters were obtained:

$$m\rho_{0d} = 1.196 \times 10^{-7}\text{kg m}, \quad \beta = -0.3\,\text{deg.}, \quad \rho_{0x} = 7.60\,\mu\text{m},$$
$$\rho_{0y} = 7.49\,\mu\text{m}, \quad \alpha_x = 48.51\,\text{deg.}, \quad \alpha_y = -39.65\,\text{deg.}$$

An interesting observation here is that the determined $\beta = -0.3$ deg. seems to indicate that the effective mass center is aligned with the effective geometric center. In further examination, it was seen that the change in β between -1 deg. and 20 deg. resulted in a very small change in the least square error. Therefore, the conclusion about the coincidence of the mass and geometric centers may not be accurate, and this result may be produced by the model equivalency and/or by the curve fitting approach. Another observation is that, as expected, the zero-speed radial throw magnitudes in x and y directions were very close to one another, and the difference between the x and y phase angles is $\alpha_1 - \alpha_2 = 88.16$ deg., which is very close to 90 deg. This indicates that the zero-speed trajectory closely resembles a circle.

Table 4.2 provides measured and calculated (from the presented model, using the parameters given above) radial throw parameters and the error percentage considering the mean value of the measured parameter as a reference. The error in radial throw magnitudes between the model and the experiments is below 4.8%. In all cases, except the y radial throw at 80 krpm, the calculated radial throw magnitudes are within the $\pm\bar{\sigma}$ bounds (refer to Fig. 4.6.) Similarly, the calculated phase between x and y closely follows that measured during the experiments. Overall, it is concluded that the presented simplified model can be utilized to capture the effect of spindle speed on radial throw resulting from the dynamic response due to rotating unbalance.

Table 4.2: A comparison between the measured and the calculated radial throw.

	Radial Throw, x			Radial Throw, y			Phase Difference, y-x	
Speed (rpm)	Measured (μm)	Calculated (μm)	Error (%)	Measured (μm)	Calculated (μm)	Error (%)	Measured (°)	Calculated (°)
60k	8.47 ± 0.23	8.63	1.79	8.54 ± 0.16	8.54	0.02	-89.69	-88.56
80k	9.63 ± 0.69	9.45	1.90	9.68 ± 0.31	9.22	4.77	-90.89	-89.20
100k	11.33 ± 0.43	10.99	2.99	11.16 ± 0.30	11.08	0.67	-89.70	-90.15
120k	13.28 ± 0.31	13.17	0.82	13.81 ± 0.28	14.02	1.53	-89.84	-89.25
130k	15.30 ± 0.41	15.16	0.90	15.58 ± 0.36	15.63	0.30	-90.40	-90.90

4.7 Summary

This chapter presented a comprehensive approach for determination of spindle-speed dependent radial throw of the tool-axis and a novel method to calculate its orientation with respect to the cutting point of the tool. The approach was directly validated though LDV-based measurements, conducted at the tip portion of a custom-made microtool blank. A statistical study was conducted (at 60 krpm) to explore the statistical variation in the radial throw parameters such as eccentricity and tilt angle. Further, the contribution of mechanical interfaces such as spindle/collet/tool towards setting up of radial throw orientation was studied through detailed experiments. Lastly, impact testing on a rotating tool was conducted using custom made IES system to obtain speed-dependent frequency response functions which were used to construct a complex curve-fitting model to predict speed-dependent radial throw. The following specific conclusion were drawn from this chapter:

- The major source of uncertainty in the prediction of radial throw trajectory: form error of the micro-tool/micro-tool blank, introduced a variability amounting to <3% the average magnitude of radial throw and hence it was deemed insignificant. However, for cases where the percent standard deviation is significant, a tool with better circularity will be required for conducting measurements.
- The validation of the presented approach was accomplished by comparing the predicted and the measured radial motions at the tip (z = 17.63 mm) of the micro-tool blank. Validation error between the median values of the prediction and the direct measurements was found to be less than 3.5%, and the measured data lies within $\pm\bar{\sigma}$ for all spindle speeds.
- For the system under test, the average magnitude of radial throw shows a monotonous increases from 8 μm at 60,000 rpm to 16 μm at 130,000 rpm. This implies an absence of natural frequencies of the structure with-in the tested frequency range of 1-2.167 kHz.
- At 120,000 rpm spindle speed, axi-asymmetry in spindle/bearing structure is observed (see Fig. 4.8), highlighting the need for two-axis measurements. FRF magnitudes obtained along the two-axes using impact testing confirm the hypothesis.
- The orientation of radial throw shows a decline (<10 deg.) as the spindle speed is increased from 60,000 rpm to 130,000 rpm. Such small deviations in orientation across speeds allows a good control over orientation dependent process output such as the dimensional error.
- The parameters of radial throw were found to be normally distributed at 60,000 rpm spindle speed. However, the orientation of radial throw (when referenced at cutting edge of the tool) spanned the entire range from 0-360 degree and hence needed further investigation.
- The source of radial throw orientation was studied by precisely tracking the relative orientation of mechanical components such as the rotor, collet and the tool. It was found that the orientation is majorly dictated by the defects coming from the rotor (spindle), and the contribution of collet and tool towards orientation was found to be inconsequential.
- Lastly, a simplified complex curve-fitting model was presented which included the rotating unbalance effect and complex FRFs to predict the speed dependent radial throw of the tool-axis. The maximum error in the radial throw magnitudes between the model prediction and the measurement was 4.77% at 80,000 rpm spindle speed.

CHAPTER 5

Measurement of Radial Throw under External Loading

5.1 Motivation

Although methodologies have been developed for characterizing the error motions (high frequency components of radial throw) of UHS spindles, to date, these methodologies have not involved applying loads to the spindles. Under operating conditions, such loads arise from the micromachining forces. The ISO standard (for axes of rotation metrology [10]) does not explicitly describe a procedure for measurement of error motions of an externally loaded spindle. However, as shown in the case of macro-scale spindles [34], radial (static) loading has a significant effect on the spindle error motions. Correspondingly, we hypothesize that external loading (axial and radial) will have a substantial effect on the error motions of an UHS spindles. As spindle speed also affects the error motions significantly [29, 34], an analysis of UHS spindle error motions should involve measurements at different spindle speeds. Such error motions have a direct impact on the geometric accuracy and surface finish of the micromachined parts.

5.2 Introduction

Being able to apply axial and radial loading to (generally fragile and miniature) UHS spindles at their operating speeds poses considerable challenges. Well-characterized non-contact load applicators with variable magnitudes are required, in addition to using non-contact 2D measurement methods to identify error motions. In addition, a suitable method to remove the form error of the artifact is also required.

Non-contact loading approaches typically involve the use of electromagnets in the form of active magnetic bearings [57] or dedicated loading devices [58–60], to load the tool in a radial direction. Rantatalo *et. al.*[58] used a custom-built contact-less dynamic spindle testing (CDST) equipment consisting of electromagnets to apply dynamic loads to a dummy tool along a radial direction. This dynamic load provided the required excitation amplitude to the tool which aided in the measurement of frequency response functions of the spindle assembly. The results from CDST measurements illustrated the speed dependent system dynamics which may not captured using traditional tap test, typically conducted at 0 rpm. Matsubara *et. al.*[59] used a similar device based on electromagnet to load a dummy tool along a radial direction to measure (radial) static stiffness. From the results, an increase in spindle speed brought a decrease in radial stiffness which is attributed to the increase in centrifugal forces. Wang *et. al.*[60] used an electromagnetic loading device to measure the static and the dynamic stiffness of a rotating spindle. The results show that the stiffness, along with the damping ratio declined with an increase in spindle speed due to an increase in the centrifugal forces. Most of the studies present in the literature uses non-contact loading devices to evaluate the stiffness of macro-scale spindles; none of them studies the effect of loading on changes in the radial throw. Further, these loading devices are massive and requires larger tools/bearings for its functioning and hence are limited to be used on the macro-scale spindles. Thus, there is a need to devise novel non-contact loading approaches to enable loading miniature UHS spindles without the risk of damaging it.

In this work, a non-contact loading approach involving permanent magnets is demonstrated. The magnets for the loading setup are chosen through a validated FEM model such that the magnets can apply a wide range of static loads which are commonly encountered in micromachining process. The effect of axial and radial loading on both the fundamental component and the radial error motions (synchronous and asynchronous) of an UHS spindle are studied. A LDV-based measurement approach is adopted to measure the radial motions from the surface of a precision artifact. To remove the artifact form, a multi-probe error separation technique is adopted. The results are presented in both time and frequency domain, and in accordance with the ISO specifications.

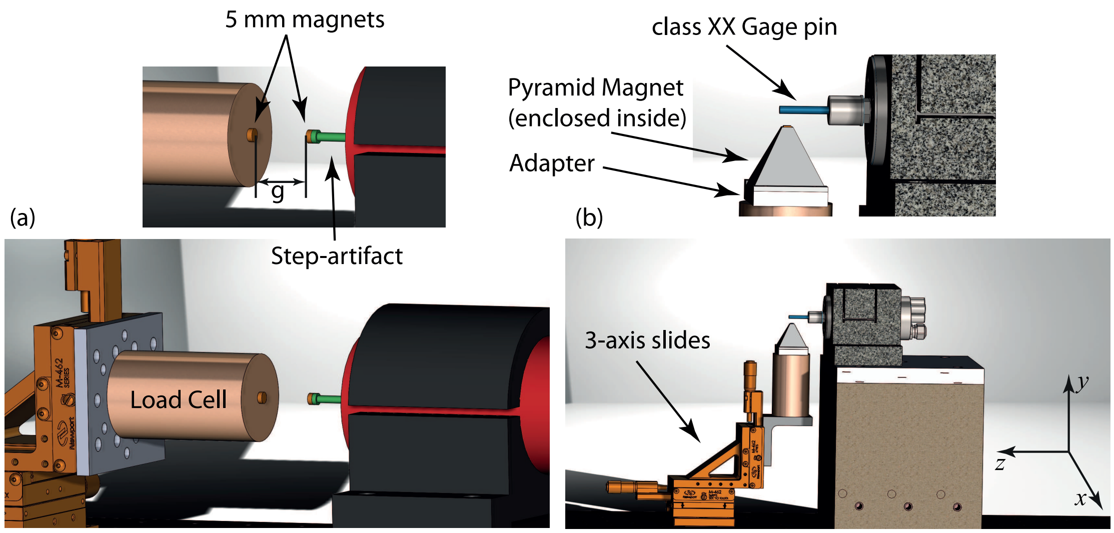

Figure 5.1: *Experimental setup for (a) axial loading, and (b) radial loading.*

5.3 Experimental Methods

5.3.1 Experimental Setup

The experimental setup used for this study is shown in Fig. 5.1. It consists of an ultra-high-speed (UHS) spindle mounted on a vibration isolation table through a polymer granite block. The spindle consists of a pair of hybrid ceramic bearings (IBAG HT 45 S 140) and possesses a maximum speed of 140,000 rpm. The spindle is water cooled where the temperature of the water is maintained within ± 2 °C about the 27°set-point through an external chiller unit. The rotation axis of the spindle is defined as the z-axis (also denoted as axial direction) where x- and y- axes denote radial directions. A custom-made loading setup is installed to apply static loads in axial and radial directions, one at a time. A pair of laser Doppler vibrometers (LDVs) are used to measure simultaneous displacement along x- and y- directions from the rotating surface of custom test artifacts. A third LDV is also used (along r-axis, shown in Fig. 5.2), to aid in conducting multi-probe error separation procedure. An infra-red (IR) sensor is used to obtain revolution marker by sensing a reference mark located on the collet-nut. The thermal state of the spindle is monitored using a temperature sensor fitted to the coolant outlet line. A custom LabVIEW environment is created to simultaneously collect four different quantities : displacements (x, y and r), revolution marker (IR-sensor), temperature of the spindle and static forces from the load cell.

The loading setup consists of a precision Newport-462-XYZ-M ULTRAlign slides with a resolution of 1 μm on each of the three axes. A strain-gage-based load cell (Omega LCM105-10) is used to measure static forces, and is attached to the 3-axis slides as shown in Fig. 5.1(a)-(b). The cumulative uncertainty (linearity, hysteresis and repeatability) of the load cell is 0.09% FSO (Full Scale Output) which corresponds to ±0.09 N. A five-point calibration of the load cell was performed in tension using dead weights, as prescribed in the ASTM standards [29]. After calibration, 1 N corresponded to 0.079 V. The magnet is enclosed inside a 3D printed enclosure, made from VeroWhite. An adapter, made from Aluminum, is used to connect the magnet to the load cell.

5.3.2 Form Error Separation

A method to separate the form of the artifact from the measured radial motions is required to obtain spindle error motions. A number of methods are discussed in literature such as reversal [61, 62], multi-probe [30, 63, 64] and multi-step [29, 43, 65]. Reversal methods are considered true separation methods but they require expensive setup to precisely rotate the orientation of artifact or spindle by 180°. Other two methods, i.e., multi-probe and multi-step suffer from harmonic suppression [66] that affects the accuracy of the separation. However, the effect of harmonic suppression can be reduced by optimizing the angle between the probes or the artifact rotation angles [30, 67]. The multi-step method require one probe but demands relative orientation of artifact/spindle to be changed a few times. This change is orientation and further alignment is facilitated by using a sphere-on-stem artifact [52]. This requirement puts significant restriction on the type of artifact that can be used. On the other hand, in the multi-probe method, three or more probes (with known sensitivities) are aligned precisely to pre-defined angles. Once aligned, this method can be used with any type of artifact and is applicable for real time measurements as it does not require any change in the setup. Therefore, this work implements multi-probe error separation technique with three laser Doppler vibrometer (LDV) probes.

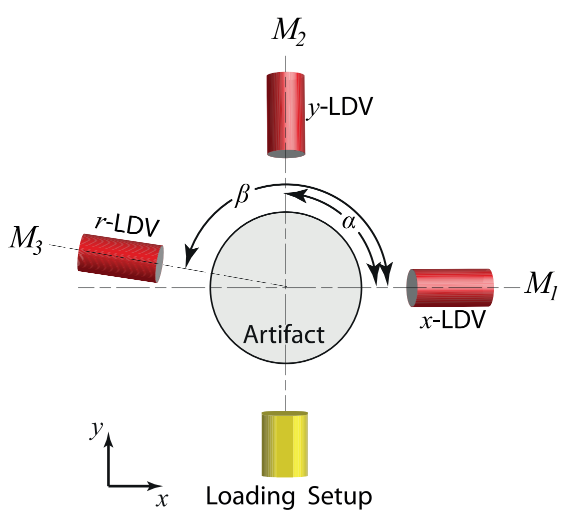

Figure 5.2: *Arrangement of probes in a multi-probe error separation technique.*

A review of the mathematical formulation of the multi-probe error separation technique [67] is presented here. Fig. 5.2 show the arrangement of three displacement probes ($M1$, $M2$ and $M3$) in an $x-y$ plane. Probes $M2$ and $M3$ are offset from $M1$ by angles alpha and beta. The artifact form error and spindle error motion is represented by P(θ) and S(θ), respectively. The component of the spindle error motion is represented by x(θ) and y(θ).

$$M_1(\theta) = P(\theta) + x(\theta) \tag{5.1}$$

$$M_2(\theta) = P(\theta - \alpha) + x(\theta)cos(\alpha) + y(\theta)sin(\alpha) \tag{5.2}$$

$$M_3(\theta) = P(\theta - \beta) + x(\theta)cos(\beta) + y(\theta)sin(\beta) \tag{5.3}$$

$M(\theta)$ is defined as a weighted combination of three measurements using coefficients 1, a and b which are chosen to cancel the x and y direction of spindle error motion in M.

$$M(\theta) = M_1(\theta) + a \cdot M_2(\theta) + b \cdot M_3(\theta) \tag{5.4}$$

where $a = \dfrac{-sin(\beta)}{sin(\beta - \alpha)}$ and $b = \dfrac{sin(\alpha)}{sin(\beta - \alpha)}$. The equations can be represented in Fourier domain as

$$M(k) = P(k) \cdot W(k) \tag{5.5}$$

And with $M(k)$ and $W(k)$ known, we can get artifact form error $P(k)$ by taking an inverse Fourier transform

$$P(k) = F^{-1}\Big(\frac{M(k)}{W(k)}\Big) \tag{5.6}$$

The harmonics k where $W(k)$ is close to zero cannot be determined accurately. Ideally one would like k to be as large as possible by optimizing α and β, which may not be possible due to setup constraints etc. To determine a minimum acceptable value of k, a simple measurement of radial motion from the surface of the artifacts used in this work is conducted. The frequency spectrum of the radial motions revealed that major harmonic components (> 1 nm) lie within first 25 harmonics. To avoid harmonic suppression within 25 harmonics, the angles between the probes α and β are carefully chosen keeping in mind the physical constraint of the existing metrology setup. A threshold of 0.20 is chosen for $|W(k)|$ above which the solution is accepted. According to this criterion, Fig. 5.3 show the favorable and non-favorable angles in green and red, respectively. A favorable set of angles is determined at $\alpha = 90 \pm 2°$and $\beta = 175 \pm 2°$. The displacement probes are roughly aligned within the ± 2 deg. tolerance and the exact angles are measured afterwards by following a procedure described in Section 5.3.4.

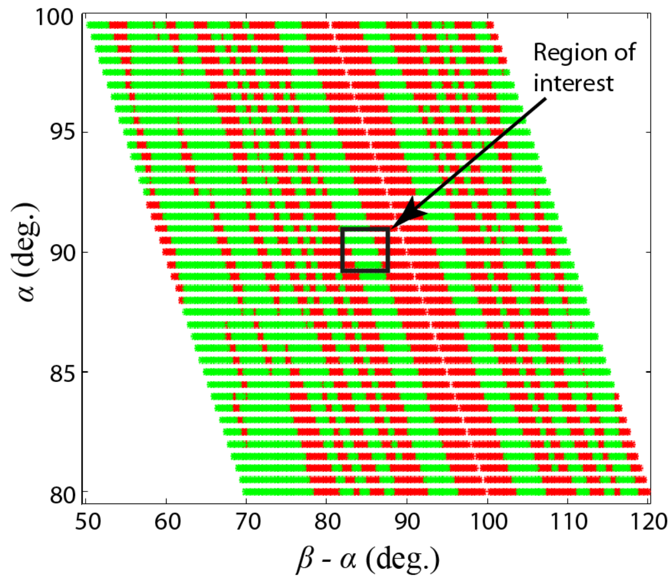

Figure 5.3: *Optimization of the probe angles α and β. Plot of the minimum values of $|W(k)|$ for a combination of $80 < \alpha < 100$ and $150 < \beta < 200$ degs. Green colored regions represent $|W(k)|$ >0.2 and vice-versa for red colored regions.*

5.3.3 Application of Loading

Overall, the requirements from the loading setup are: (1) *selectable* force magnitude spanning the entire force range of interest, (2) *low fluctuations* in forces, and (3) *low profile* so that the position of application is well known. For this purpose, first, a brief comparison between two different classes of magnets (electromagnet vs permanent magnet) is conducted. Based on the performance, permanent magnet is selected and its interaction with the artifact is numerically modeled to aid in the selection of appropriate magnet geometry.

5.3.3.1 A comparison of electromagnet and permanent magnets

To assess the relative performance of both classes of magnets, a comparison of magnetic pull force as a function of air-gap on a 3.175 mm diameter gage pin is made through experiments. For this comparison, magnets with a nominal dimensions of 10 mm were chosen. A commercially available permanent magnet made from Neodymium (pyramid shape, grade N50) with 10 mm square base was used. On the other hand, a DC electromagnet with soft cylindrical core of 10 mm diameter was used. Fig. 5.4 compares the pull force as a function of air-gap between the magnet and the gage pin. Because of the higher forcing capability with a smaller footprint, permanent magnet is preferred over DC electromagnet for static loading applications. Note that, a similar magnitude of force can be achieved with permanent magnet with much larger air-gap which is desired to keep the loading setup sufficiently away from the rotating artifact, for safety reasons.

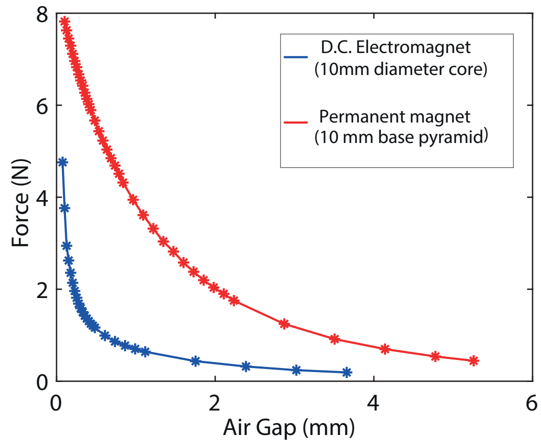

Figure 5.4: *Comparison between DC electromagnet and permanent magnet.*

5.3.3.2 Selection of permanent magnets

A FEM based modeling of magnet-to-magnet and magnet-to-artifact interaction is performed using COMSOL Multiphysics modeling software. The numerical model is used to obtain magnetization and to calculate force generated by permanent magnets. The magnetic field for permanent magnets is best represented by magnetic scaler potential V_m. The underlying physics [68] in the calculation of V_m and the magnetic force per unit volume F is discussed here in brief.

In the absence of electric currents, Ampere's law can be written as

$$\nabla \times \boldsymbol{H} = 0, \tag{5.7}$$

where **H** is magnetic field intensity and "∇" is the gradient operator. The magnetic field of a permanent magnet can be described using magnetic scaler potential V_m, defined as

$$\boldsymbol{H} = -\nabla V_m. \tag{5.8}$$

In the absence of electric current, the Gausss law can also be simplified as

$$\nabla \boldsymbol{B} = 0, \tag{5.9}$$

where **B** is magnetic flux density. Using the following constitutive relation

$$\boldsymbol{B} = \mu_0 \mu_{rm} \boldsymbol{H} + \boldsymbol{B}_r, \tag{5.10}$$

the magnetic scaler potential can be derived; where μ_0 is the permeability of the vacuum, μ_{rm} is the relative permeability of the magnet, and $\boldsymbol{B_r}$ is the remanent flux density in the magnet. Therefore, the magnetization can be obtained from Eqs. 5.7-5.10 as

$$-\nabla(\mu_0 \mu_{rm} \nabla V_m - \boldsymbol{B}_r) = 0. \tag{5.11}$$

The magnetic force per unit volume F is defined using the Maxwell stress tensor σ [69] as

$$F = \nabla \sigma. \tag{5.12}$$

Using divergence theorem, force on a volume V can be calculated as an integral of Maxwell stress tensor over the surface area S as

$$F = \int_V \nabla \sigma dV = \oint_S \sigma \boldsymbol{dS}. \tag{5.13}$$

To set up this physics in COMSOL Multiphysics, the Magnet Fields, No Currents interface is selected. To define the magnet, relative permeability μ_{rm} and remanent flux density $\boldsymbol{B}_r$ are specified in the model. For artifact, only the relative permeability μ_{ra} is sufficient. A free tetrahedral mesh is selected to mesh both the magnet and the artifact. The air-gap g between the magnet and the artifact is identified as one of the key parameters and therefore, variation of magnetic force as a function of g is obtained. This simulation framework can be used to obtain the forces between a magnet-magnet or a magnet-artifact pair.

To validate the simulation, the forces between two axially aligned 3.175 mm diameter cylindrical neodymium magnets (grade N38) at different air-gaps were obtained through experimentation and is compared with the simulations. Fig. 5.5(a) depicts the variation in forces with change in air-gap, where a close match between the experimental and the simulation data is obtained. A slight discrepancy between the curves is seen that could be due to slight misalignment between magnets during experimentation.

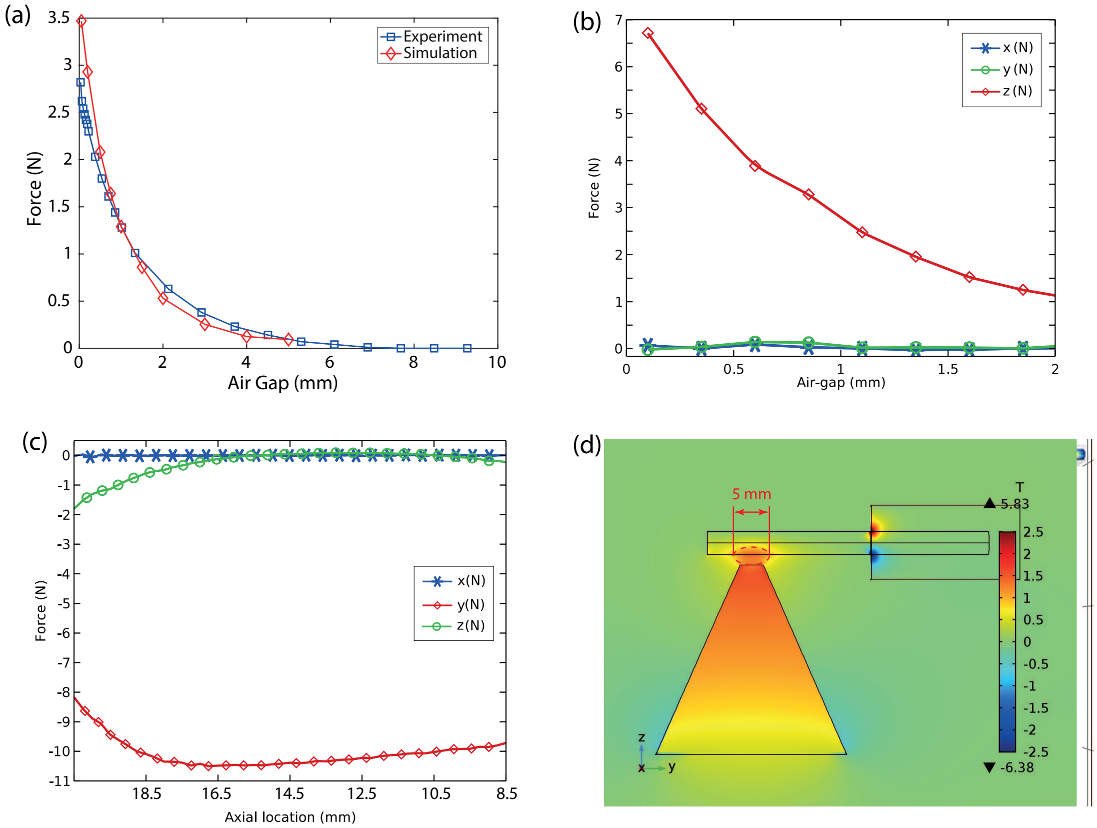

Figure 5.5: *(a) force vs air-gap for a pair of axially aligned cylindrical magnets, (b) force vs air-gap for axial loading, (c) force vs axial location at an air-gap of 500 μm, and (d) magnetic flux density for the selected magnet geometry at 500 μm air-gap.*

Based on a number of micromilling studies [16, 21, 70] on commonly used materials and with reasonable process conditions, the static component of micromilling forces in thrust and radial directions can reach up to 5 N. This peak force should be at the minimum permissible air-gap g, which is chosen to be 0.5 mm for safety reasons. Therefore, the minimum requirement from the axial and the radial loading are a minimum peak force of 5 N at g=0.5 mm. Using the COMSOL simulation framework, various geometries of the permanent magnets are explored. In general, a large magnet that can be accommodated in the setup without interfering components (except artifact) is desirable. This restricts the cross-section area of magnet to be less than 10x10 mm^2 (overhang length of the test artifact being set at 20 mm). Also, attempts should be made to minimize the interaction area with artifact so that the position of application is well known. In this regard, a custom made step-artifact with 3.175 mm shank portion and 5 mm cylindrical tip portion is designed. And to satisfy high energy density requirement within a small footprint, only Grade N50 Neodymium magnets are considered.

Axial Loading To load the spindle in axial direction, a push type loading is required where the tool can be pushed towards the collet. To achieve this, a pair of cylindrical Neodymium magnets (grade N50, 5 mm diameter and 2 mm thickness) are used, in a manner such that same magnetic poles face each other (see Fig. 5.6(a)). One of the magnets is attached to the loading setup and the other magnet is attached to front face of the step-artifact using a high-strength glue (Loctite 480). The magnitude of push force is varied by changing the air-gap, g. A cap on the minimum permissible air-gap g_{min} is placed at 500 μm considering the safety of the spindle. Based on the simulation results presented in Fig. 5.5(b), at g_{min}, the axial push force is expected to be 4 N. To increase the force magnitude, we tried replacing the magnet mounted on the loading setup with a bigger diameter magnet. However, the smaller diameter magnet located at the tip of the step-artifact demagnetized when the bigger diameter magnet came sufficiently close to it. This is because opposite poles create a demagnetizing field for each other where the intensity of the field is proportional to the size of the magnet [71]. Therefore, the axial loading of up to 4 N is achieved with 5 mm magnets (at $g = 0.5$ mm), without any loss of magnetism at either end.

Radial Loading To load the spindle in radial direction, a pull type loading is sufficient. A ferromagnetic test artifact in the form of Class-XX gage pin is used. To select an appropriate magnet, different geometries such as cylindrical, conical and pyramidal were simulated using COMSOL Multiphysics for their forcing capability and compactness. The end result is a pyramid shaped geometry with 25.4 mm square base, 25.4 mm height and 3.1 mm square top. This magnet could apply a peak radial load of 10 N at 500 μm air-gap. Fig. 5.5(c) present radial forces at 500 μm air-gap as the magnet is traversed axially. The artifact overhang is 20 mm and the magnet is referenced at its geometric center. It is observed that the forces along z-axis stays consistent between 16.5 mm and 8.5 mm axial location. This defines the axial range where a pure radial load can be applied to the spindle. The distribution of magnetic flux density, which is used to calculate radial force, using the selected magnetic geometry is presented in Fig. 5.5(d). The axial length of the distributed (peak) force is estimated to be 5 mm.

5.3.4 Alignment and Measurement

The magnet interacts with the test artifact (clamped to the spindle) where the magnitude of applied load is a function of magnets' placement in the 2-D space and the air-gap (g) between the magnet and the step-artifact. To apply loading at a particular location on the test artifact, two-axis adjustment on the loading setup is required. The third axis is used to control the air-gap between the magnet and the test artifact. The selection of axes varies for both axial and radial loading (see Fig. 5.6). In axial loading, a symmetric placement of the magnet with respect to the face of the test artifact in the $x - y$ plane is required. The symmetricity is checked by traversing the slides along the x and y axes while continuously monitoring the force from the load cell. For each axis, the location of maxima results in a symmetric placement. In the case of radial loading, the two-axis alignment is conducted in the $x - z$ plane. For x-axis, a symmetric placement of magnet with respect to the cylindrical surface of the step-artifact is sufficient. The alignment in z-axis is achieved by (1) locating the one end of the magnet to the tip of the artifact using a square with level indicator, and (2) translating the magnet along the negative z-axis to the desired force application position.

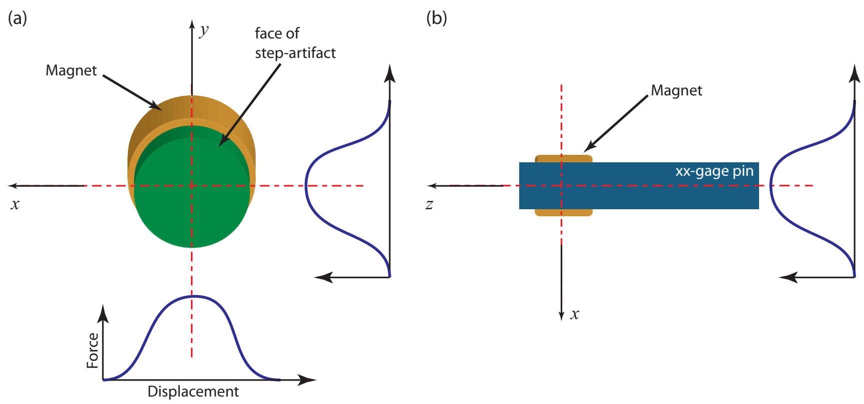

Figure 5.6: *Alignment between magnet and test artifact for (a) axial loading, and (b) radial loading. Note that the magnet on the tip of the step-artifact for axial loading is not shown for clarity.*

The measurements are conducted for two different outcomes: (1) form error removal at zero loading, and (2) radial motion measurements under axial and radial loading. The configuration of the test artifacts for the both axial and radial loading are presented in Fig. 5.7. For each of the experiments, the radial motions are measured from two distinct axial locations, P_1 and P_2. For the case of radial loading, the load is applied at three distinct axial locations indicated by S_1, S_2 and S_3.

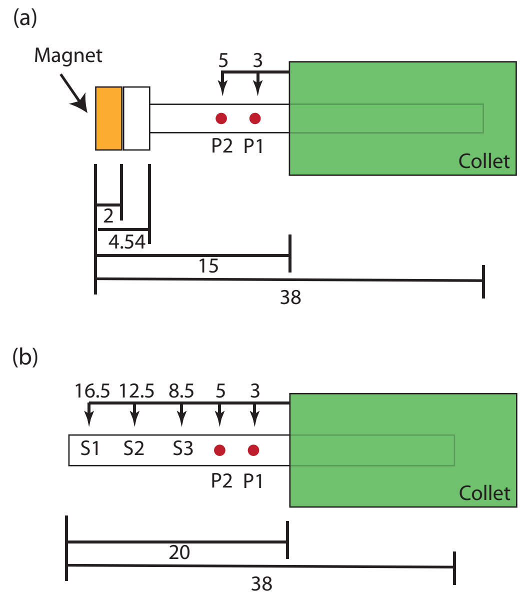

Figure 5.7: *Measurement scheme for (a) axial loading, and (b) radial loading. All dimensions are in mm.*

To perform the form removal using multi-probe technique, the setup requires three displacement probes to align in the same axial plane with specified angles between them (see Fig. 5.2). All three probes are mounted on individual kinematic mounts, providing 6-degree of freedom to facilitate alignment. First, the probes are set perpendicular to the axis average line by maximizing the reflectivity signal coming from a rotating artifact. Second, to align the probes in the same axial plane, an alignment technique discussed in [52] is used which utilizes a Grade 3 sphere for alignment. The probes are made to reflect from the surface of a stationary sphere and are translated along z-axis until the reflectivity signal is maximized. This process ensure that the probes lie in the same axial plane where the plane containing the probes is also normal to the axis average line. Third, to measure the angular distance between the probes, an artifact containing a non-reflective reference mark (straight line of 200 μm width) is used to obtain reflectivity signals from the probes. As the reference mark passes though the sight of probe, a drop in the signal is observed from each of the probes at different times. This difference in time when converted into angular domain, using a pattern correlation algorithm [29], indicates the angular offset between the probes.

5.3.5 Experimental Conditions

The radial motion measurement are conducted with the without loading from both $x-$ and $y-$axes. For axial loading, forces at 0, 2 and 4 N are applied. And for radial loading, forces at 0, 3 and 6 N are applied. A range of spindle speeds were tested between 60-120 krpm, at 10 krpm intervals. For each spindle speed, radial motions are measured from two distinct axial locations, P_1 and P_2, to obtain the changes on both the eccentricity and the tilt.

In case of radial loading, the reaction at the spindle nose not only consists of a radial load but also a moment. To understand the effect of moment on the changes in radial motions, the radial load is applied at three distinct axial locations, S_1, S_2 and S_3. Applying loads at different axial locations results in different moment arm which changes the resulting moment at the spindle nose (see Table 5.1).

Table 5.1: *Radial loading: Effect of moment arm*

Force (N)	Moment Arm (mm)	Moment (N-mm)
0	8.5	0
0	12.5	0
0	16.5	0
3	8.5	42.5
3	12.5	62.5
3	16.5	82.5
6	8.5	85
6	12.5	125
6	16.5	165

5.3.6 Data collection and post processing

For conducting multi-probe error separation, pairwise LDV measurements consisting of (x, y) and (x, z) motions from the surface of the artifact, pulse signal from IR sensor, and temperature measurements from coolant outlet line are simultaneously acquired. For each speed, the data is collected for a time duration of 1 seconds, corresponding to at least 600 revs., after warming up spindle for at least 30 mins. This procedure is repeated for each speed under consideration. At each speed, data is collected at five different temperatures covering the coolant cycle.

A sample measurement and associated data processing at 60 krpm is presented in Fig. 5.8. Fig. 5.8(a) plots the raw radial motions as observed from the $x-$axis displacement probe. The raw motion is separated into three different components [10]: fundamental, asynchronous and residual synchronous components as depicted in Figs. 5.8(b)-(d), respectively.

The residual synchronous motions presented in Fig. 5.8(d) consists of form error of the artifact and the spindle error motions. The residual synchronous motion from three separate probes M_1, M_2 and M_3 are plugged into Eq. (5.4) to obtain the artifact form error using Eq. (5.6). The resulting form error of the artifact is presented in Fig. 5.8(e). The artifact form error is the subtracted from the residual synchronous error motions to obtain the true residual synchronous error motions as presented in Fig. 5.8(f). The pure residual synchronous error motions are typically represented using a polar plot as shown in Fig. 5.8(h) and a synchronous error motion value v is defined as the difference in the radii of the two circles that encloses the motions. The preferred way to present asynchronous error motion is by calculating the standard deviation, as shown in Fig. 5.8(g).

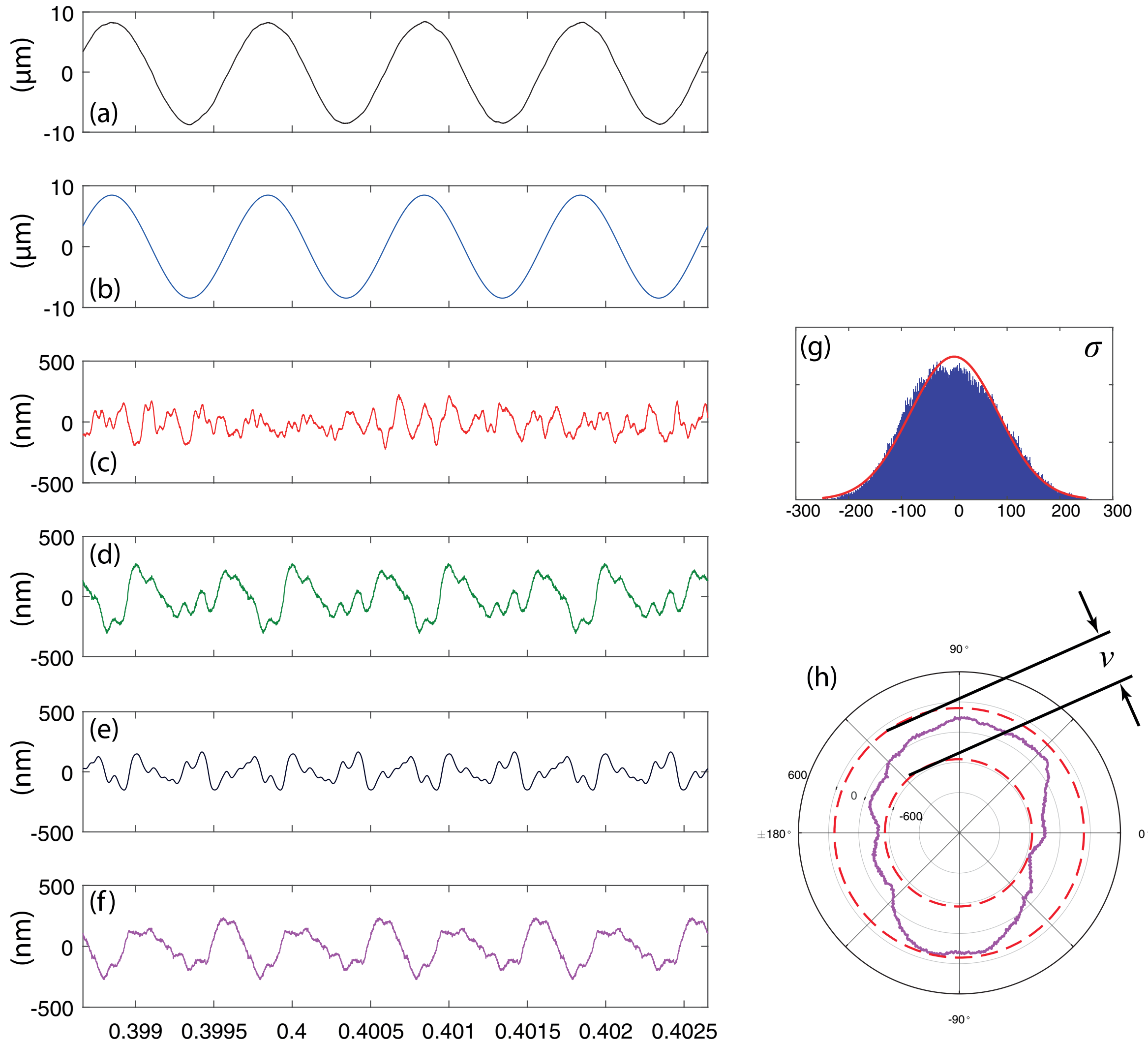

Figure 5.8: *The data processing scheme for a single axis measurement is presented: (a) raw displacement data, (b) one-per-rev, (c) asynchronous error, (d) synchronous error, (e) artifact form error, (f) true synchronous error, (g) standard deviation σ for asynchronous errors, and (h) synchronous error value v.*

5.4 Analysis

5.4.1 Effect of tool-eccentricity on radial loading

Although our intent is to apply a pure static load to the spindle, small magnitude of dynamic forces (mainly one-per-rev) could be generated due to resulting tool-eccentricity at the force application position. The eccentric attachment of the tool to the spindle results in a finite radial offset. This offset causes the air-gap to vary during rotation, thereby altering the force magnitudes. To quantify the magnitude of the dynamic forces generated by this offset, a 3-axis high frequency dynamometer (Kistler 9256C1, specified first natural frequency of 5 kHz) is used. We hypothesize that these dynamic forces are small in magnitude compared to the static forces we intend to apply and hence can be ignored. To test the hypothesis, the dynamometer is installed in the experimental setup to capture the dynamic component of forces during static loading (see Fig. 5.9). It is observed that the oil-air lubrication from the spindle introduces additional noise in measurements at the rotational frequency. To quantify the noise, in a separate experiment, a dummy magnet (3D printed) is attached in place of the actual magnet and the experiments are repeated. Since the dummy magnet does not influence the test artifact in any manner, the forces obtained using the dummy magnet are classified as noise in the measurements.

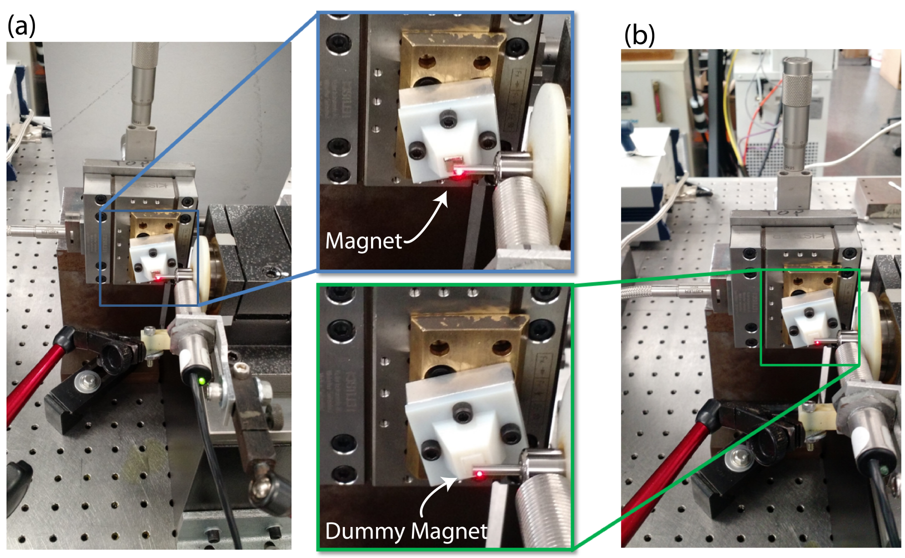

Figure 5.9: *Dynamometer experiments to assess the dynamic forces.*

To conduct the experiments, first, the magnet is translated at the tip portion of the test artifact (Class-XX gage-pin) and this position is noted. Second, the air-gap is varied between 0.5 mm and 6 mm in steps and at each step, forces from dynamometer are recorded for both magnet and dummy magnet. Fig. 5.10 compares the forces along x-axis with and without the magnet. The average magnitude of radial throw (or offset) is measured to be 8 μm at the force application position. The experiments, both with and without the magnet, resulted in similar magnitude forces at rotational frequency. The difference between the forces is within 20 mN (0.4%) for a static load of up to 5 N at 0.5 mm air-gap. Such small values of dynamic forces can be assumed to be negligible for this study.

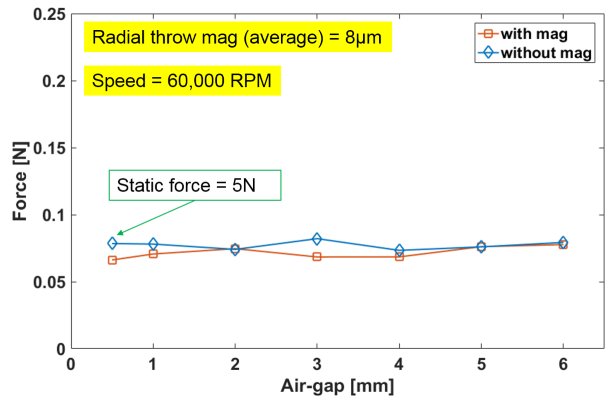

Figure 5.10: *Magnitude of once-per-rev forces both with and without (dummy) magnet at 60 krpm spindle speed.*

5.4.2 Deflections due to radial loading

One-sided radial loading on the test artifact could result in deflection of either the artifact or the spindle or both. To assess the stiffness of the artifact, the Euler-Bernoulli beam theory is used. The Euler-Bernoulli beam theory was also used in [70], where the stiffness of micro-tool was successfully modeled as a cantilever beam. Using this theory, the deflection of a cantilever beam for a concentrated load P at any axial location z is given as

$$\delta(z) = \frac{Pz^3}{6EI} \tag{5.14}$$

Assuming attachment of artifact to collet as a fixed boundary condition (for obtaining the stiffness of Class-xx gage-pin) and radial load as a point force, the stiffness of a cylindrical artifact (3.175 mm diameter) at $z = 16.5$ mm (maximum moment arm, see Sec. 5.3.5) was found to be 692 N/μm. The stiffness of the spindle is quoted to be 21 N/μm and 24 N/μm in axial and radial directions, respectively [7]. On comparison, the stiffness of the spindle is an order of magnitude lower than the artifact, and therefore, the spindle is more likely to deflect on application of force and deflection of the artifact can be assumed to be negligible.

5.4.3 Validation of multi-probe error-separation method

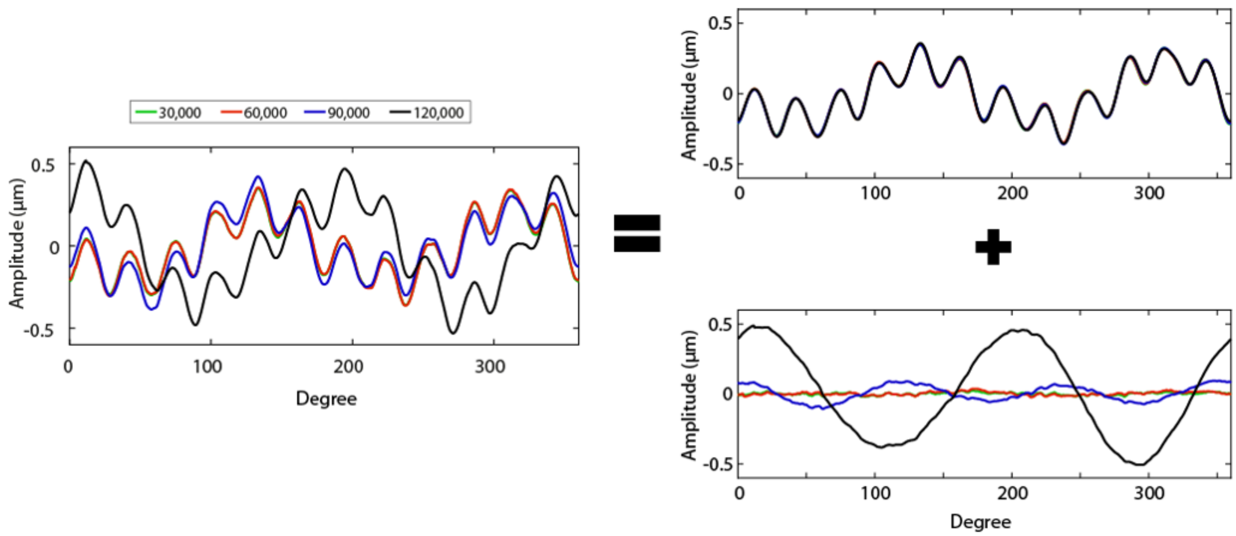

Figure 5.11: *Separation of artifact form and spindle error motions after performing multi-probe error separation technique at four different spindle speeds: (a) synchronous erros, (b) artifact form at all tested speeds (overlapped on each other), and (c) true synchronous errors.*

The multi-probe error separation method is validated by comparing form errors of the artifact at four different spindle speeds at a fixed axial location. Displacement data is collected from three displacement probes ($M1$, $M2$ and $M3$); rotational angle information is obtained through IR-sensor and temperature of the spindle through RTD. The raw displacement data is post-processed to obtain synchronous error motion using a procedure described in [10]. These synchronous error motions are used to obtain artifact form error and spindle error motions (see Sec 2). Fig. 5.11 present artifact form error and spindle error motions at different speeds. Since the (axial) measurement location is kept fixed, the artifact form remains constant at all speeds. The maximum deviation in the artifact form error between different speeds is less than 30 nm. There could be a few reasons for this discrepancy: (1) uncertainty of a few nm due to the synchronous components of structural error motions [26], and (2) gradual axial growth of the shaft, as a result of change in preload or temperature, by a total of 10 μm as the spindle speeds is increased from 60k to 130k rpm (figure not shown) which changes the measurement location on the artifact by the same amount.

5.5 Results and Discussion

This section presents the measurement results from the radial loading. The experiments are conducted at load levels of 0, 3 and 6 N and at three moment arms of 8.5, 12.5 and 16.5 mm.

5.5.1 Effect of radial loading

The effect of radial load for a fixed moment arm (16.5 mm) is analyzed in this section. The measurements are conducted at an axial location of 5 mm from the spindle nose. The measured motions are decomposed into various components using the data processing scheme presented in Sec. 5.3.6.

Fig. 5.12 presents the amplitude of fundamental (or one-per-rev) component of radial throw at different radial loads for a range of spindle speeds. The amplitude of fundamental component is presented for measurement along x- and y-directions, respectively. At 80 krpm, the maximum change of 254 nm (∼2.5%) in average fundamental component is observed along x-direction. Along y-direction, a maximum change of 550 nm in average fundamental component is observed at 120 krpm (∼3.5%). For majority of cases, the change in fundamental component is less than 1 % which can be assumed to be negligible. This is expected because as static loading only brings static shift in the location of axis average line as a result of the finite radial and bending stiffness of the spindle. The attachment error or the dynamic response is not expected to change during pure static loading. Hence, the effect of static loading on the fundamental component of radial throw is considered inconsequential.

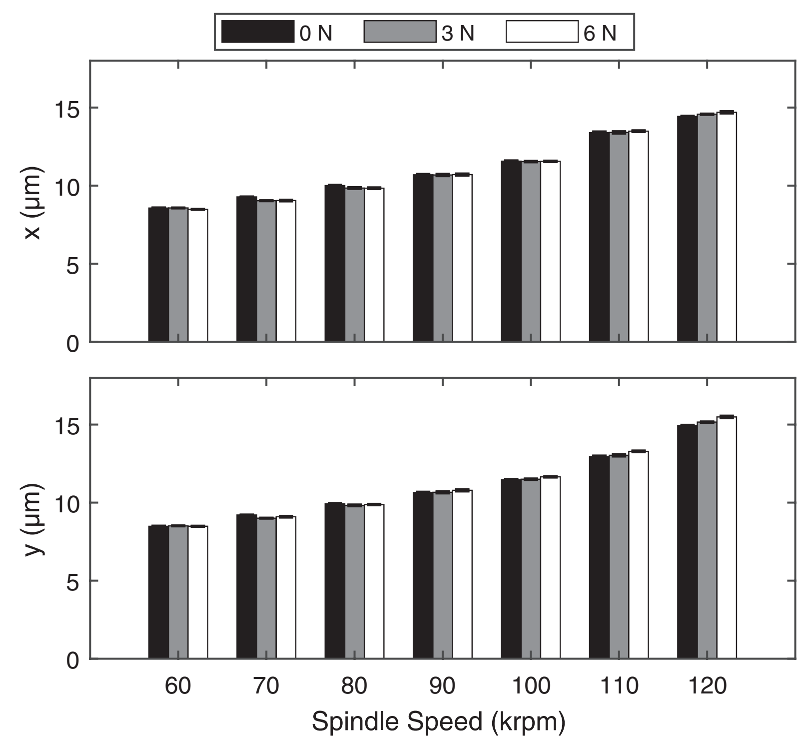

Figure 5.12: *Fundamental (or one-per-rev) component of radial throw along x- and y-axes at varying radial loading levels.*

Fig. 5.13 shows polar plots of synchronous radial error motions at selected spindle speeds of 60, 90 and 120 krpm. Significant differences in synchronous radial error motions are observed at different speeds and at different loading levels. At 60 krpm, the predominant motion along the x-direction changes from a 3-lobe at 0 N to a 2-lobe at 6 N force. For 120 krpm, the synchronous radial error motions does not show a significant change in amplitude on application of radial loading. The trends and the magnitudes are similar for motions along both the x- and the y-direction on application of radial loading.

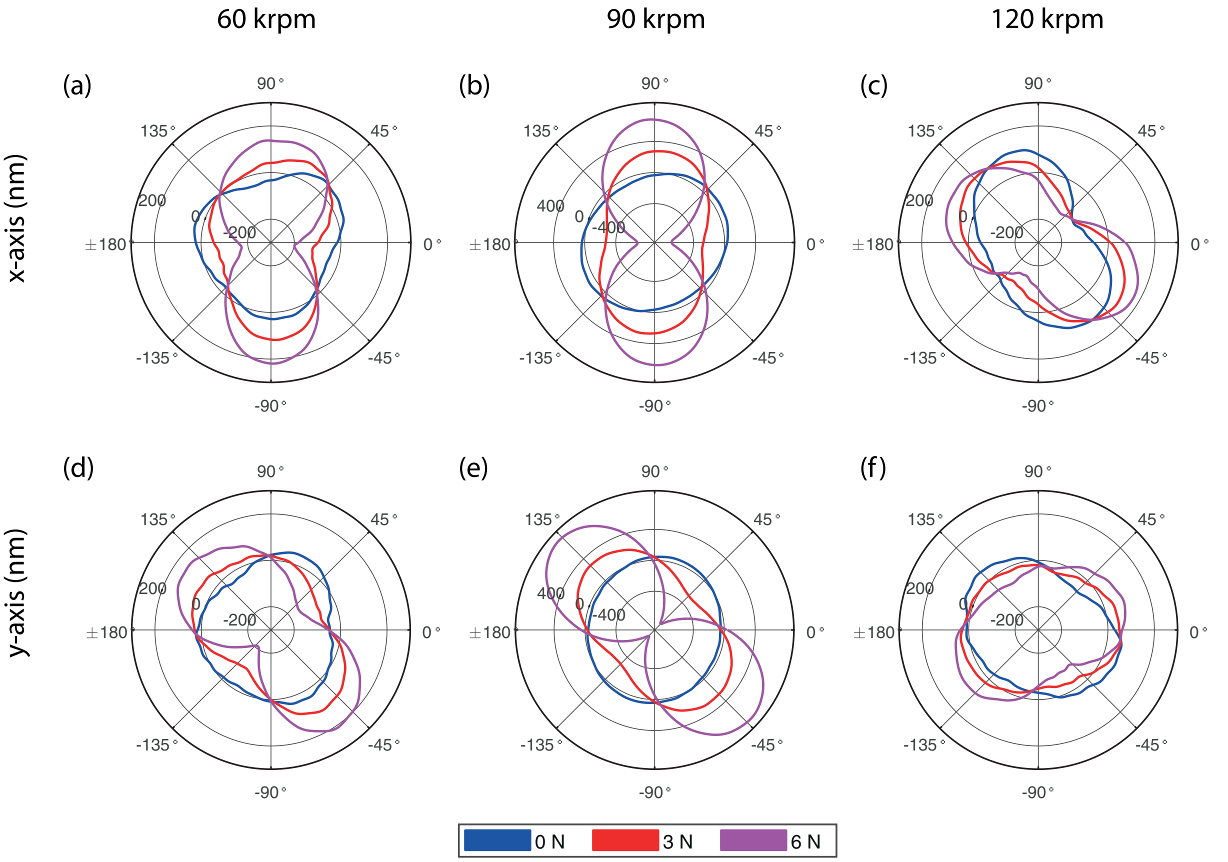

Figure 5.13: *Polar plots of synchronous radial error motions along the x- and y-axes at varying spindle speeds and radial load levels.*

Fig. 5.14 shows the magnitude of the Fourier transforms of the synchronous radial error motions along the x- and y-directions at selected spindle speeds. These bar charts are equivalent to the motions observed in Fig. 5.13. E.g., a 2-lobed shape is represented as 2 cpr in Fig. 5.14. The effect of radial loading is clearly identified as a significant jump in 2 cpr values for both 60 and 90 krpm when a radial load is applied. The 120 krpm spindle speed shows marginal increase in 2 cpr.

Fig. 5.15 shows synchronous radial error motion values along x- and y-directions for a range of spindle speeds. At speeds of 90-100 krpm, the synchronous radial error motion values are greater

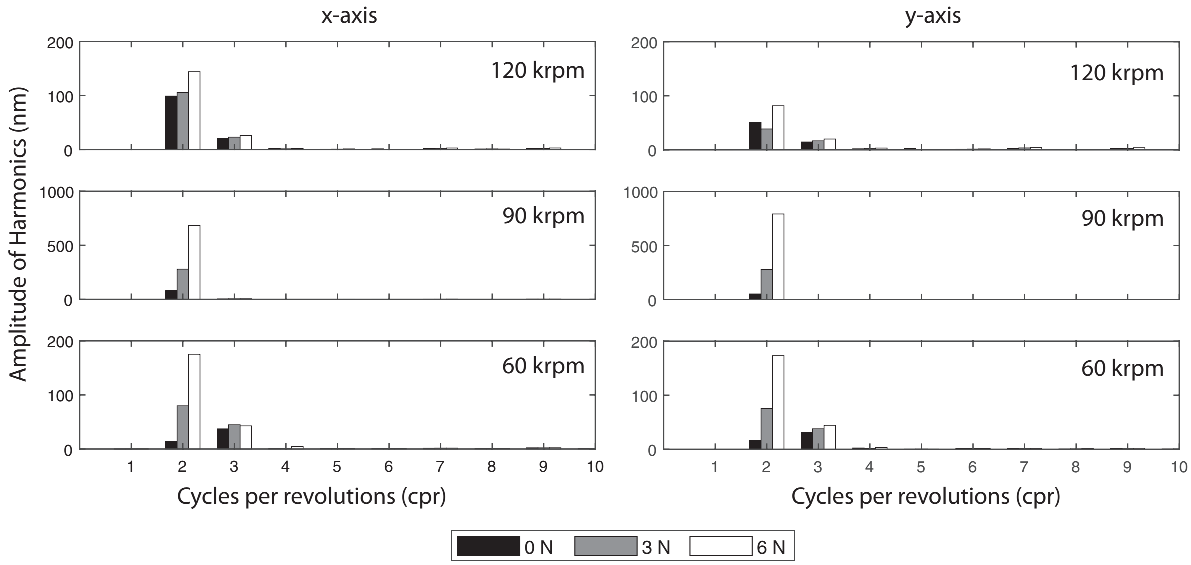

Figure 5.14: *Magnitude of the Fourier transforms of synchronous radial error motion along x- and y-directions at varying radial loads.*

than all other speeds by about 50%. On increase in radial loading, the synchronous radial error motion values are found to increase for all speeds, except for 3 N load at 110 krpm. The increase in the synchronous radial error motion values are dis-proportionally higher for 90-100 krpm spindle speeds when a radial load of 6 N is applied. Both x- and y-directions follow similar trends.

Fig. 5.16 shows the 1σ values as a measure of asynchronous radial error motions. The 1σ values are calculated for motions along both the x- and y-directions. For most speeds, except 110-120 krpm, the change in 1σ values is within 15%. The maximum 1σ values of the asynchronous error motions for x-direction are seen at 80 krpm. However, the amplitude of motion at 80 krpm is significantly lower along y-direction. For all other speeds, the 1σ values are below 100 nm and 150 nm for motions along x-axis and y-directions, respectively.

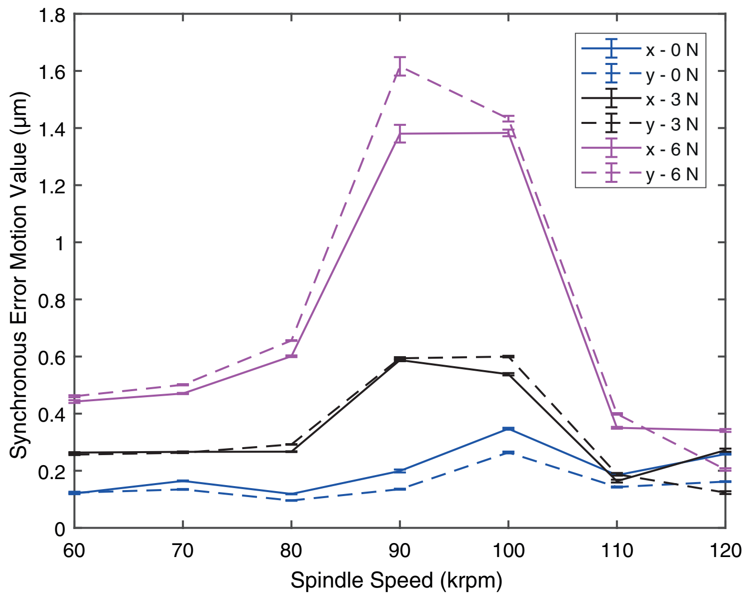

Figure 5.15: *Synchronous radial error motion values along x- and y-directions at varying radial loads.*

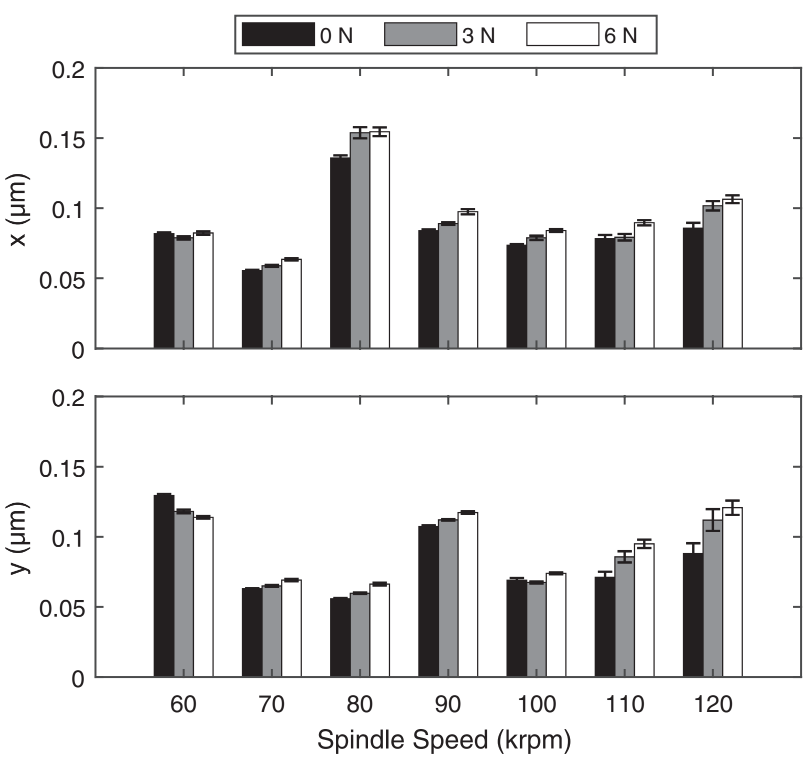

Figure 5.16: 1σ *of asynchronous radial error motion along x- and y-directions at varying radial loads.*

5.5.2 Effect of moment arm

In this analysis, the radial load is kept constant at 6 N and the moment arm is varied between 8.5 mm to 16.5 mm, in three steps. The measurements are conducted at an axial location of 5 mm from the spindle nose. As earlier, the measured motions are decomposed into various components using the data processing scheme presented in Sec. 5.3.6.

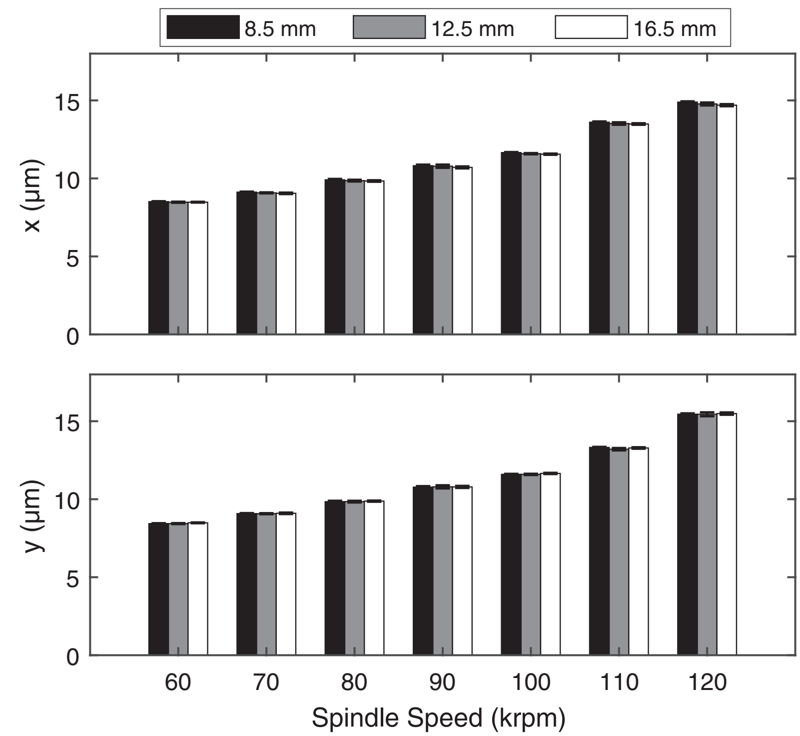

Figure 5.17: *Fundamental (or one-per-rev) component of radial throw along x- and y-axes at varying moment arm.*

Fig. 5.17 shows the variation in the fundamental (or one-per-rev) component of radial throw when a constant force is applied at different moment arms. As expected, for both x- and y-directions, no significant changes in the fundamental components is observed.

Fig. 5.18 shows polar plots of synchronous radial error motions at spindle speeds of 60, 90 and 120 krpm. Significant differences in synchronous radial error motions are observed at 60 and 90 krpm at different moment arms. At 90 krpm, the 2-lobe motion along the x-direction is pronounced when the moment arm is increased from 8.5 mm to 16.5 mm. On the other hand, the synchronous radial error motions at 120 krpm is relatively stable at all values of moment arm. The trends and the resulting magnitudes are similar for motions along both the x- and the y-direction when the moment arm is varied.

Fig. 5.19 shows the harmonic content of the polar plots presented in Fig 5.18. The magnitude

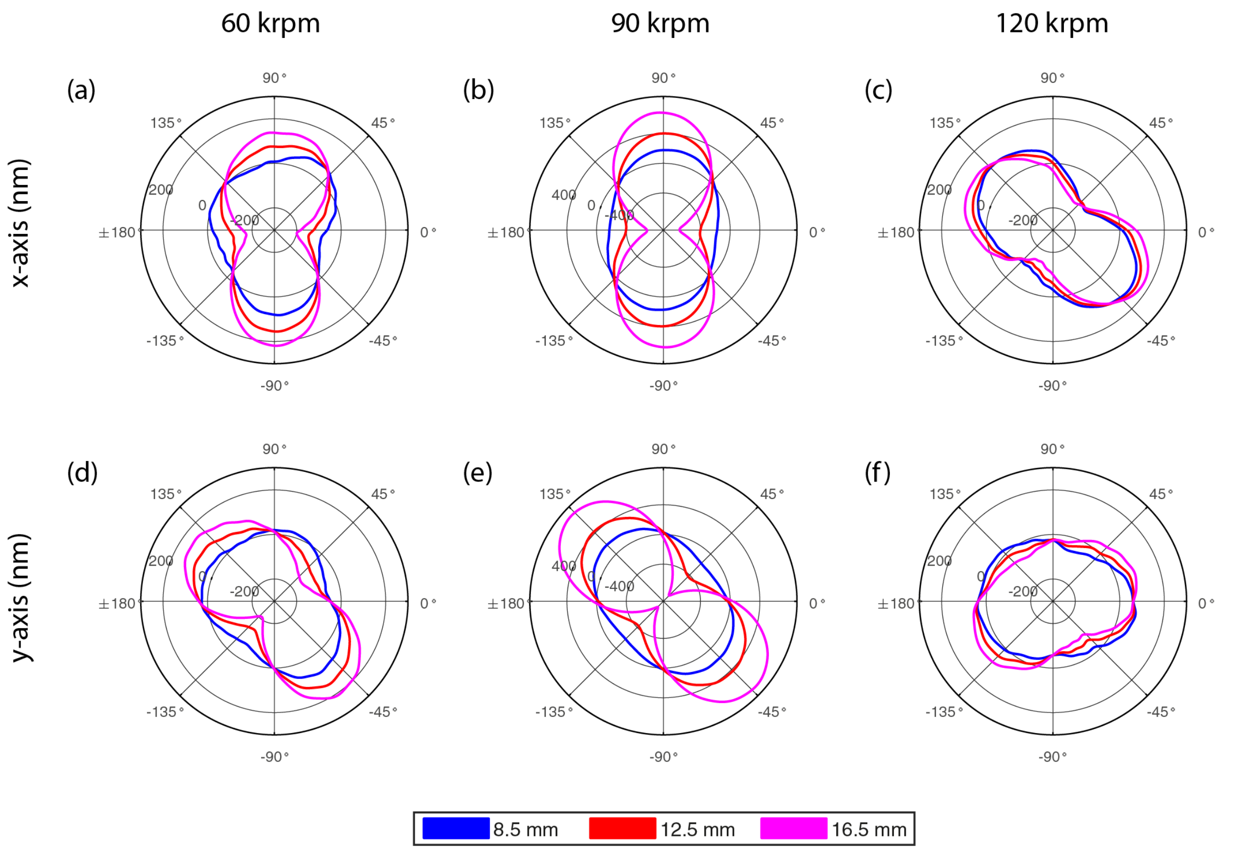

Figure 5.18: *Polar plots of synchronous radial error motions along the x- and y-axes at varying spindle speeds and moment arm.*

of 2 cpr increases linearly with moment arm for 60 and 90 krpm spindle speed. However, the amplitude of 3 cpr remain constant when moment arm is changed. Similar to the case of change in force magnitude (in Sec. 5.5.1), 120 krpm spindle speed shows marginal increase in the amplitude of 2 cpr with an increase in moment arm.

Fig. 5.20 shows synchronous radial error motion values along x- and y-directions for a range of spindle speeds. The trends are similar to one observed when the force magnitude is varied. However, the increase in magnitude of synchronous radial motion is linear, compared to the earlier case where a non-linear increase at 6 N in observed. At speeds of 90-100 krpm, the synchronous radial error motion values are greater than all other speeds by about 50%. On increase in moment arm, the synchronous radial error motion values are found to increase, except for 120 krpm. Both x- and y-directions follow similar trends.

Fig. 5.21 shows the 1σ values as a measure of asynchronous radial error motions. The 1σ values are calculated for motions along both the x- and y-directions. In general, the change in 1σ values is marginal on increase in moment arm. The maximum 1σ values of the asynchronous error motions

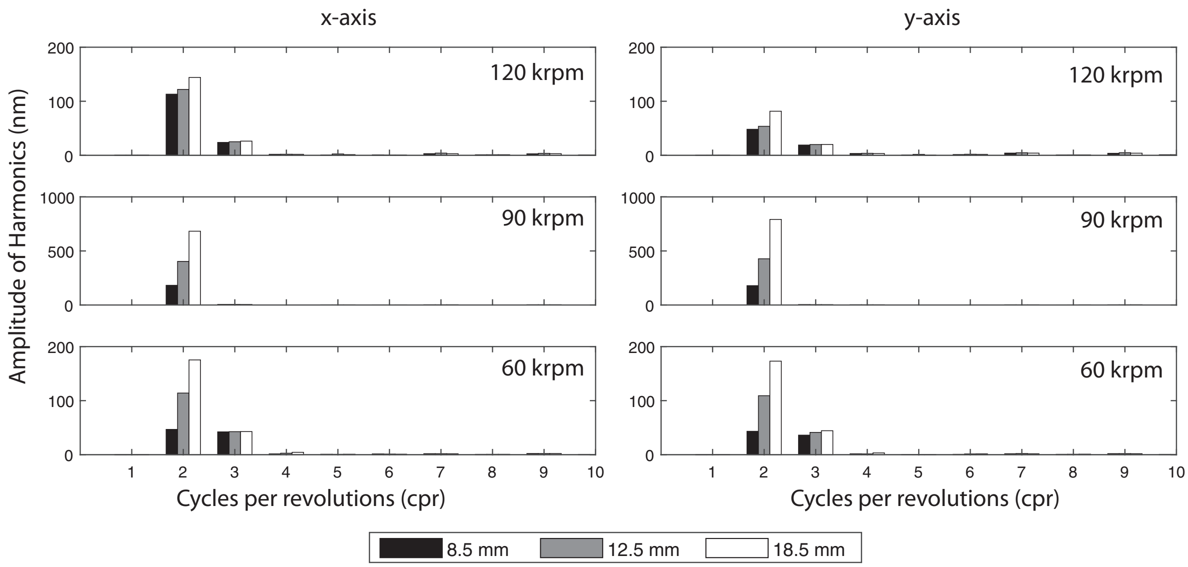

Figure 5.19: *Magnitude of the Fourier transforms of synchronous radial error motion along x- and y-directions at varying moment arm.*

for x-direction are seen at 80 krpm. As before, the amplitude of motion at 80 krpm is significantly lower along y-direction. For all other speeds, the 1σ values are below 100 nm and 150 nm for motions along x-axis and y-directions, respectively.

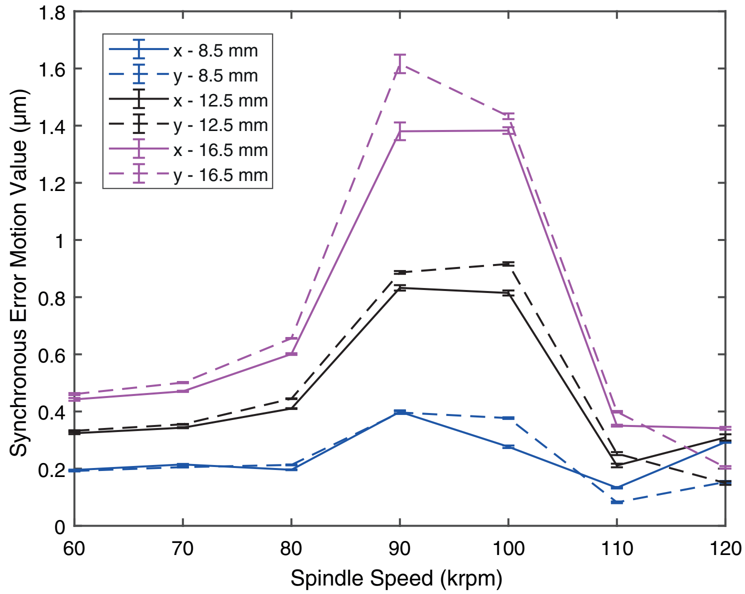

Figure 5.20: *Synchronous radial error motion values along x- and y-directions at varying moment arm.*

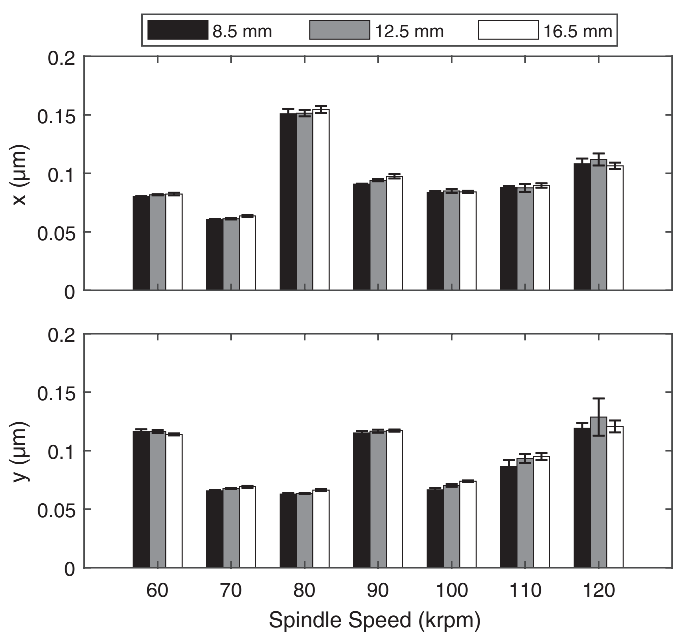

Figure 5.21: 1σ *of asynchronous radial error motion along x- and y-directions at different radial loads.*

5.6 Uncertainty Analysis

The uncertainty analysis for the spindle metrology work is conducted as per [72]. The uncertainty is considered to arise from: (1) measurement instrumentation related (LDV, DAQ), (2) environmental factors (acoustic noise, air flow, temperature fluctuation, vibration induced due to rotation of spindle), (3) laser beam alignment and curvature effects, and (4) data processing.

In general, the uncertainty can be grouped into two categories according to the way in which its numerical value is estimated: (1) Type A those which are evaluated by statistical methods, and (2) Type B those which are evaluated by other means. They are characterized by estimated variances, s_i and approximated variances u_i, respectively. Depending on the (assumed) distribution, various coverage factors k_p are used to relate the range to the standard uncertainty u_i given as

$$u_i = k_p.(range) \tag{5.15}$$

The value of k_p for normal and rectangular distributions are 0.25 (95.45% confidence) and 0.29 (100% confidence), respectively. The combined uncertainty uc can be characterized by the numerical value obtained by applying the method for the combination of variances.

5.6.1 Measurement instrument related

The uncertainty due to LDV and NI-DAQ affects all frequency components. To quantify the magnitude across the frequency spectrum, displacement measurement is conducted from the surface of a tool clamped to the spindle at rest. At rest, the measured motions are classified as noise of the measurement instrument. In addition to instrument noise, these measurements contain contributions from the environment such as ground vibrations and airflow, which is difficult to isolate. The measurements are conducted in time domain and is converted to frequency domain in Fig. 5.22. The noise is below 1 nm for frequencies above 500 Hz along both x- and y-axes. The frequencies below 500 Hz typically constitute asynchronous frequencies since we do not run spindle below 30,000 rpm (500 Hz). Therefore, the uncertainty towards fundamental and synchronous frequencies is much less than 1 nm at all spindle speeds and hence can be considered negligible.

5.6.2 Environmental effects

The environmental effects include airflow, thermal effects, vibrations of the LDV mounting structure (induced by rotating unbalance) and acoustic noise (from the rotating spindle). To evaluate the uncertainty due to environmental effects, a massive cast iron block is mounted on the isolation table. From the surface of the block, displacement measurements are conducted when the spindle

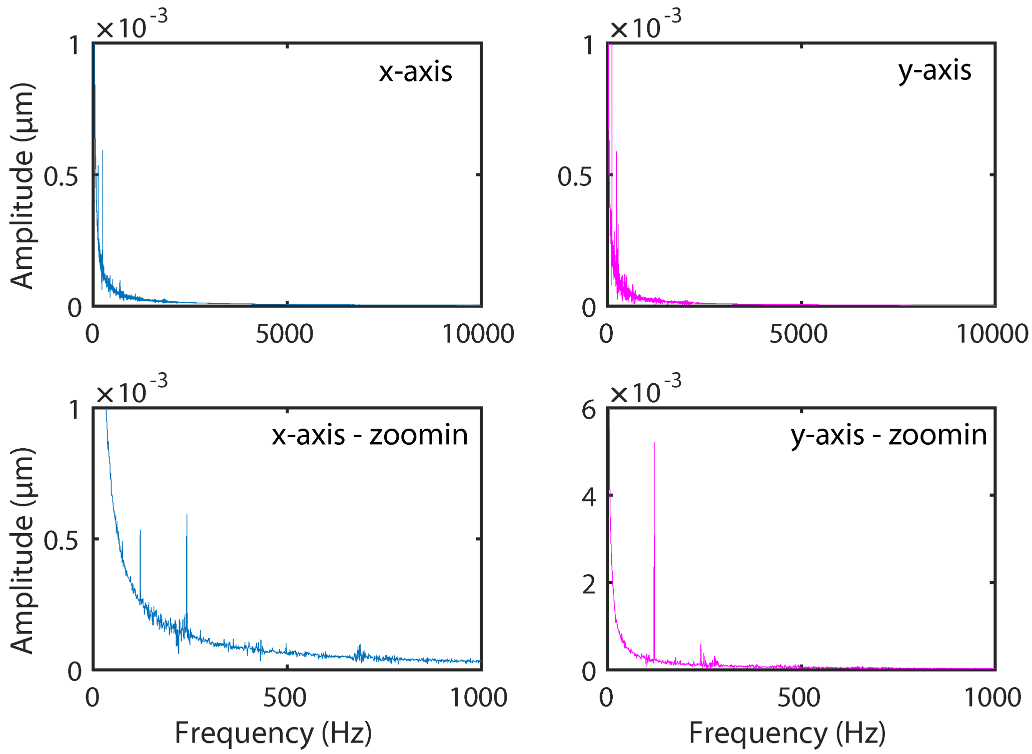

Figure 5.22: *Uncertainty due to measurement instruments.*

is running at operating speeds. The block is assumed to be completely stationary because of its massive size and hence the measured displacements correspond to the vibration of the LDV mounts due to environmental effects [26]. The measured displacements are decomposed into fundamental, synchronous and 1σ asynchronous motions and are presented in Tables 5.2-5.3. The standard uncertainty in fundamental component is found to be less than 30 nm for all speeds except for 80 krpm where it is 62 nm. The standard uncertainty in synchronous motions is found to be less than 5 nm at all spindle speeds, except 110 krpm where it is 7 nm. The standard uncertainty in asynchronous motions is found to be less than 25 nm at all spindle speeds.

Table 5.2: *Spindle speed dependent uncertainty: fundamental component.*

Spindle Speed	Range (nm)	Distribution	Standard uncertainty (nm)
60k	90	Uniform	26.1
80k	213	Uniform	61.8
100k	104	Uniform	30.1
120k	83	Uniform	24.1

Table 5.3: Spindle speed dependent uncertainty: synchronous and asynchronous components.

Spindle Speed	Range (nm)	Distribution	Standard uncertainty (nm)
Synchronous frequencies			
At 110 krpm	24	Uniform	7
Except 110 krpm	10	Uniform	2.9
Asynchronous frequencies			
All speeds	80	Uniform	23.2

5.6.3 Alignment and curvature effects

The uncertainty due to alignment and curvature effects are observable when a finite eccentricity is present in the system. Therefore, the uncertainty due to alignment and curvature is a function of eccentricity and hence cannot be generalized. The readers are encouraged to read [26, 73] where the contribution of alignment and the curvature effects towards measurement uncertainty are discussed in detail.

5.6.4 Data processing

Data processing involves separating the measured displacements into fundamental, synchronous and asynchronous components. When a sufficiently large number of revolutions (>500) are taken, the error in the calculations reduces significantly and hence can be considered negligible.

5.7 Summary and Conclusions

This chapter presented a comprehensive approach to measure radial throw under the effect of external axial and radial loading. The approach involves an implementation of multi-probe error separation technique to isolate the artifact form errors from the synchronous component of the radial throw. A well characterized non-contact loading setup is realized using permanent magnets and custom artifacts. The following specific conclusions are drawn from this chapter:

- A favorable set of probe angles were identified ($\alpha = 90 \pm 2°$and $\beta = 175 \pm 2°$) for accurate separation of artifact form errors up to 25 harmonics, considering the constraints posed by the experimental setup.

- The multi-probe method for error separation was successfully implemented on an UHS spindle. The implementation is validated by comparing the artifact form extracted at a fixed axial location for four different spindle speeds. The artifact form error was found to be similar at all spindle speeds (<30 nm variation out of $\pm$300 nm); the spindle error motions show significant variations (upto $\pm$500 nm) at different speeds, similar to that observed in [29].

- The magnet-magnet and magnet-artifact interactions are modeled in COMSOL Multiphysics. The magnet-magnet interaction model (forces) is then validated using experiments. The validated model was used to optimize both the magnet and the artifact geometry to satisfy the axial and radial loading requirements.
- The dynamic forces generated due to an average radial throw of 8 μm were found to be <1% of the applied (static) radial force at 60,000 rpm. Therefore, the dynamic forces are considered to be negligible during static radial loading.
- The theoretical stiffness of the artifact in bending is calculated to be 30 times higher than the radial stiffness of the spindle (data provided by the manufacturer), and therefore, the effect of radial loading on the bending of the artifact is considered negligible.
- On varying radial loads, the fundamental component of radial throw remains within 1% for the majority of spindle speeds, whereas the synchronous spindle error motions are found to increase by more than 200%.
- The synchronous spindle error motions depend strongly on the magnitude of force as well as the moment arm. In both the cases, an increase in 2 cpr was observed for both the x and y directions.
- In general, the 1σ of asynchronous spindle error motions were found to be affected by change in radial forces (up to 15%) and no appreciable change was observed when the moment arm is varied.

CHAPTER 6

Evaluation of Micro-tool Geometric Errors

6.1 Motivation

As discussed in Section 1, the geometric errors of the micro-tools − specifically the non-straight tool-axis, variations in the tool-diameter and the inaccurate location of the cutting edges − contribute directly to the radial throw and to the trajectory of the cutting edges at the tool-tip. These geometric errors can either add or subtract to the existing radial throw of the tool axis at the tool-tip. In this chapter, we develop procedures to quantify the geometric errors of a microtool and integrate them to the radial throw calculation at the tool-tip by extending the mathematical formulation presented in Chapter 3. Although, the procedure in this chapter is described considering a micro-endmill geometry, the approach can be applicable for other micro-tools.

6.2 Introduction

An ideal micro-endmill is presented in Figure 6.1(a). It consists of a 3.175 mm diameter shank, a fluted tool-tip and a tapered region which connects the shank to the fluted tool-tip. The geometric errors of interest to us, affecting the radial throw at the cutting edges, are are highlighted in Figs. 6.1(b)-(c). First, a non-straight tool axis is shown in Fig. 6.1(b). This non-straightness directly affects the radial throw prediction at the tool-tip. Second, the tool-diameter can deviate from its nominal diameter. And third, the inaccuracy in the location of the cutting edges is depicted in Fig. 6.1(c) with: (1) an included angle less than 180 degrees for a two-fluted micro-endmill resulting in a deviation $\Delta\theta_p$, and (2) a difference in the magnitude of effective radii (r_1, r_2 where $r_1 \neq r_2$).

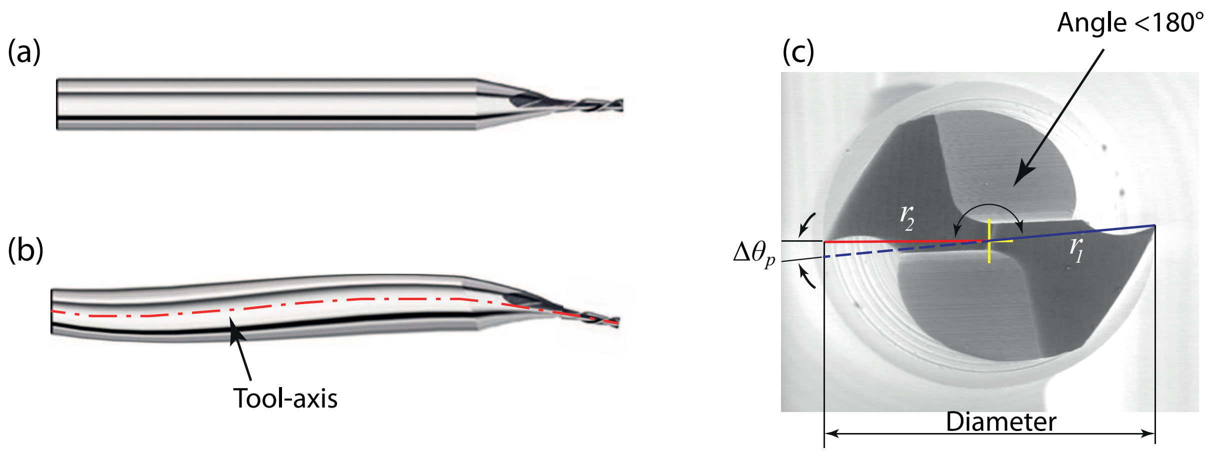

Figure 6.1: *(a) An ideal 2-fluted micro-endmill [Source: www.harveytool.com], (b) Non-straight tool-axis (significantly exaggerated), (c) imprecise tool-diameter and inaccuracy in the location of cutting edges depicted by effective radii (r_1, r_2 where $r_1 \neq r_2$) and deviation in the included angle (from 180°) between the radial vectors.*

The tool diameter appears to be the most fundamental factor affecting the accuracy. For tools with diameters below 1 mm, most commercial tool manufacturers (e.g., Performance Micro Tools and Harvey Tools) have a tolerance specification of ±0.0005" (12.7 microns). For this reason, many machine tool manufacturers offer *tool-setter* [74], an instrument capable of measuring *effective* tool-diameter when the tool is clamped to the spindle. The effective tool diameter is the diameter of the biggest circle created by the cutting edges of the tool when it is rotated ($= 2(max(r_1, r_2))$). The tool setter is capable of measuring both the static and the dynamic run-out at the tool-tip but the accuracy is limited to 2 μm and works reliably at a maximum speed of 80,000 rpm (when measuring dynamic run-out). Alternatively, there are many offline methods to measure the tool-diameter such as using Scanning Electron Microscopy (SEM), optical microscopy and focus variation based microscopy to name a few. Similarly, the inaccuracy in the placement of cutting edges can also be determined through the discussed offline measurement methods followed by appropriate post processing.

From the presented literature (in Chapter 1) and the methods discussed above, the determination of the non-straightness of the tool-axis appears most challenging due to its three-dimensional nature and micron-scale tool dimensions. To address this challenge, focus-variation microscopy seems promising in determining the complete tool profile in 3D. Therefore, an effort is made to measure the aforementioned tool-geometric errors with focus-variation-based microscopy.

6.2.1 Focus variation based microscopy

In this section, a brief overview of the focus variation based microscopy is presented. The instrument has 4 degrees of freedom: 3 translation and 1 rotational. The rotational allows the tool-to be measured along its full circumference. The instrument is equipped with objectives from 2.5X to 100X, thus, capable of providing high resolution measurements. The working of the instrument is described using a schematic presented in Fig. 6.2. Light is introduced into the optical path using a beam-splitting mirror and is focused onto the specimen using an objective. The reflected light is bundled together using optics and is gathered by the charge-couple device (CCD) image sensor). This technique relies on the shallow depth of focus (see label 8 in Fig. 6.2). For a particular specimen and a given working distance, only a small region is sharply imaged. This sharpness is determined by software based methods. The objective is then translated to scan the specimen in the vertical direction yielding one sharp image per vertical step. The software algorithm then stitches all the sharp images, thus, constructing a 3D profile of the specimen.

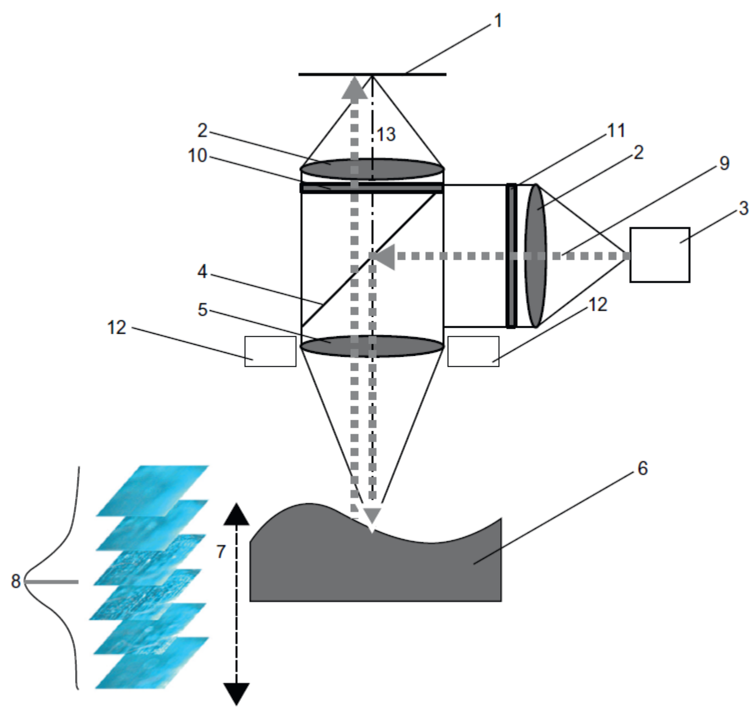

Figure 6.2: *Schematic of a focus variation instrument. 1, Sensor; 2, optical components; 3, white light; 4, beam-splitting mirror; 5, objective; 6, specimen; 7, vertical scanning; 8, focus information curve with maximum position; 9, light beam; 10, analyser; 11, polariser; 12, ring light; 13, optical axis. Source: [75]*

The scan volume of the instrument is 100 mm x 100 mm x 50 mm, which is achieved by using high precision xy stages and a software based stitching algorithm. The vertical step size depends on the chosen objective and can go as low as 10 nm. At the same time, the lateral resolution is diffraction limited and is controlled by the magnification of the objective and/or the pixel spacing of the sensor. Some of the key specification are listed in Table 6.1. The main advantage of this instrument is that the maximum measurable slope angle is not dependent on the Numerical Aperture of the objective [75]. This is made possible by employing a range of different illumination sources (e.g., ring light), which allows the measurement of slopes angles upto 85 degrees. This is one of the key enabler when measuring highly steep cutting tool profiles. In addition, the light can be polarized using filters to remove the specular light components.

Table 6.1: *Key specifications of the Alicona focus variation based microscope.*

Objectives		2.5X	5X	10X	20X	50X	100X
Working Distance (WD)	μm	8.8	23.5	17.5	19	11	4.5
Lateral sampling distance	μm	3.52	1.76	0.88	0.44	0.18	0.09
Max. lateral resolution	μm	6.92	3.49	1.75	0.88	0.64	0.44
Best vertical resolution	nm	2300	410	100	50	20	10
Minimum repeatability	nm	800	120	30	15	8	3

6.2.2 Measurement Concept

An ideal procedure to obtain the tool-axis of a micro-tool is discussed here. The non-straight tool-axis can be represented as a function, $\boldsymbol{q} = \boldsymbol{q}(x', y', z')$, dependent on all the three axes. The z'-axis aligns with the average (ideal) axis of the tool. The radial directions are represented by x' and y' axes. In an ideal case, the function $\boldsymbol{q}$ yields a straight line with $(x', y') = (0, 0)$. However, it deviates from a straight line as a result of manufacturing errors. A two-step procedure can be followed to obtain the true axis of the tool: (1) by measuring the circumference of the tool, perpendicular to the z'-axis, to obtain a 2D cross-section in the $x' - y'$ plane, and (2) finding the center of the best-fit circle (in least square sense) to the obtained cross-section [76]. This process can be repeated at each discretized axial location and the centers of each of those circles can be connected together to obtain the actual tool-axis. This method of finding the tool-axis is known as cross-section strategy [76] as depicted in Fig. 6.3(a). There are few other measurement strategies discussed in literature such as generatrix strategy, bird-cage strategy and points strategy (see Fig. 6.3).

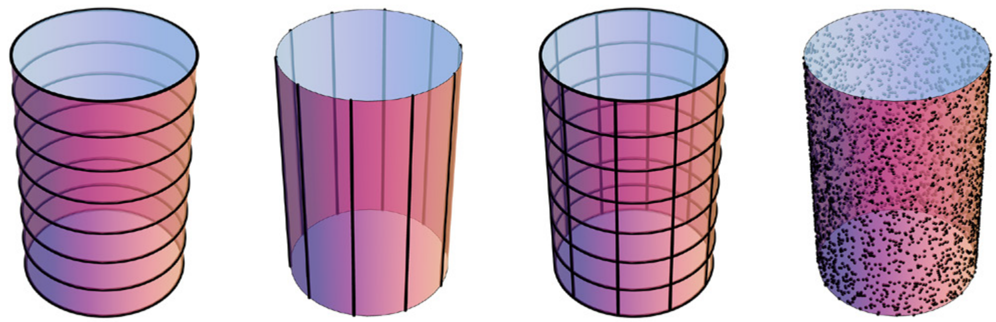

Figure 6.3: *Strategies for measurement of cylindricity [76]: (from left to right) cross-section strategy, generatrix strategy, bird-cage strategy and points strategy.*

6.3 Integrating Tool-geometric Errors with Radial Throw Formulation

The radial throw formulation presented in Eq. (3.9) assumes tool-geometric errors to be non-existent. In this section, we drop this assumption and include a tool-geometric error as a function and integrate in the formulation. In particular, the non-straight geometric axis of the tool and the inaccuracies in the position of the cutting edges, directly affects the tool tip motions (see Fig. 6.4).

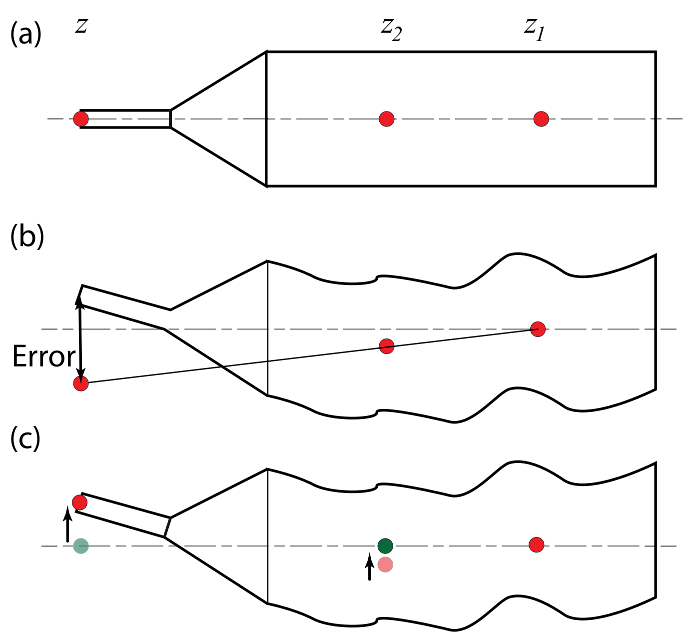

Figure 6.4: *Tool-geometric errors: (a) ideal tool, (b) error in the shank region, and (c) error in both the shank and the tool-tip.*

The non-straight tool axis is represented as a function, $\boldsymbol{q} = \boldsymbol{q}(x', y', z')$. A straight line is then fit to the curve $\boldsymbol{q}$ to represent the average (ideal) tool-axis, represented as dotted lines in Fig. 6.4. Since radial throw measurements at the tool-shank gives the displacement between the geometric-axis of the tool and the axis average line, the non-straightness of the tool is included. Therefore, to obtain the true radial throw value, the contribution from non-straightness needs to be removed. It is noted that z and z' axes show a axis offset due to tilt errors. However, for small enough tilt angle (< 0.05 degs.), the location error in the determination of non-straightness is calculated to be under 20 nm, and hence can be ignored. Therefore, for the purpose of adding/subtracting tool-geometric errors, the axis z and z' are assumed to be parallel.

A generatrix based approach is adopted to explain the measurement approach. A total of 10 different crest of the tool (along the length) can be measured by rotating the tool by 36 degrees at each step. Each measurement along the axis results in a profile of the tool along the length. The tool also possess a reference mark on its shank portion and it is also measured during one of the measurement when the reference mark is on the top (typically the first measurement since will be easier to align). Each of the profile are filtered by using an approach presented in [39]. At this point, an average of all the collected profiles can be taken to obtain a 3D curve representing the true tool-axis. A straight line is then fit to the curve to represent the average (ideal) tool-axis. The average tool-axis pass through point A'. The ideal tool-axis aligns perfectly with the z'-axis. The function $\boldsymbol{q}$ can be calculated which represent the true tool-axis in the $x'y'z'$ coordinate system. Since the first measurement is aligned with the reference mark and with from measurements, the ideal and the actual tool-axis is known - the information is sufficient for calculating the orientation angle α_i and displacement d_i for an axial location i, as depicted in Fig. 6.5.

The next set of measurements is presented with the help of Fig. 6.5. In the schematic diagram we focus on a single $x - y$ plane of measurement, where the radial throw is described by $\boldsymbol{\rho}$ and the average tool-axis is located at $\boldsymbol{\rho'}$. From the tool-measurements, the displacement relationship between $\boldsymbol{\rho}$ and $\boldsymbol{\rho'}$ (length of AA', $\boldsymbol{d}$) as well as its orientation α with respect to the reference mark (reference mark represent the average axis of the tool-shank) is known. Therefore, we find $\boldsymbol{\rho'_1}$ and $\boldsymbol{\rho'_2}$ at two of the measurement locations $i = 1, 2$. The obtained $\boldsymbol{\rho}'_1$ and $\boldsymbol{\rho}'_2$ are used to calculate $\boldsymbol{\rho}'_z$ at the tool-tip using Eq. (3.9). And lastly, $\boldsymbol{\rho}'_z$ is transformed to $\boldsymbol{\rho}_z$ using vector addition of the tool-axis error, given as

$$\boldsymbol{\rho}_z = \boldsymbol{\rho}'_z + \boldsymbol{d_z}. \tag{6.1}$$

The measurement of tool-diameter and inaccuracy of each of the cutting tools is also accomplished using the focus variation based microscopy. These results can be added in a straightforward sense

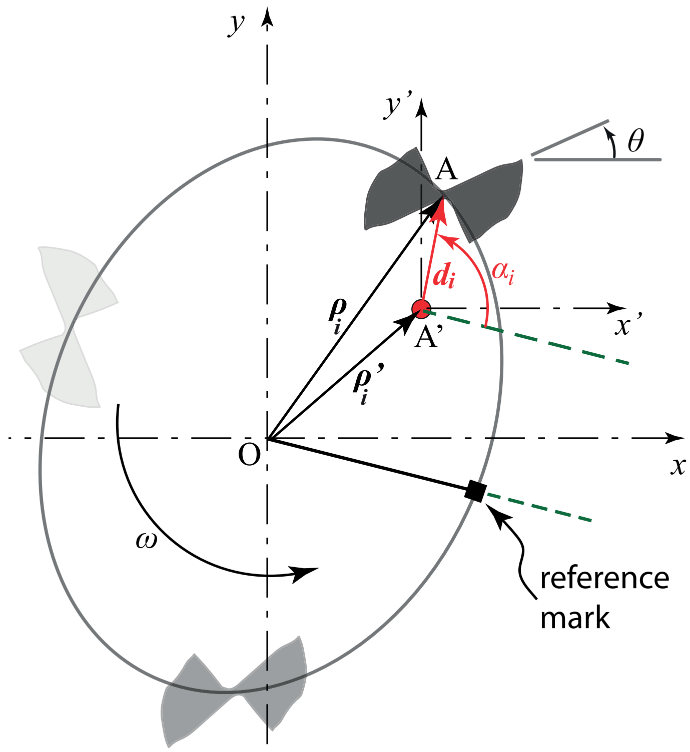

Figure 6.5: *Schematic diagram to include non-straightness of tool axis in the radial throw calculations. The physical location of tool-axis is point A, the average tool-axis lies at point B, where vector* $\boldsymbol{d}$ *represent the non-straightness of the tool-axis at an angle* α *with respect to the reference mark.*

to the $\boldsymbol{\rho}$ at the tool-tip, yielding trajectory of the m^{th} cutting edge as

$$\begin{aligned}\boldsymbol{p_m}(z,\theta) = \big(\rho_x(z,\theta) + r_m\cos(\theta + 2\pi(m-1)/n + \Delta\theta_{pm})\big)\boldsymbol{i}\\ + \big(\rho_y(z,\theta) + r_m\sin(\theta + 2\pi(m-1)/n + \Delta\theta_{pm})\big)\boldsymbol{j},\end{aligned} \quad (6.2)$$

where $\boldsymbol{i}$ and $\boldsymbol{j}$ are the unit vectors along the x and y directions, respectively. Variables ρ_x and ρ_y are the x and y components of $\boldsymbol{\rho}$, r_m is the effective radii of the m^{th} cutting edge, n is the number of cutting flutes, and $\Delta\theta_{pm}$ is the deviation of the pitch angle from its nominal value.

6.4 Measurement Approaches

6.4.1 Identification of tool-axis using 3D profile measurement (points strategy)

Using the focus variation microscopy, the 3D profile of a 1 mm diameter, two-fluted micro-endmill is measured. The tool is attached to the rotary stage (real 3D$^{\text{TM}}$ rotation stage) of the instrument (as shown in Fig. 6.6(a)). The measurement length span from the shank portion of the tool to the tool-tip. A 20X objective with lateral and vertical resolution of 2 and 0.1 microns, respectively, is selected for this measurement. The brightness and contrast is chosen to minimize the specular light components. The tool was thoroughly cleaned before taking measurements. To obtain a 3D measurement of the tool profile, the circumference is divided into twelve equal portions where each portion is measured at a time. This resulted in an overlap of 30% between two adjacent sections. The entire measurement scheme is software controlled and thus, is fully automated. The measurement took approximately 24-30 hours to complete.

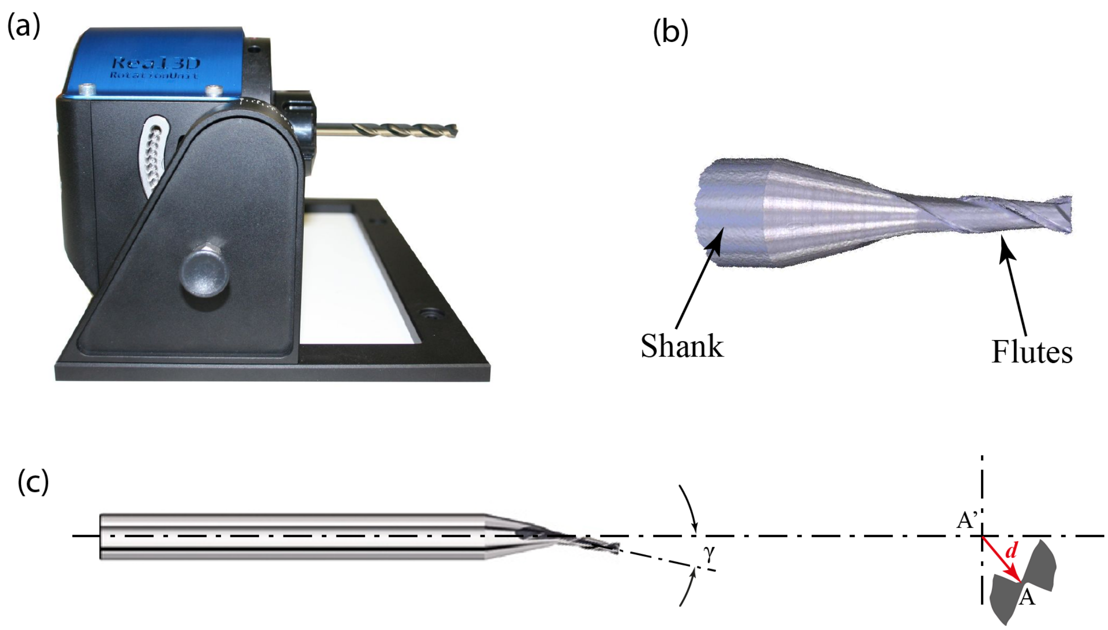

Figure 6.6: (a) Real 3D rotation stage, (b) a 3D measurement of a 2-fluted micro-endmill, and (c) misalignment angle γ between shank axis and the flute axis.

The software identifies the sharp features from the collected images and stores it as a three-dimensional point cloud. To assist in visualization, the software interpolates between three adjacent points to create a surface and also preserves the color information. The result of this measurement and post processing procedure is presented in Fig. 6.6(b). The 3D profile contains both the shank and the flutes portion. The bright and dark bands seen on the reconstructed profile is a visual artifact created as a result of overlapping adjacent portions of the circumference.

For the current analysis, it is assumed that the major error in the tool-axis originate from the axis offset between the shank portion and the fluted portion [25] (as shown in Fig. 6.6(c)). To find the axis offset, it is required to find the axis of the cylindrical shank portion and the axis of the fluted portion. For this purpose, the 3D point cloud data is exported from the machine as a text file and is imported in MATLAB for post processing.

To obtain the axis of the shank portion, a least square cylinder is fitted to the 3D point cloud data corresponding to the shank portion (see Fig. 6.7(b)). To this end, a MATLAB based code is written where the algorithm outputs two parameters: (1) the orientation of the axis of the cylinder in 3D space, and (2) the radius of the fitted cylinder.

Similarly, to obtain the axis of the fluted section, a least square cylinder is fitted to the fluted portion. Due to the presence of flutes, an additional post-processing step is required. In this step, the 3D points falling inside the 1 mm cylinder are omitted based on a threshold value, leaving behind the points lying on the circumference of the flute. To omit the points, the distance of each point from an approximate center line is determined and the points falling under 95% of the nominal radius are omitted. This cleanup procedure is important to reduce the error in the least square fitting. After the cleanup procedure, a best fit cylinder is fitted to the remaining data (see Fig. 6.7(a)). Using this procedure, the axis offset at the tool-tip (i.e., eccentricity $\boldsymbol{d}_z$) is calculated to be 17.33 μm. Based on the prior experience with the tools during micromachining , the obtained value is considered to be an overestimate.

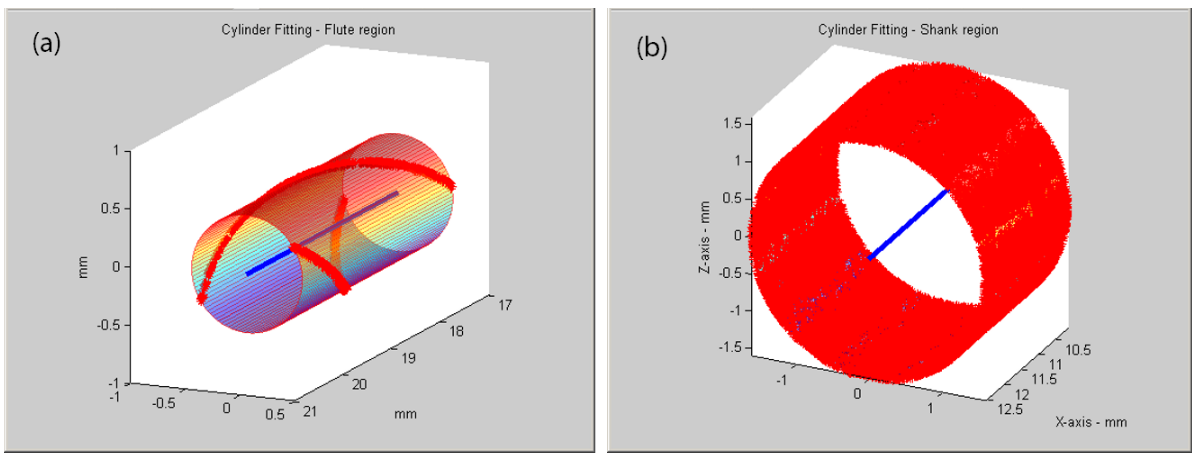

Figure 6.7: *Least-square cylinder fitting to a measured 3D point cloud of a micro-endmill: (a) fluted portion, and (b) shank portion.*

On close examination, it is noted that the distribution of 3D points on the circumference (of the flute) is uneven. For some locations, a higher number of points are segregated when compared to other locations. This is caused due to highly reflective nature of the cutting tools and/or high undercut present at the cutting edges resulting in a loss of data. This unevenness in 3D point distribution introduces error in the least square fitting as the fitting is sensitive to the overall number and the distribution of points. Unfortunately, there does not seem to be a way to uniformly sample the points during a measurement. Therefore, a different approach is needed to quantify the errors.

During this procedure, it is also realized that the tool-axis may not be reliably determined using the read-3D rotation stage of the instrument. For reliable measurement, the rotation stage should compensate for the attachment-tilt angle when the microtool is clamped to the stage. The inefficient tilt angle compensation of the real-3D rotation stage introduces location error in the 3D point cloud data. As a result, measurement error of upto 12 μm at 60 mm overhang length is reported in [77]. Therefore, appropriate compensation techniques are needed to make reliable measurements using the read-3D rotation stage.

6.4.2 Quantification of non-straightness in tool-shank through LDV-based measurements

LDV-based measurements directly provides the location of local (for a particular measurement plane) geometric-axis of the tool-shank. Therefore, the measurements conducted in Section 4 can be analyzed for the straightness of the tool-axis. The one-per-rev component of radial throw is plotted in Fig. 6.8. For the tested micro-endmill, it is observed that the deviation from the straightness is symmetric along the axis, on an average. Numerically, the non-straightness of the obtained tool-axis is with in ±100 nm. For such small deviation from straightness, the axis of the tool-shank is assumed to be straight. Therefore, the tool-shank can be used as a reference to find the axis-offset $\boldsymbol{d}_z$ at the tip of the tool.

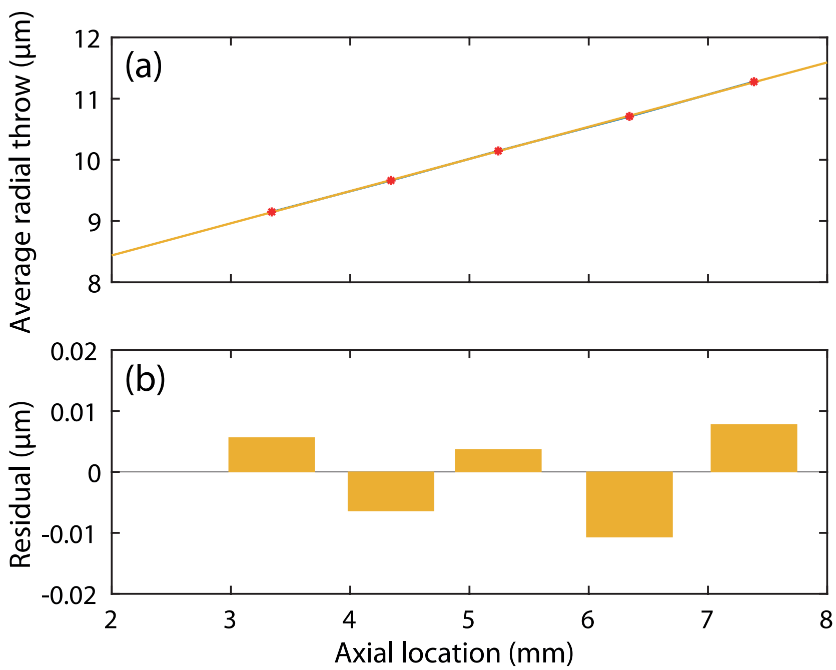

Figure 6.8: *(a) Average radial throw (dots) is presented as a function of axial location and a line is fit to the data representing average location of tool-axis, and (b) residual between the fitted line and the actual data.*

6.4.3 Use of precision pins to identify the axis-offset at the tool-tip

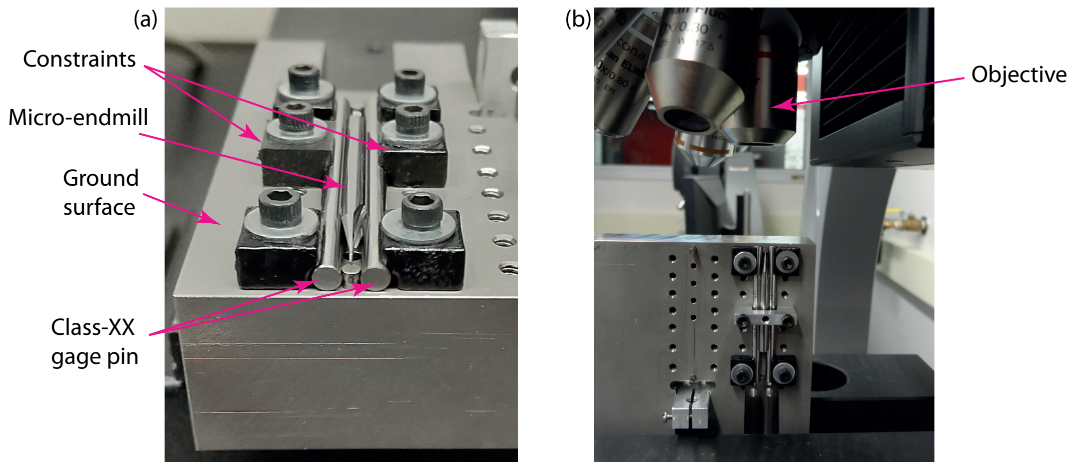

Figure 6.9: *Precision setup to measure tool-geometric errors (a) micro-endmill placed on two Class-XX gage-pins, and (b) setup placed under Alicona microscope for measurement.*

Considering the results from the previous section, the axis of tool-shank can be asumed to be straight. Thus, it can provide a reference for the following measurements. Now, to obtain the axis-offset the at tool-tip, a custom v-block is designed using two class-XX gage-pins (3.175 mm diameter). These two pins are arranged side-by-side to provide an axis of rotation (see Fig. 6.9). A direct line contact between the gage-pins is avoided by using two pillars (class-XX gage-pins) of 2 mm diameter each. This arrangement allows for point contact and improves the accuracy of the system. The 3.175 mm gage-pins are held in place by using three constraints each. The weight of the micro-tool is sustained by a small wedge glued to the base plate (providing axial constraint) and a set screw is used to constraint the tool radially. The circularity of gage-pin is specified to be 508 nm. The tool-shank is assumed to be straight for these measurements, so are the axes of the gage-pins. Under these assumptions, the cylindricity of all three tools (two gage-pins and a micro-tool) under test is exceptionally high and hence it contributes to a <1 μm loss in rotation accuracy.

To obtain the axis offset ($\boldsymbol{d}_z$) between the shank portion (assumed straight) and the tip of the tool, two separate measurements are required. Between the two measurements, the tool is rotated by an angle Ω. The rotation center $A'(x_0, y_0)$ is coincident with the average axis of the shank. The two measurements (x_1, y_1) and (x_2, y_2) are used to identify the location of the cutting edge in the 2D space. To obtain the rotation center A', two equations corresponding to the rotation of axes are solved simultaneously. Mathematically, the equation is represented as

$$\begin{bmatrix} x_2 - x_0 \\ y_2 - y_0 \end{bmatrix} = \begin{bmatrix} cos\Omega & -sin\Omega \\ sin\Omega & cos\Omega \end{bmatrix} \begin{bmatrix} x_1 - x_0 \\ y_1 - y_0 \end{bmatrix} \tag{6.3}$$

and the axis-offset $\boldsymbol{d}_z$ at the tool-tip can be calculated as the distance between the rotation center A' and the geometric center of the tool A.

To conduct measurements, first, the cross-section at the tip of the tool is scanned using Alicona microscope to generate a 3D profile. Without disturbing the setup, a partial profile of the one end of the gage-pin is also scanned, which serves as a reference. Second, the tool is rotated by an unknown angle Ω. This angle is later determined during post processing. Third, after rotation, the cross-section of the tool is measured again as well as the partial profile of one end of the gage-pin without disturbing the setup.

The post-processing involves running a correlation algorithm (provided by Alicona microscope) to match the partial profile of the gage pin which brings both the measurements in a single co-ordinate system. The geometric center and the cutting edge of the tool is then determined for both the measurements. These values are plugged into Eq. (6.3) to obtain the rotation center A' and subsequently, $\boldsymbol{d}_z$. To validate, additional measurements are made by rotating the microtool and comparing the measurements with one another. This serves as a cross-validation and with sufficient number measurement for a particular tool, variance associated with the measurement can be quantified.

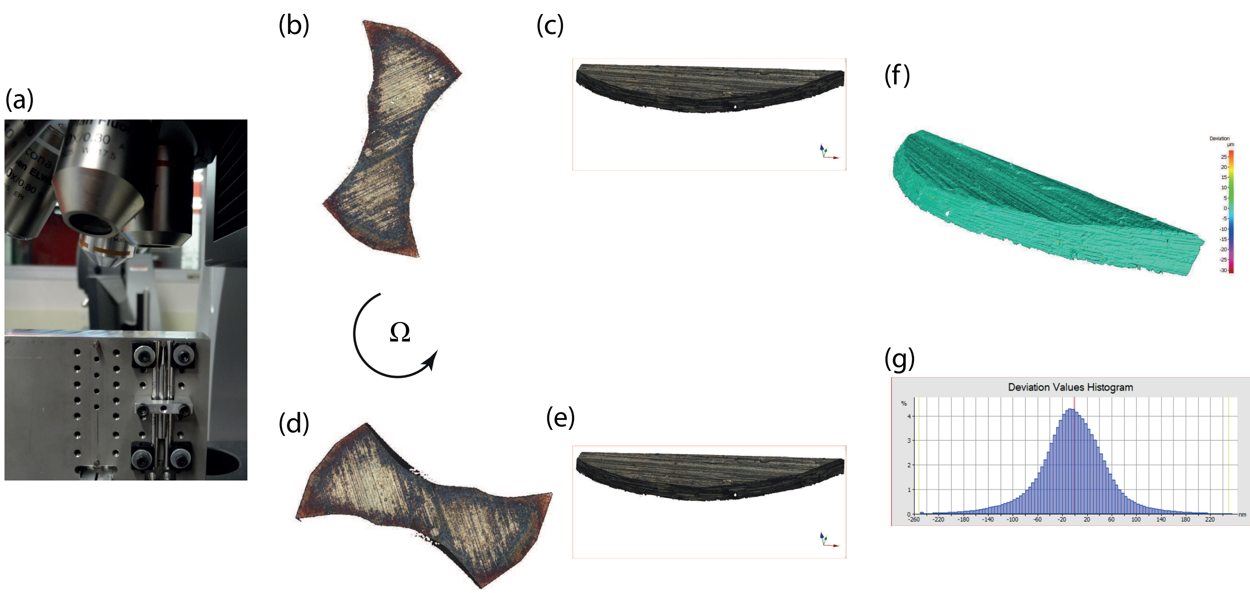

Figure 6.10: *Measurement procedure (a) precision v-block under the microscope, (b)-(c) measurement # 1, (d)-(e) measurement # 2 after Ω rotation, (f)-(g) deviation after matching the portion of the gage-pin.*

6.5 Summary

This chapter introduced the tool-geometric errors affecting the trajectory of the cutting edge at the tool-tip: (1) non-straight tool axis, (2) variation in the tool diameter, and (3) inaccuracy in the location of the cutting edges. To measure the non-straight axis of the shank and the axis offset between the shank portion and the fluted portion, focus variation based optical microscopy (FVM) technique is deemed promising.

In this regard, the FVM was used to measure a 1 mm diameter, two fluted micro-endmill. The generated 3D point cloud data was post processed in MATLAB to extract the axis of the shank and the axis of the flute. The results were considered to be over estimating the axis offset and the key reason was identified as the non-uniform sampling of the measured points. This occurs due to specular cutting edges and the presence of undercuts in the flute geometry. Further, the in-built tilt correction associated with the rotation stage of the equipment was found to be unreliable; upto 12 μm location error at 60 mm overhang length [77] are observed.

As an alternative method, axis offset at the tool-tip was determined by using two parallel class-XX gage-pins which provided a reference axis of rotation for measurements (accuracy better than 1 μm). The method was found to be promising but a formal validation and uncertainty analysis is yet to be completed.

CHAPTER 7

Effects of Radial Throw on Surface Location Error, Surface Roughness and Uncut Chip Thickness

7.1 Motivation

Radial throw critically impacts the precision attainable from a milling process [9, 78]. The changes in the tool-tip trajectory arising from radial throw induces direct (kinematic) changes in dimensional errors (surface location error, SLE) and sidewall (peripheral) surface roughness. In addition, radial throw alters the chip thickness experienced by each cutting edge, thereby causing changes in both machining kinematics and dynamics, and inducing an indirect change to the quality parameters. Therefore, it is essential to assess the effects of radial throw parameters on quality metrics of the machining process. To this end, a time-domain (kinematic) simulation of the micromilling process is conducted to determine the SLE, peripheral (sidewall) surface roughness and the variations in the uncut chip thickness induced by varying radial throw.

7.2 Model Development

7.2.1 Radial throw in micromachining

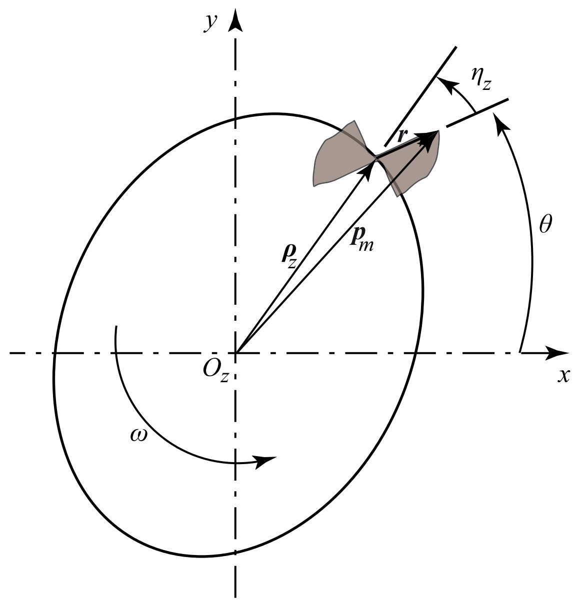

Figure 7.1: *Description of radial throw. Note that the micro-endmill is shown at a much smaller scale to help the visualization.*

To review, Figure 7.1 depicts the radial throw $\boldsymbol{\rho}_z(\theta)$ in a plane perpendicular to the tool-axis. In the absence of radial throw, this diagram would have shown a single point (the rotation axis) located at O_z. The radial throw changes the effective radii of the cutting edges. Consequently, the trajectory of the cutting edges, $\boldsymbol{p}_m$, at a given axial location z, can be written as:

$$\boldsymbol{p_m}(z,\theta) = \big(\rho_x(z,\theta) + r\cos(\theta + 2\pi(m-1)/n)\big)\boldsymbol{i} + \big(\rho_y(z,\theta) + r\sin(\theta + 2\pi(m-1)/n)\big)\boldsymbol{j}, \quad (7.1)$$

where, i and j are the unit vectors along the x and y directions, respectively. Here ρ_x and ρ_y are the x and y components of the radial throw $\boldsymbol{\rho}$, r is the radius of the cutting tool, θ is the rotation angle, and n is the number of cutting flutes. The x and y axes are mutually perpendicular axes in a plane perpendicular to the rotational axis. The orientation of radial throw is defined by $\eta_z(\theta)$, referenced with respect to the first cutting edge of the tool.

7.2.2 Modeling and assumptions

The trochoidal trajectory of the cutting edges is generated using Eq. 7.1 for a given cutting plane (axial slice of the tool). This equation considers only the kinematics of the cutting process where the additional static or dynamic effects arising from the process mechanics or dynamics (including elastic recovery, minimum chip thickness, etc.) are not studied. A full-immersion slot milling operation is simulated in this work. The points participating in the creation of sidewalls (periphery at each tool slice) are used to calculate channel width and sidewall surface roughness, as illustrated in Fig. 7.2. A mean channel width is used to represent the dimensions of the channel and a difference between the mean channel width and the prescribed width is termed as dimensional error. SLE is defined as half the dimensional error. The average surface roughness (Ra) for a single slice is calculated around the mean line (of the side profile) for both the up-milling and down-milling cases. And for finite depth of cut, areal surface roughness parameter (Sa) is calculated. To obtain the uncut chip thickness, an approach similar to that described in [17] is adopted. In this approach, uncut chip thickness is continuously monitored as a function of the rotation angle for both the cutting edges.

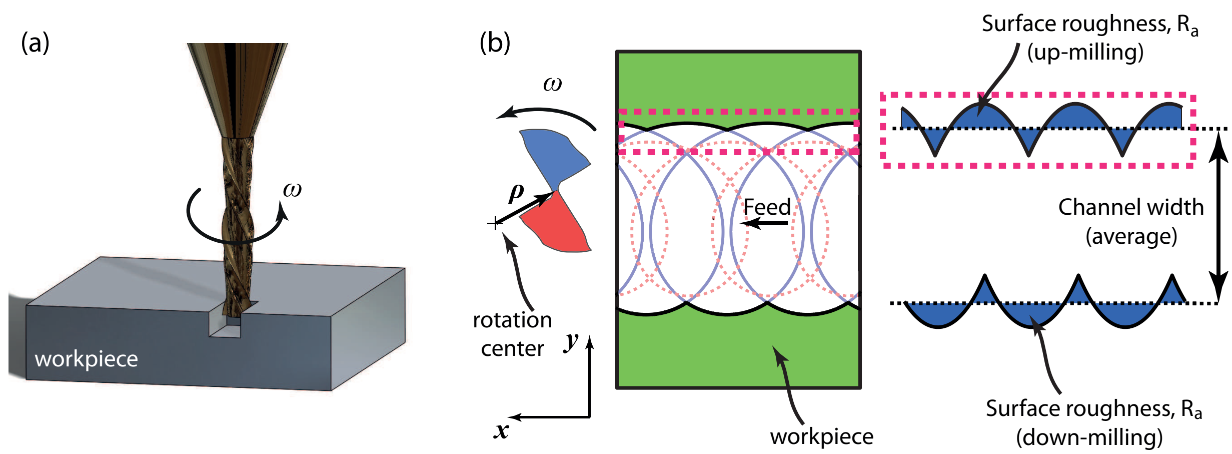

Figure 7.2: *(a) A micro-milling process depicting a full-immersion slot cutting using a 2-fluted micro-endmill, and (b) associated parameters of the machined slot such as average channel width and sidewall surface roughness.*

7.2.3 Experimental matrix

The experimental matrix (see Table 7.1) is designed to capture the contrast between the circular and elliptical radial throw trajectories as well as to study the effects of varying radial throw magnitude and orientation. A two-fluted micro-endmill with three different tool diameters (X1) with 30 deg. helix angle is considered for the simulations. The feed rate (X2) is varied in three levels at 0.1, 5 and 25 μm/flute. The trajectory of radial throw is varied for three different ellipse ratios (X3) at 1, 1.25 and 1.5. The magnitude of radial throw (X4) is varied between 0-15 μm for the circular form. And for the elliptical forms, since the magnitude is a function of the rotation angle, the length of the semi-minor axis (aligned along the x-axis) is fixed at 10 μm and the length of the semi-major axis (aligned along the y-axis) is fixed at 15 μm. This results in a fixed orientation of an ellipse. After fixing the orientation of ellipse, the feed direction (X6) is varied between 0-180 degs. to capture the effects of the elliptical trajectory. It should be noted that varying the orientation of the ellipse is equivalent to varying the feed direction. The feed direction is measured clockwise from the x-axis (see Fig. 7.2), where x, y and z denotes the machine coordinates, referenced at the spindle nose. For both the circular and the elliptical forms, a four-fold symmetry exist in radial throw orientation for a two-fluted cutting tool and therefore, radial throw orientation (X5) is only varied between 0-90 degs. The orientation of radial throw also varies within a revolution for an elliptical trajectory as the radial throw vector rotates at an angular speed, different from the rotational speed of the cutting tool. The variation of up to 11.6 degs. in the radial throw orientation is calculated for X3 = 1.5.

Table 7.1: *Experimental matrix for the time domain simulations.*

Parameter	Factor	Level		
		-1	0	1
Tool diameter (μm)	X1	50.8	254	508
Feed rate (μm/flute)	X2	0.1	5	25
Ellipse ratio	X3	1	1.25	1.5
Radial throw magnitude (μm)	X4		0-15	
Radial throw orientation (degs.)	X5		0-90	
Feed direction (degs.)	X6		0-180	
Depth of cut (μm)	X7		50	

Since the radial throw magnitude and orientation change with the axial location of the tool and the rotation angle (see Fig. 7.3), various z-slices needs to be considered. For this purpose, a 50 μm depth of cut (X7) is simulated considering six axial slices, 10 μm apart. The radial throw orientation within each slice is considered to be constant; however, its variation from slice to slice is taken into account. For a 50.8, 254 and 508 μm tool and 50 μm depth of cut, the total change in radial throw orientation ($\theta_{zi} - \theta_{zj}$) is calculated to be 32.5, 6.5 and 3.25 degs, respectively.

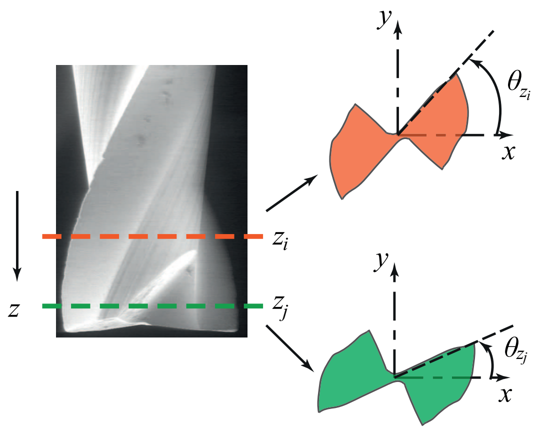

Figure 7.3: *Change in radial throw orientation with z height.*

7.3 Results and Discussion

7.3.1 Explanation of 3D simulation for a sample case

Fig. 7.4 presents the results for one of the simulation cases in 3D, considering an extended depth-of-cut of 1.38 mm. This plot helps in understanding the processing steps and the results that follows. This simulation is conducted for a 254 μm, two-fluted cutting tool. The orientation of radial throw changes linearly with the depth of cut due to a finite helix angle. For instance, the y-axis in Fig. 7.4(b)-(c) shows a variation in orientation from 0 to 90 degs., which corresponds to a depth of cut from 0 to 1.38 mm for a 254 μm too diamter. For a particular radial throw orientation (fixed y-axis), the profile shows the variation in the side surface created for the up-milling and down-milling cases ($x - z$ plane). The radial throw magnitude was kept at 10 μm with a circular trajectory. The nominal (or prescribed) half-width is 127 μm. The effect of radial throw orientation can be observed clearly as the orientation increases from 0 to 90 degs., the half-width inches close to the nominal value. The simulation also presents the expectation from the micromachining process. If the depth of cut is chosen to be 1.38 mm, some portions of axial depths show high accuracy (close to nominal half-width) and other portions show an error of upto 12 %.

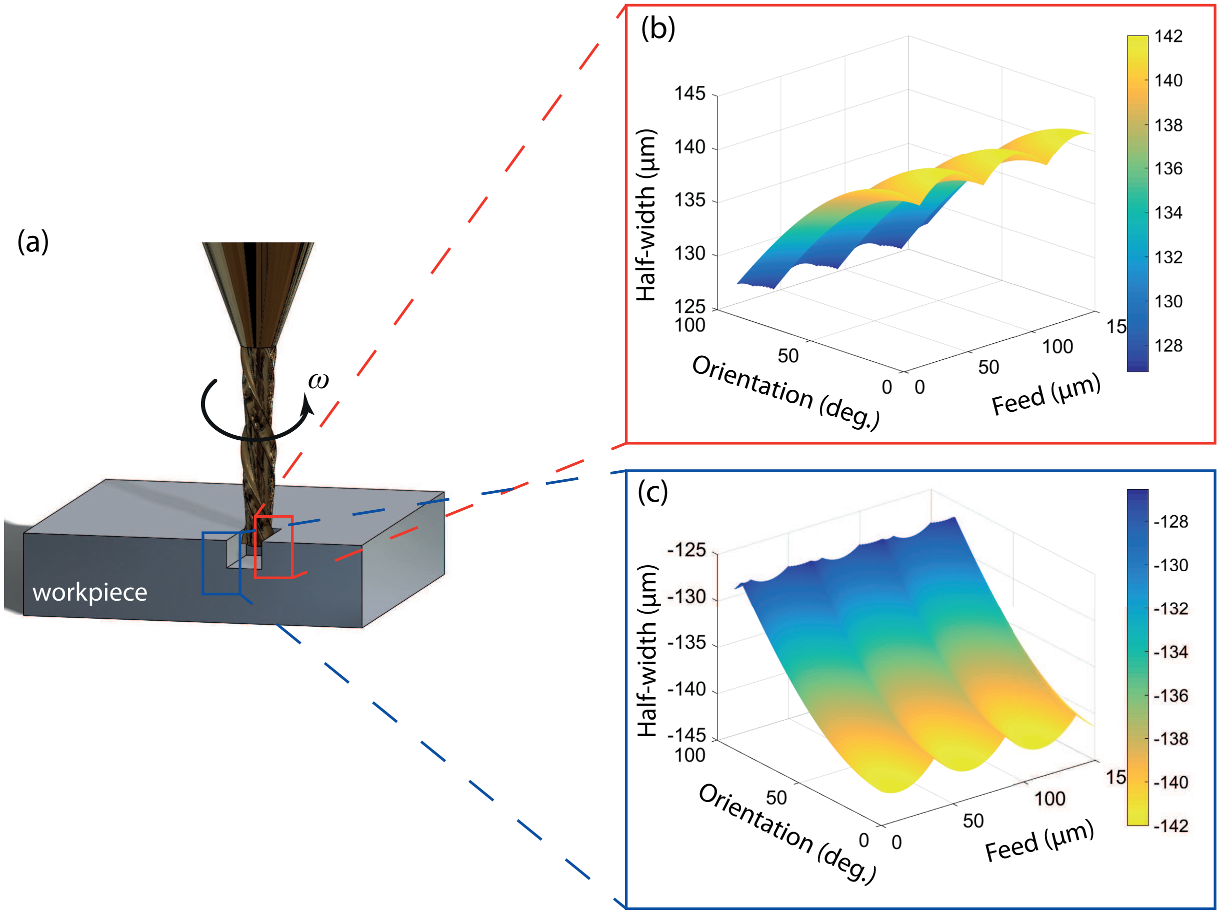

Figure 7.4: *A 3-d profile of the channel for a 254 μm tool: (a) up-milling, and (b) down-milling.*

Fig. 7.5 presents a sample contour plot depicting dimensional errors as a function of radial throw amplitude and orienation. In the absence of tool-tilt (assumed), a finite depth of cut introduces an averaging effect to the dimensional errors. In other words, instead of a dot in the contour plots, there is a finite width along the orientation axis ($\Delta\eta$). When the tool-tilt is included, it result in a finite height along the amplitude axis ($\Delta\rho$). The cumulative effect of both results in a curve with a slope between 0 — 90 degs. as depicted in the Fig. 7.5. The individual points on this curve are obtained at different axial slices which are averaged to provide a net effect.

In case of surface roughness, the effect of finite depth-of-cut is difficult to predict as the relationship between surface roughness and the peripheral points used in the calculation of surface roughness is non-linear. Where the metric Ra is defined for a line, an areal metric Sa is used for a surface. The first step in calculating surface roughness is to find the arithmetic mean of the line or of a surface. Since arithmetic mean of any two individual line profiles is not necessarily same, therefore, arithmetic mean of the surface created by those two line profiles will be different than individual means. This renders the Sa to be calculated for each case separately and unlike dimensional errors, an averaging analogy cannot be used.

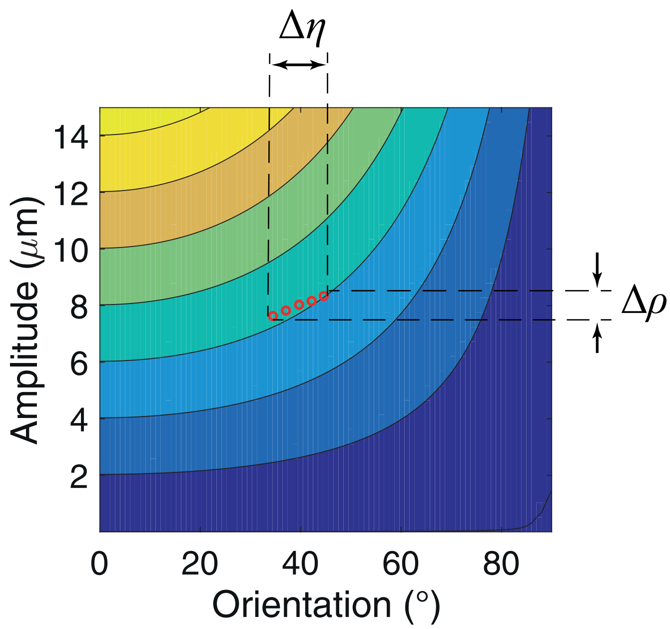

Figure 7.5: *A sample contour plot depicting dimensional errors as a function of radial throw magnitude and orientation. The unit is μm.*

For the following sections, for simplicity in understanding the effects of various parameters on various quality metrics, only a single axial slice is considered.

7.3.2 Surface location error (SLE)

Dimensional errors (or SLE) is independent of the feed rate. Therefore, the effects of ellipse ratio and tool diameter as a function of radial throw magnitude, orientation and feed direction is investigated. Fig. 7.6(a) presents contour plots as a function of magnitude and orientation of radial throw for a circular form (X3 = 1) for 50.8 μm tool diameter. As expected, the SLE increases with an increase in radial throw magnitude and a steep change is observed when the orientation is closer to 0 deg. This is expected since orientations of 0 deg. or 180 deg. dictate the radial throw to align with one of the cutting-edges, thus directly increasing to the effective tool radius by the radial throw magnitude. For the 90 deg. orientation, however, the radial throw is perpendicular to the cutting-edge radii, resulting in an effective radii very close to the actual tool radius. Fig. 7.6(b)-(c) gives radial throw orientation vs feed direction for elliptical forms. Again, at the lower end of the orientation spectrum (far from 90 deg.), effects of the elliptical form are pronounced. Specifically, the SLE varies as much as 6 μm (or 50%) as the feed direction is varied from 0 deg. to 180 deg. These results indicate the importance of considering the magnitude, orientation and the form of radial throw to understand its effect on the process output.

Figs. 7.6(d)-(i) plots the dimensional errors for 254 and 508 μm tool diameters and varying elliptical ratios. As the tool diameter increases, the effects become less pronounced, which is true irrespective of the form. This is because the contribution of tool diameter to effective radii increases with the increase in diameters which reduces the dimensional errors.

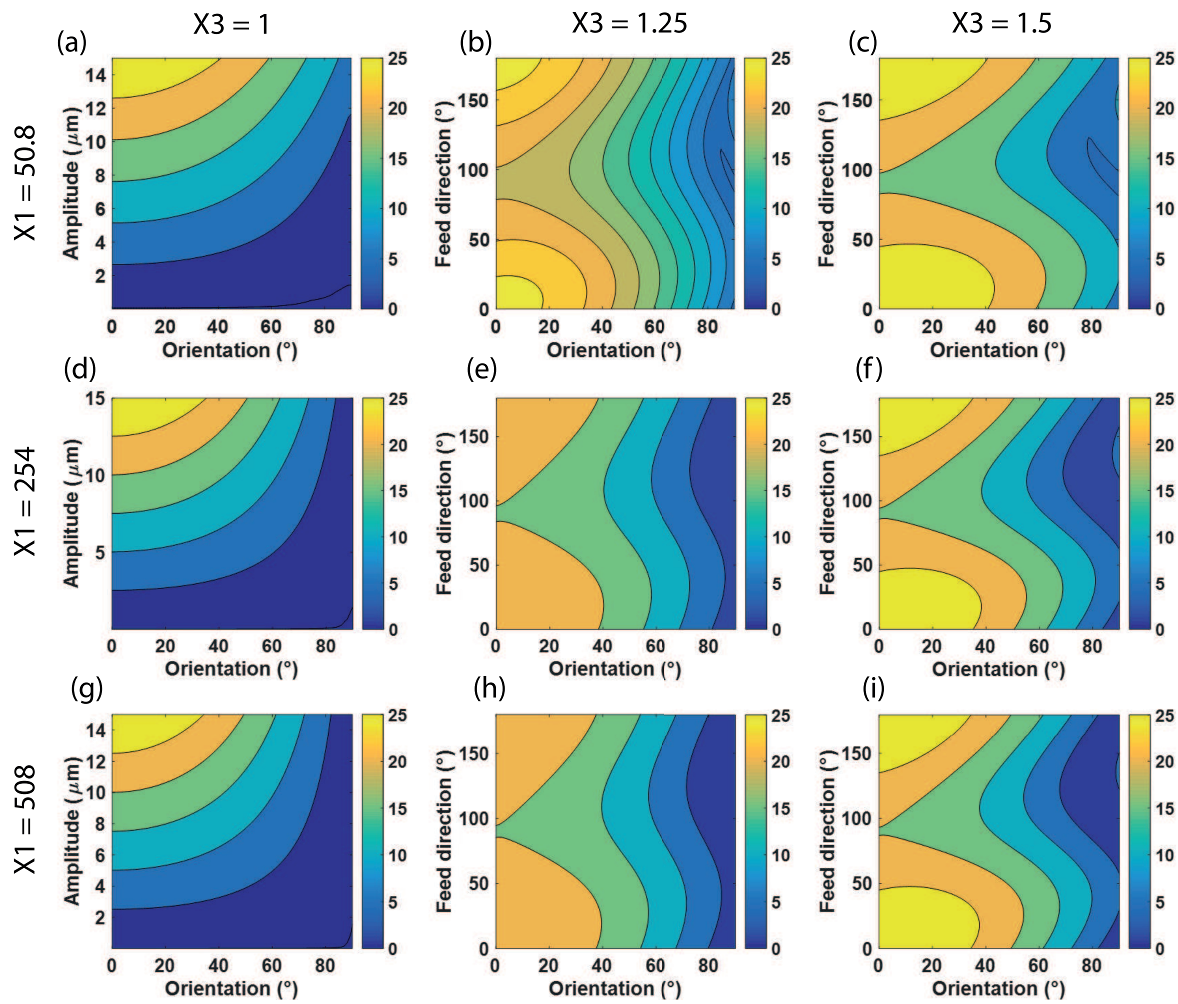

__Figure 7.6:__ Variation in the dimensional error (or twice the SLE) for (a) varying magnitude and orientation for a circular trajectory, and (b)-(c) varying radial throw orientation and feed direction for an elliptical ratio of 1.25 and 1.5, respectively. The rows present data for different tool diameters. The unit is μm.

7.3.3 Sidewall (peripheral) surface roughness

Surface roughness highly depends on the feed rate used for the micromachining process. Fig 7.7 presents down-milling surface roughness with varying ellipse ratio and feed rates along horizontal and vertical axes, respectively. We focus our attention to Figs. 7.7(g)-(i) where the feed is kept constant at 25 μm/flute and the form of radial throw is varied. In Fig. 7.7(g), the surface roughness marginally decreases for an increase in the radial throw magnitude and for a decrease in the orientation of the radial throw. This is because the surface roughness decreases as the effective radii increases due to marginal decrease in cusp heights. This effect is closely related to feed rate where a higher feed rates shows higher changes in surface roughness. For very small magnitudes of radial throw (< 0.5 m) or orientations close to 90 degs., where both edges participate in generating the sidewalls, the surface roughness is lower in magnitude.

For an elliptical form (ellipse ratio = 1.5) in Fig. 7.7(i), the notion of effective radii fails to explain the peripheral surface roughness as the trajectories are complicated, compared to a circular form. For example, at 0 deg. orientation, the effective radii at 0 deg. feed direction is higher than at 90 deg. feed direction, however, the surface roughness shows the opposite trend. Thus, the contour plots play an important role in highlighting the roughness map at various combination of parameter. From Fig. 7.7(i), it can be observed that, for a fixed magnitude, the effect of orientation and/or feed direction is found to vary surface roughness by up to 20%.

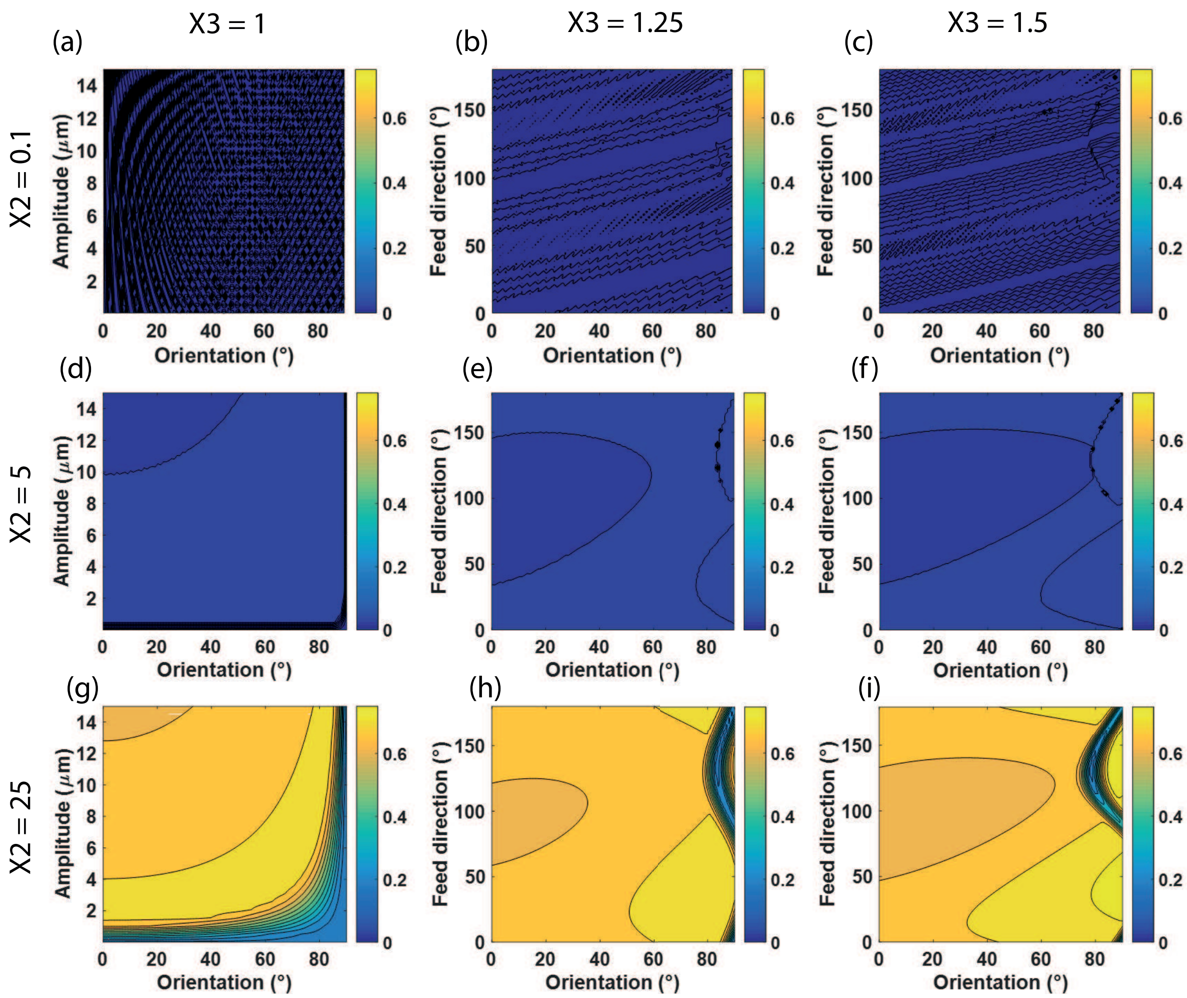

__Figure 7.7:__ The variation in the down-milling peripheral surface roughness for (a) varying magnitude and orientation for a circular trajectory, and (b)-(c) varying radial throw orientation and feed direction for an elliptical ratio of 1.25 and 1.5, respectively. The rows present data for different feed rates. The tool diameter is kept fixed at 254 μm. The unit is μm.

The diameter of the tool significantly affects the surface roughness due to change in effective radii. The higher the effective radii, the smaller the surface roughness. These effects are depicted in Fig 7.8 where a change in diameter from 254 to 508 μm brings over 50% improvement in surface finish for most radial throw magnitudes and orientations. These simulations are conducted at a fixed feed rate of 25 μm/flute.

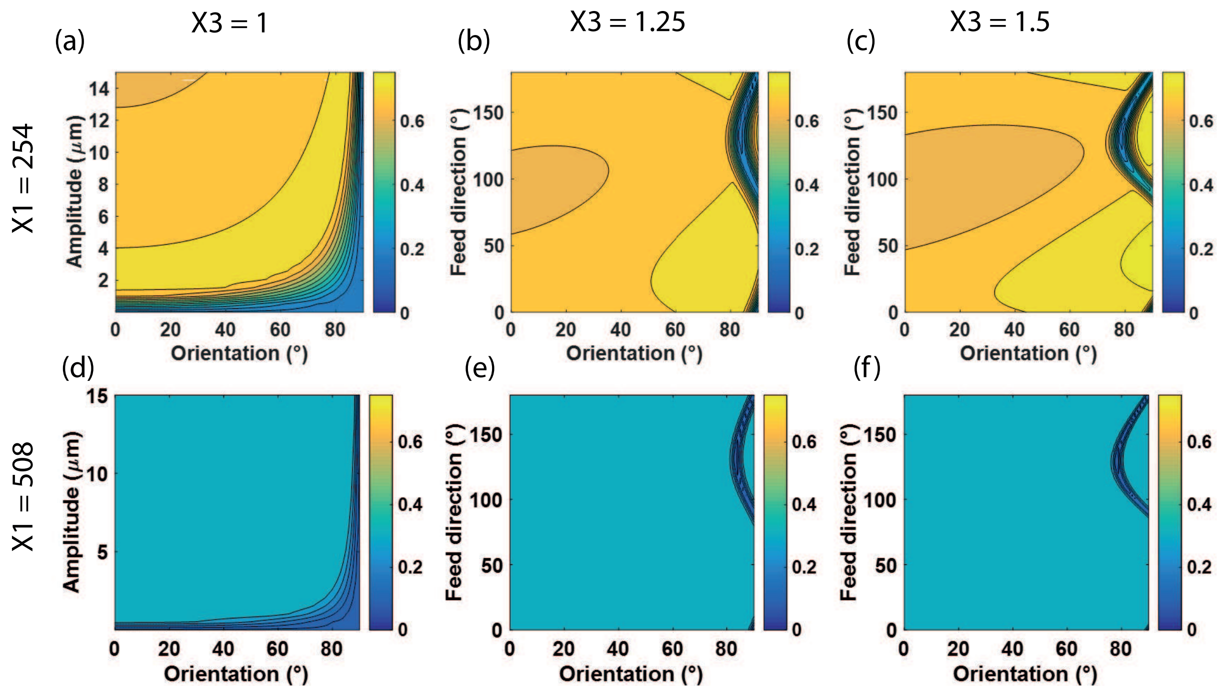

Figure 7.8: *The variation in the down-milling peripheral surface roughness for (a) varying magnitude and orientation for a circular trajectory, and (b)-(c) varying radial throw orientation and feed direction for an elliptical ratio of 1.25 and 1.5, respectively. The rows present data for different tool diameters. Feed rate is kept at 25 μm/flute. The unit is μm.*

7.3.4 Uncut chip thickness

The cutting forces observed during micromilling are a direct function of uncut chip thickness, which also affects the cutting mode, stability, and tool wear etc. Fig. 7.9 explores the uncut chip thickness as it is experienced by the cutting edges # 1 and # 2 at different radial throw orientations for the circular form of radial throw. For this simulation, the magnitude of radial throw is kept fixed at 2.5 μm (half the feed rate). The uncut chip thickness profiles are found to be significantly affected by change in the orientation of radial throw. Specifically, as the orientation deviates from 90 degs., one of the cutting points increasingly experiences a higher chip thickness than the other. When the orientation is sufficiently close to 0 deg. or 180 deg., only one cutting edge participates in cutting. As a result, the cutting forces also follow the same trends. This uneven chip loads would also cause one of the cutting edge to wear faster than the other one resulting in premature tool wear.

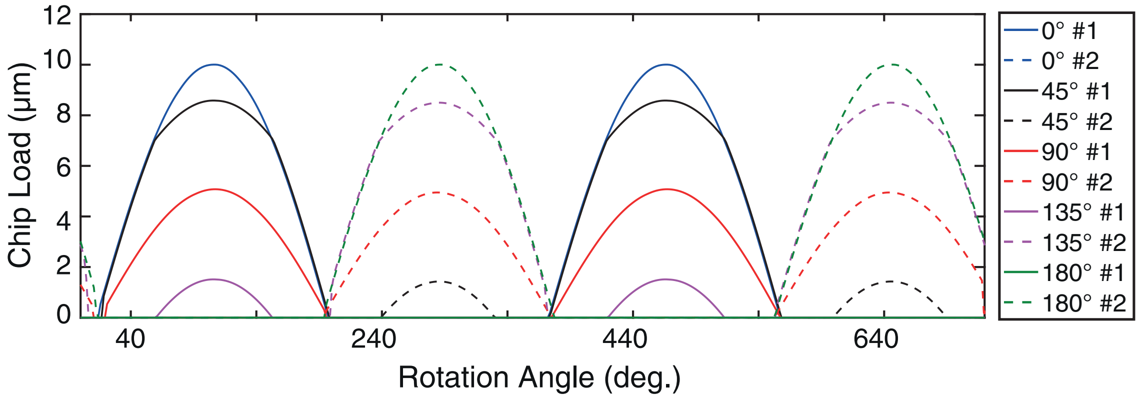

Figure 7.9: *Uncut chip thickness (or chip load) variation for a circular radial throw trajectory at a fixed magnitude of 2.5 μm and varying orientation. The cutting edges* 1 *and* 2 *are represented by solid and dotted lines, respectively.*

Figs. 7.10(a)-(b) present uncut chip thickness for an elliptical form of radial throw at 0 deg. and 90 deg. orientation, respectively. Each sub-plot features uncut chip thickness profiles for different feed directions ranging from 0-180 degs. for cutting edges # 1 and # 2. Depending on the feed direction, a variation of up to 50% in the maximum chip thickness is observed (e.g., 4 μm/flute at 45 deg. vs 6 μm/flute at 135 deg.) for one of the cutting edges. These variations can cause significant changes in the cutting force profiles. For instance, while machining a circular feature where feed direction changes continuously as the feature is being machined, the forces may contain many harmonics of the tooth passing frequency because of the variations observed in the uncut chip thickness (see Fig. 7.10(b)). Therefore, it is critical to understand the effects of both the magnitude and orientation of radial throw as well as the effects of feed direction in the case of elliptical form.

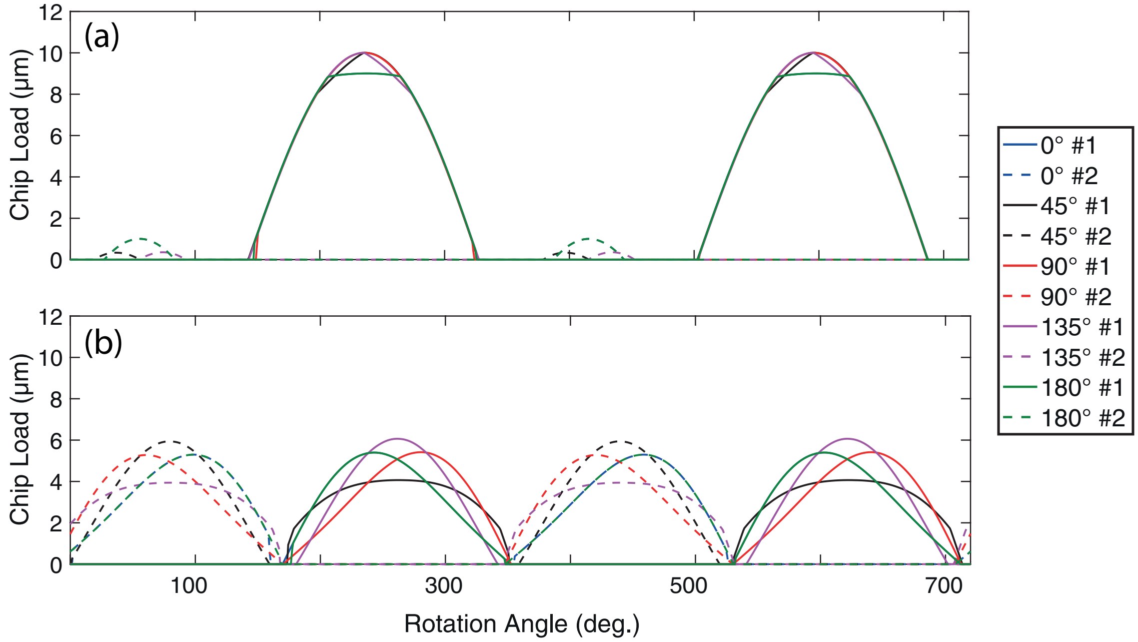

Figure 7.10: *Uncut chip thickness (or chip load) variation for an elliptical trajectory fixed at a semi-major and a semi-minor axis of 3 µm and 2 µm, respectively. The feed direction is varied for radial throw orientations of (a) 0 deg., and (b) 90 degs. The cutting edges # 1 and # 2 are represented by solid and dotted lines, respectively.*

7.3.5 Tooth-spacing angle

Tooth spacing (or pitch angle) in an ideal two-fluted tool is 180 degs. If the orientation of radial throw is 0 deg., the spacing angle remains at 180 deg. However, if the orientation is different than 0 deg., the spacing angle starts to deviate, and the deviation becomes maximum when the orientation is 90 deg. This deviation in spacing angle $\Delta\theta_p$ (see Fig. 6.4(c) for visual description) can be calculated as

$$\Delta\theta_p = 2\cos^{-1}\frac{(2r)^2 - r_1^2 - r_2^2}{2r_1 r_2}, \tag{7.2}$$

where r is the tool radius, r_1 and r_2 are the effective radii for cutting edge # 1 and # 2, respectively.

As can be deducted from the Eq. 7.2, the change in spacing angle is a function of initial tool radius. With the smaller tool radii, higher deviations are expected. Fig 7.11 shows how the tooth spacing angles change with respect to radial throw and its orientation for three different tool sizes. As expected, the deviation in tooth spacing angle for small tool diameters such as 50.8 μm can reach up to 120 degs, compared to only 12 deg. for a tool diameter of 508 deg. As a result of this deviation, the orientation of cutting geometry is severely affected. Among the affected geometries, the changes in rake angle and the side clearance angle length should now be considered in process planning. The significant changes in the tooth spacing angle causes rake angle for one cutting edge to decrease, and the same amount of increase to other cutting edge. This can cause significant differences in material removal mechanism, cutting forces and tool life [79]. Also, depending on the feed rates and tool cross-section profile, the work-piece can engage with cutting tools in locations other than cutting edges (flank face etc). Although this contact does not occur on created side surfaces, the generated contact forces can cause additional tool deflection etc. and can also lead to cutting forces being misinterpreted.

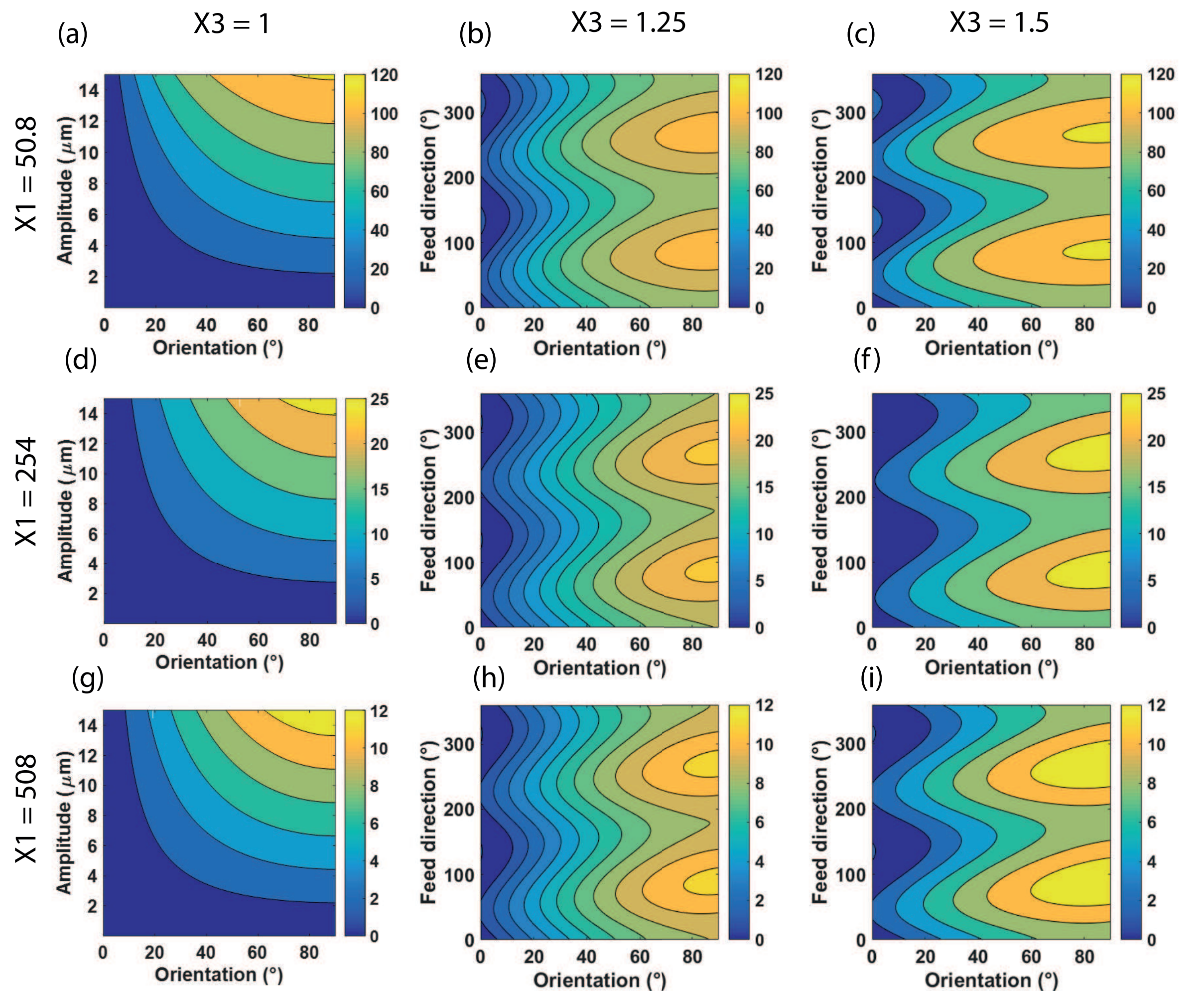

Figure 7.11: *The variation in the tooth-spacing angle for (a) varying magnitude and orientation for a circular trajectory, and (b)-(c) varying radial throw orientation and feed direction for an elliptical ratio of 1.25 and 1.5, respectively. The rows present data for different tool diameters. Note the difference in legend amplitudes. The unit is μm.*

7.4 Measurement Results from Chapter 4

To understand the effects of radial throw measured in Section 4.3.2, we considered a two-dimensional (2D) tool model where we considered only a single "slice" of a two-fluted microtool (or, a zero-helix microtool) with 254 μm diameter. For this simulation, the radial throw parameters calculated in Chapter 4 are used. In addition to directly using the measure radial throw orientation, considering the possibility of dictating the radial throw orientation (as discussed in Chapter 4, Section 4.5, Fig. 4.6), we used not only the measured value but also 45 degrees less than the measured value. Since tool-geometric errors are unknown, the tool is assumed to be ideal for the purpose of this simulation.

Fig. 7.12(a) presents the variation of SLE with spindle speed. As expected, following the increase in radial throw with increased spindle speed, the SLE also increases considerably with the spindle speed. An increase in feed rate was seen to slightly reduce the SLE; however, this is merely due to the way in which the SLE is calculated. An increase in feed rate causes the cusp height to increase while not affecting the maximum channel width, and since the SLE is calculated as the average width of the channel, increased feed rate causes an apparent reduction in SLE. Another very important observation is that the radial throw orientation has a significant effect on SLE. Indeed, a change in radial throw orientation by 45 degrees causes the radial throw to more than double for every speed. This also highlights the importance of being able to dictate the radial throw orientation. However, a deeper cut with non-zero helix angle will reduce the impact of radial throw angle for the entire channel, as the effect of radial throw at the cutting points will change at different depths.

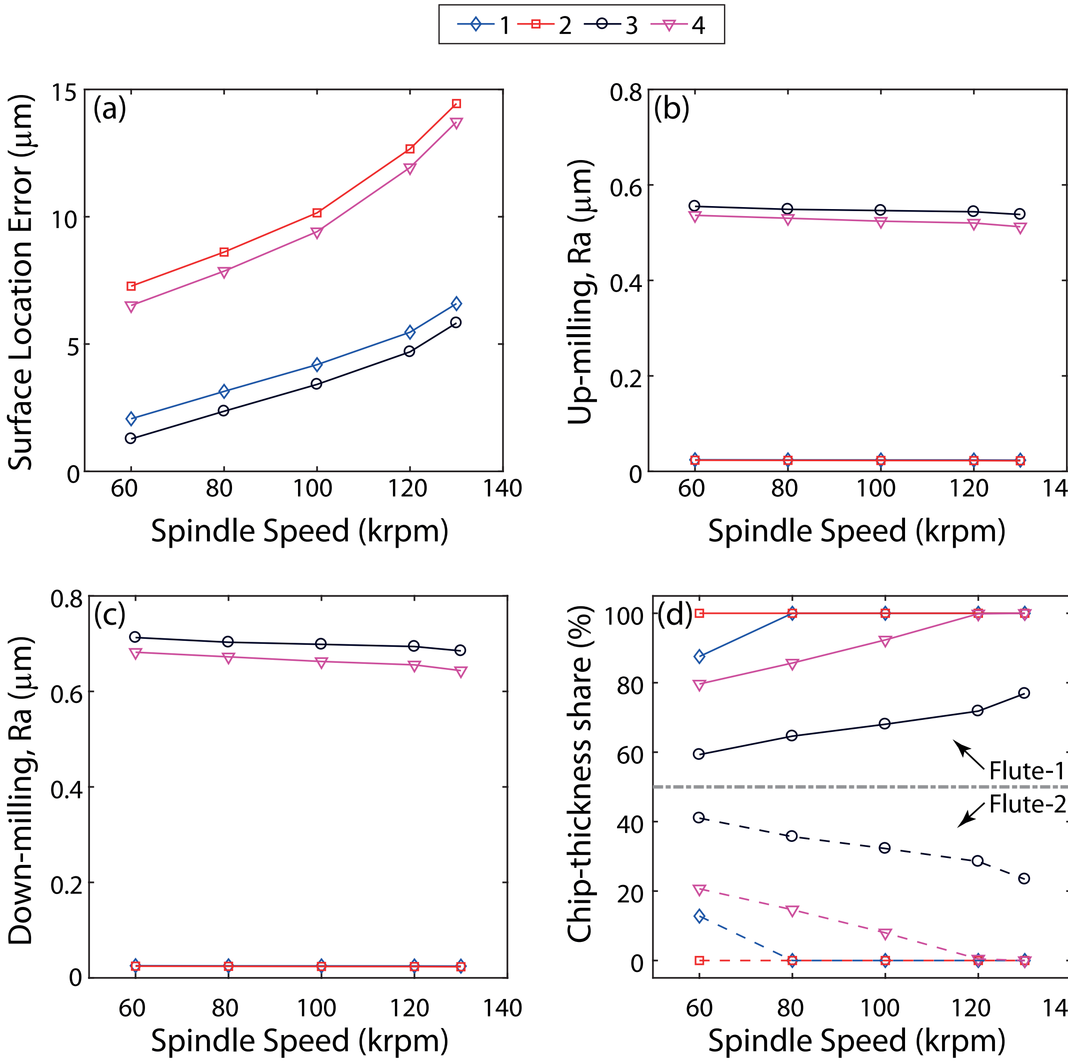

Figure 7.12: *Effect of measured radial throw on (a) Surface Location Error (SLE), (b) up-milling sidewall surface roughness, (c) down-milling sidewall surface roughness, and (d) chip-thickness share. The feeds for 1&2 and 3&4 are 5µm/flute and 25µm/flute, respectively. The radial throw orientations for 1&3 and 2&4 are measured values and measured values - 45 deg., respectively.*

The sidewall surface roughness (R_a) values for the up-milling and down-milling sides are given in Figs. 7.12(b)-(c). As expected, the surface roughness increases strongly with the feed rate, and increased spindle speed (and hence increased radial throw magnitude) induces a slight decrease in sidewall surface roughness. This is due to a small decrease in cusp height is obtained at higher radial throw magnitudes. Due to the non-symmetric tool-tip trajectory, the up-milling side has a lower surface roughness value than the down-milling side has. The effect of radial throw orientation on sidewall surface roughness was seen to be less than 5%.

To assess the effect of radial throw parameters on uncut chip thickness, a *chip-thickness share* is defined as the ratio of maximum chip thickness (in the presence of radial throw) to twice the feed rate. As such, in the absence of radial throw, each of the two cutting edges would have a chip thickness share of 50%. Figure Fig. 7.12(d) shows the change in the chip-thickness share for each of the two cutting edges with spindle speed for two different feed rates. For the feed rate of 5 μm, which is smaller than any of the measured radial throw magnitude, and for the measured radial throw orientation, only one of the cutting edges (100% chip-thickness share) was seen to participate in cutting for speeds above 60 krpm. At 60 krpm, the measured radial throw orientation of 78 deg. causes both cutting edges to engage into the material. When the radial throw orientation is shifted by 45 degrees, for 5 μm feed rate, only a single cutting edge is involved in cutting for *any* speed mainly due to the increase in radial throw magnitude. This is an expected result, since the measured radial throw magnitudes exceed the feed rate, and if the radial throw orientation is such that the radial throw is aligned with one of the cutting edges, only that cutting edge removes material. The smaller the feed rate and the larger the radial throw, the higher will be the non-symmetry in uncut chip thickness between the cutting edges. For the larger feed rate of 25 μm, which is larger than any of the measured radial throw magnitude, for the measured radial throw parameters, both cutting edges engage in cutting, although at different chip-thickness shares. The variation in chip-thickness share in this case is dominated by the change in radial throw orientation (see Fig. 4.8(c)). The closer is the radial throw orientation to 90 degrees (which was seen at lower speeds, e.g., 78 deg. at 60 krpm), the more symmetric is the participation of the two cutting edges (i.e., the chip-thickness share is closer to 50%). When the radial throw orientation is shifted (reduced) by 45 degrees, the small radial throw orientation angles at 120 krpm and 130 krpm causes only one of the cutting edges to participate in the cutting.

7.5 Summary and Conclusions

This chapter presented a three-dimensional time-domain kinematic simulation of the microcutting process, specifically focusing on micromilling. The simulation effectively contrasts between the circular vs elliptical nature of radial throw trajectory as well as shows the effect of radial throw amplitude and orientation on the micro-machining quality parameters. The trochoidal trajectory is generated with Eq. 7.1. The experimental matrix consisted of varying tool diameter, feed rates, radial throw forms, radial throw magnitude and orientation. The effects on various quality parameters such as surface location error, peripheral surface roughness as well as uncut chip thickness and tooth-spacing angles are comprehensively discussed. In addition, the effect of measured parameters from the radial throw measurements presented in Chapter 4 are also discussed. The following specific conclusions can be drawn from this chapter

- The dimensional errors (or SLE) increases when the radial throw magnitude increases and radial throw orientation decreases. For elliptical forms of radial throw, the SLE can vary as much as 6 μm (or 50%) as the feed direction is varied form 0 deg. to 90 deg. The larger the tool diameter, the lesser the variation in the SLE.

- The peripheral (sidewall) surface roughness immensely depend on the feed rate and tool diameter used in cutting. For circular radial throw form, a larger effective radii results in a smaller roughness. However, for elliptical forms, the effective radii changes with in a revolution and therefore, a generalized argument cannot be established.

- The uncut chip thickness is highly dependent on the feed rate and the radial throw magnitude and its orientation. For a circular form, as the radial throw orientation deviates from 90 degs., the participation of one of the cutting edges increases which leads to uneven tool wear. And for an elliptical form, at a fixed radial throw magnitude and orientation, a variation of up to 50% in uncut chip thickness is observed across feed directions. These results show the importance of studying the radial throw magnitude, orientation and form in understanding the micro-milling process output.

- The tooth-spacing angle is linearly correlated with the tool diameter used for cutting. For a circular form, the deviation in the tooth-spacing angle increases as the radial throw orientation approaches 90 degs. The trends are similar for an elliptical form where for a fixed radial throw orientation, the deviation in the tooth-spacing angle can change by up to 50%. It is interesting to note the competing effects in SLE vs deviation in tooth-spacing angle as the radial throw orientation is varied.

- The 2D simulations (with measured values from Chapter 4) indicated the importance of determining the radial throw orientation with respect to the cutting edges of the tool. A change in the orientation by 45 degs. caused the surface location error (SLE) to more than double at each speed. The simulation also predicted the chip-thickness share experienced by each of the cutting flutes which directly affects the process output such as machining force signatures and tool wear.

CHAPTER 8

Conclusions

8.1 Summary and Conclusions

This thesis aimed at improving the process accuracy and reproducibility of micromachining processes. Measurement and analysis tools were developed to characterize the non-ideal motions of the micro-tool tip when it is rotated using ultra-high-speed (UHS) spindles. These non-ideal motions deviate the trajectory of the cutting edge from the ideal trajectory, and, therfore directly contribute to the dimensional error and surface roughness. Furthermore, the non-ideal motions alter the uncut chip thickness experienced by the cutting edges. These non-ideal motions arise from geometric errors of the micro-tools; imperfect interfaces within the tool-collet-spindle assembly (resulting in setup errors); manufacturing errors of the spindle (imperfect bearings, non-straightness of the spindle shaft); the errors of the spindle under loading from the cutting processes; and vibrations caused by the system components or environmental effects.

To enable high quality measurements to characterize non-ideal motions, a new spindle-metrology testbed was designed to reduce the noise and vibrations and their in influence on the measurements, thereby reducing the uncertainties of the LDV-based measurement technique. The developed measurement and analysis technique was then used to study the effects of radial loading and moment arm on the various components of radial throw: fundamental (or one-per-rev), synchronous error motions and asynchronous error motions. Next, the tool-geometric errors such as (1) the non-straight tool-axis, (2) variation in the tool-diameter, and (3) inaccuracy in the location of cutting edges were explored using a rotary stage and precision (kinematic) setups in conjunction with focus variation microscopy (FVM) techniques. Lastly, the changes in the tool-tip trajectory arising from radial throw was studied on the surface location errors (SLE), peripheral (sidewall) surface roughness and the variations in the uncut chip thickness using a time-domain simulation, representing the kinematics of the micromilling process. The effect of various parameters associated with radial throw, such as the magnitude, orientation, form, were studied for a variety of feed rates and tool diameters.

Based on the work presented in this thesis, the following conclusions are obtained:

- The experimental technique and the associated mathematical framework presented in this thesis enable accurate determination of the radial throw (of the tool axis) at any axial position, as well as of the trajectory of the cutting points in the presence of radial throw. Run-out measurements cannot capture the dynamic, rotation-angle-dependent motions of the cutting points.

- The mathematical framework can be used to obtain the trajectory of any point along the cutting edges in the presence of radial throw. The framework uses a vectorial formulation and requires measurements of radial throw at two axial locations along the tool shank in two mutually-perpendicular directions to determine the trajectory of the cutting points. This framework allowed straightforward addition of tool-geometric errors, which could contribute considerably to the radial throw at the tool-tip. An LDV-based experimental approach was developed to obtain both the magnitude and orientation of radial throw.

- The overall trajectory of radial throw was found to be elliptical, rather than circular, at some spindle speeds. This behavior was hypothesized to arise from the axi-asymmetry in spindle/bearing structure and the associated non-symmetric dynamic response. The FRF magnitudes obtained along the two-axes using impact testing have confirmed this hypothesis. The radial throw orientation was found to be dictated by the defects coming from the rotor (spindle), and the contribution of the collet and the tool towards orientation was found to be inconsequential.

- For the particular UHS spindle used in this work, under loaded conditions at varying levels of load, and irrespective of the moment arm, the fundamental component of the spindle motions shows marginal or no increase due to loading. On the other hand, the synchronous spindle error motions are found to increase by more than 200% depending on both he magnitude of applied radial force and the moment arm (which varies the applied moment). The 1σ of the asynchronous spindle error motions were found to be affected by the change in radial forces at a fixed moment arm (up to 15%). The asynchronous spindle error motions stays relatively constant when the moment arm is varied.

- The use of focus-variation microscopy along with a low-precision rotary stage resulted in inaccurate measurement of the microtool geometries. As an alternative method, axis-offset at the tool-tip was determined by using two parallel class-XX gage-pins, which provided a reference axis of rotation for measurements (accuracy better than 1 μm). The preliminary data indicated that this alternative method could enable accurate measurement of microtool geometries using FVM.

- In general, the magnitude, orientation and the form of radial throw had an immense effect on the output of the micromachining process. The peripheral surface roughness is found to be highly dependent on the feed rate and tool diameter. At small feed rate, the surface roughness does not vary appreciably with radial throw. The orientation of radial throw was found to dictate the chip share between the two cutting flutes. Even for the same orientation in an elliptical form, the feed direction caused up to 50% variation in the uncut chip thickness. These simulations indicated the importance of determining the radial throw magnitude as well as orientation with respect to the cutting edges of the tool.

8.2 Research Output

The following research articles and conference proceedings were published as a result of this thesis (in chronological order):

1. Nahata, S., Onler, R., Shekhar, S., Korkmaz, E. and Ozdoganlar, O.B., "Radial Throw in Micromachining: Measurement and Analysis." *Precision Engineering*, 2018.

2. Nahata, S., Onler, R., Korkmaz, E. and Ozdoganlar, O.B.,"Radial Throw at the Cutting Edges of Micro-Tools When Using Ultra-High-Speed Micromachining Spindles." *Proceedings of NAMRI/SME*, Vol. 46, 2018. (*Accepted*)

3. Nahata, S., Onler, R. and Ozdoganlar, O.B., "Experimental investigation of radial throw in miniature spindles used for micromachining." *International conference on micromanufacturing (ICOMM)*, Milan, Italy, March 2015.

4. Nahata, S. and Ozdoganlar, O.B., "Application of magnets in loading ultra-high-speed spindles and understanding its effects on radial spindle error motions." *ASPE Annual Meeting*, St. Paul, Minnesota, Oct. 2013.

5. Nahata, S., Anandan, K.P. and Ozdoganlar, O.B., "LDV-based Spindle Metrology for Ultra-High-Speed Micromachining Spindles." *Proceedings of NAMRI/SME*, Vol. 41: 319-324, 2013.

The following articles are in the pipeline for submission/publication:

1. Nahata, S., Onler, R. and Ozdoganlar, O.B., "Radial Throw in Micromilling: The Effects on Surface Location Error, Sidewall Surface Roughness and Uncut Chip Thickness." *2nd World Congress on Micro and Nano Manufacturing* (*Submitted*)
2. Nahata, S. and Ozdoganlar O.B., "Effect of external loading on radial throw when using UHS micromachining spindles." (*in Preparation*)
3. Nahata, S., Shekhar, S. and Ozdoganlar O.B., "A Simplified Dynamic Model to Predict Spindle-Speed Dependent Radial Throw at the Tool-tip." (*in Preparation*)
4. Nahata, S., Onler, R. and Ozdoganlar O.B., "The Effect of Radial Throw on the Kinematics and Quality of the Features fabricated by Micromilling" (*in Preparation*)
5. Nahata, S., Onler, R. and Ozdoganlar O.B., "Geometric errors of Micro-Tools: Measurement and Analysis." (*in Preparation*)

CHAPTER 9

Future Work

9.1 Understanding the effect of overhang length on radial throw

The overhang length of the tool is known to have a significant effect on the resulting radial motions, as indicated by the previous work from the Ozdoganlar group [24]. Overhang length generally varies by the type of the tool used for micromachining . A long-reach tool will have a longer overhang length than a standard tool. The overhang length could affect the effective unbalance in the system which changes the dynamic response of the system.

To assess the effect of artifact over-hang length, tests using four different artifact lengths (5 mm, 10 mm, 15 mm, and 20 mm from the collet) will be performed. In each case, the length of the artifact inside the collet will be kept constant. The measured data will be analyzed to determine the effect of artifact over-hang length on synchronous and asynchronous components of the radial, axial, and tilt error motions.

9.2 Effect of dynamic loading on radial throw

The static loading was found to significantly affect the synchronous spindle error motions. Likewise, it is interesting to observe the effects of dynamic loading on the various component of radial throw. This requires a method to apply non-contact dynamic loading to the spindle via test artifacts.

As a preliminary work, a custom dynamic loading artifact is designed and fabricated. It consists of a 3.175 mm diameter neodymium disc magnet is attached to the 3.175 mm class-Xx gage-pin. This magnet is magnetized diametrically which means that left-half face of the disc is North-Pole and the other half is South-Pole. To generate dynamic forces, another permanent magnet, cylindrically shaped, is placed perpendicular to the axis-of-rotation of the artifact, maintaining a finite air-gap (g) with the magnetic-tip. This cylindrical magnet is axially magnetized with North-Pole (or South-Pole) facing the artifact (as shown in Figure 9.1). As the artifact rotates, it constantly changes the poles w.r.t. to the radial magnet which causes a cycle of attraction-repulsion-attraction and so on. This creates dynamic forces with a frequency corresponding to the spindle rotational speed. This force was measured with the help of dynamic load cell and is presented in Figure 9.2. At an air-gap of $\sim$200 μm, peak-to-peak force amplitude of 4 N at spindle rotational frequency was generated with this method.

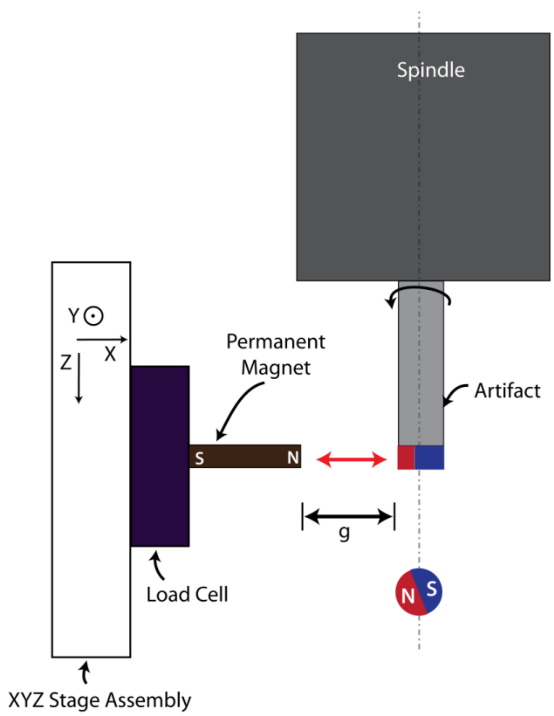

Figure 9.1: *Dynamic loading artifact, consisting of disc magnet magnetized diametrically, is used to generate dynamic forces at spindle rotational frequency.*

The dynamic loading artifact described above provides us with the appropriate magnitude of forces but it is locked at the spindle rotational frequency. This is due to the presence of two poles which can produce only one sine per revolution. In order to obtain dynamic forces twice the frequency of the spindle rotational frequency (representative of the two-fluted cutting tool), a multi-pole magnet is designed and fabricated.

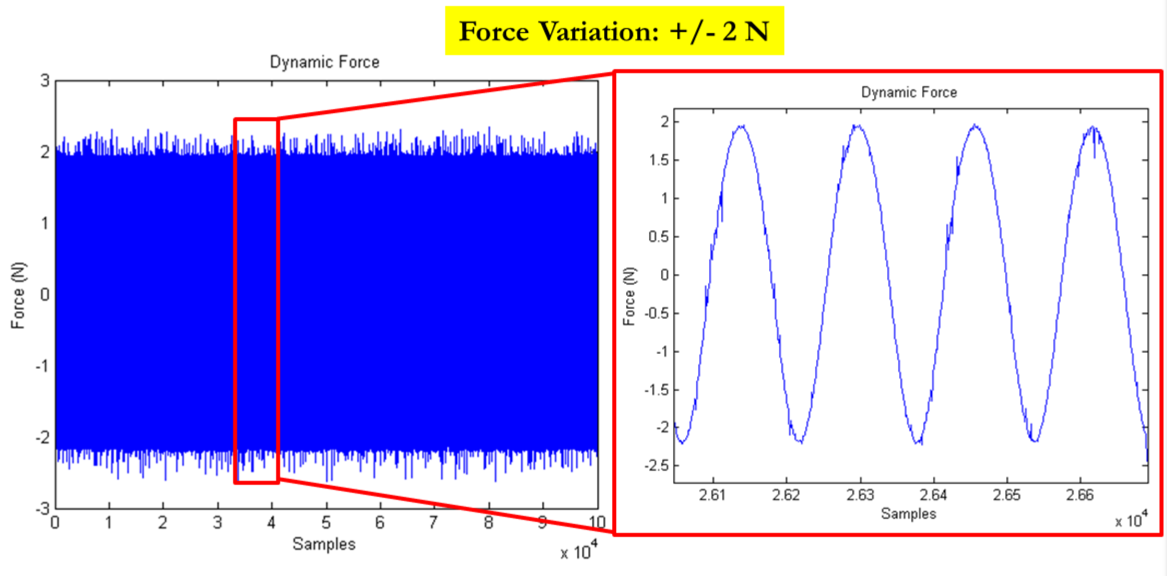

Figure 9.2: *Dynamic force of ±2 N is generated by using dynamic loading artifact in an arrangement shown in Fig. 9.1.*

9.2.1 Multi-pole magnet for dynamic loading

In order to make the forcing frequency twice the spindle rotational frequency, a multi-pole magnet is designed which consists of multiple North and South poles. Figure 9.3(a)-(b) explains the construction of such a magnet.

The multi-pole magnet was assembled from four different 90 deg. arc sections which were custom manufactured by SuperMagnetMan.net. Two of the sections were having North-pole on their arcs and vice-versa for the other two. They were arranged in alternating fashion as shown in Figure 9.3(b). The whole multi-pole magnet assembly is then attached to the step-artifact (5 mm diameter) through glue. The physical setup of the multi-pole magnet in trial experimentation is shown in Figure 9.3(c). For each revolution, both the North-pole and South-pole of the artifact interacts twice with the North-pole of stationary magnet (attached to the loading setup). This creates alternating forces with frequency twice the rotational frequency.

The force output is shown in Figure 9.4 below for an air-gap of $\sim$500 μm. The presence two sine waves in each revolution demonstrate forces at twice the rotational frequency. The variation in the amplitude is possibly due to the misalignment of the axis of multi-pole magnet w.r.t. the axis of the step-artifact. Using this setup, we are able to generate forces with peak-to-peak amplitude of 1 N. In future, experiments will be conducted to assess the variation of spindle error motion under dynamic loading.

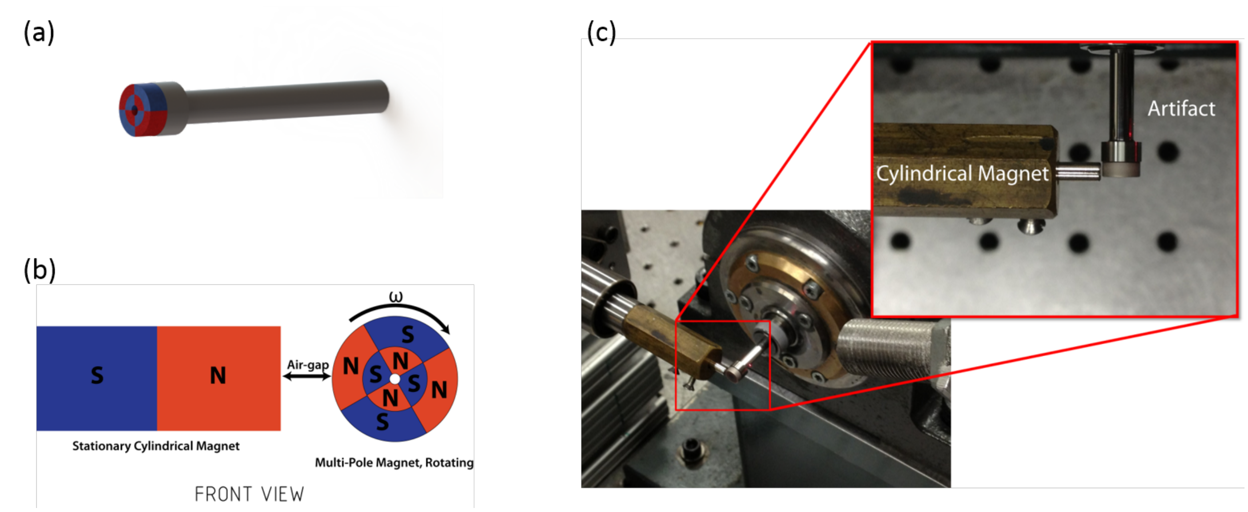

Figure 9.3: *(a) Multi-pole magnet with N-S-N-S poles on the outer circumference attached to the step-artifact, (b) Multi-pole magnet (rotating) along with cylindrical magnet (stationary) used for generating dynamic forces with twice the spindle rotational frequency, and (c) Dynamic loading artifact consisting of multi-pole magnet attached to the step-artifact.*

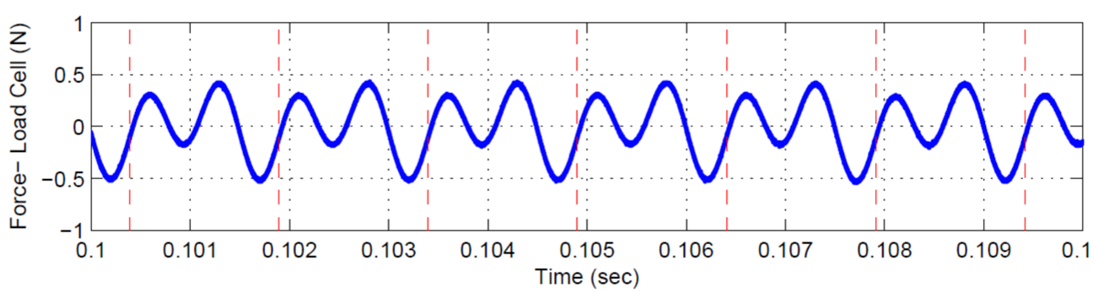

Figure 9.4: *Dynamic force output from the multi-pole magnet at an air-gap of ∼500 μm. Red-dash lines represent start/end of a revolution.*

9.3 A comprehensive assessment of tool-geometric errors

Tool-geometric errors can be as large as the tool-attachment errors. As tool-geometric errors directly affect the motions at the tool-tip, it is therefore important to measure and quantify these errors. These errors particularly consists of the non-straight tool-axis, variability in the tool diameter and inaccuracies in the position of the cutting edges. To this end, initial work using focus variation based microscopy is presented in Chapter 6. More research is needed to validate the presented approach and devise superior approaches towards accurate measurement of tool-geometric errors. The specific objectives of this work are:

- To develop novel measurement approaches and post-processing techniques, using focus variation microscopy (FVM), to quantify the non-straightness tool-axis in 3D.

- To demonstrate the measurement approach by conducting a statistical analysis on the geometric errors of a set of commercial microtools from the same batch.

Bibliography

[1] M A Camara, J C Campos Rubio, A M Abrão, and J P Davim. State of the art on micromilling of materials, a review. *Journal of Materials Science & Technology*, 28(8):673–685, 2012. (Cited on page 1.)

[2] D. Dornfeld, S. Min, and Y. Takeuchi. Recent advances in mechanical micromachining. *CIRP Annals - Manufacturing Technology*, 55(2):745–768, 2006.

[3] Bekir Bediz, Emrullah Korkmaz, Rakesh Khilwani, Cara Donahue, Geza Erdos, Louis D. Falo, and O. Burak Ozdoganlar. Dissolvable microneedle arrays for intradermal delivery of biologics: Fabrication and application. *Pharmaceutical Research*, 31(1):117–135, 2014.

[4] Jonelle Z. Yu, Emrullah Korkmaz, Monica I. Berg, Philip R. LeDuc, and O. Burak Ozdoganlar. Biomimetic scaffolds with three-dimensional undulated microtopographies. *Biomaterials*, 128:109–120, 2017. (Cited on page 1.)

[5] Sinan Filiz, Caroline M. Conley, Matthew B. Wasserman, and O. Burak Ozdoganlar. An experimental investigation of micro-machinability of copper 101 using tungsten carbide micro-endmills. *International Journal of Machine Tools and Manufacture*, 47(7-8):1088–1100, 2007. (Cited on page 2.)

[6] Emrullah Korkmaz, Emily E. Friedrich, Mohamed H. Ramadan, Geza Erdos, Alicia R. Mathers, O. Burak Ozdoganlar, Newell R. Washburn, and Louis D. Falo. Therapeutic intradermal delivery of tumor necrosis factor-alpha antibodies using tip-loaded dissolvable microneedle arrays. *Acta Biomaterialia*, 24:96–105, 2015. (Cited on page 2.)

[7] IBAG. HT 45 S 140 user manual, 2011. (Cited on pages 2, 30, and 67.)

[8] Gong Yadong. Tool tip trajectories investigation and its influences in micromilling operation. *2008 3rd IEEE International Conference on Nano/Micro Engineered and Molecular Systems*, pages 440–445, 2008. (Cited on pages 2 and 9.)

[9] Kiha Lee and David A Dornfeld. A study of surface roughness in the micro-end-milling process. *Laboratory for Manufacturing and Sustainability*, 2004. (Cited on pages 3 and 94.)

[10] ISO. ISO 230-7 (2015): Test code for machine tools - Geometric accuracy of axes of rotation. 2015. (Cited on pages 3, 5, 7, 8, 33, 35, 51, 63, and 68.)

[11] Xiaodong Lu, Arash Jamalian, and Richard Graetz. A new method for characterizing axis of rotation radial error motion: Part 2. Experimental results. *Precision Engineering*, 35(1):95–107, 2011. (Cited on pages 3, 4, and 8.)

[12] Bekir Bediz, B. Arda Gozen, Emrullah Korkmaz, and O. Burak Ozdoganlar. Dynamics of ultra-high-speed (UHS) spindles used for micromachining. *International Journal of Machine Tools and Manufacture*, 87:27–38, 2014. (Cited on pages 3, 9, 28, and 47.)

[13] Cha Bum Lee, Rui Zhao, and Seongkyul Jeon. A simple optical system for miniature spindle runout monitoring. *Measurement: Journal of the International Measurement Confederation*, 102:42–46, 2017. (Cited on pages 4 and 10.)

[14] Eric R. Marsh and Shinji Shimizu. Precision Spindle Metrology,. *Journal of Manufacturing Science and Engineering*, 130(3):036501, 2008. (Cited on page 5.)

[15] Aerotech Inc. Rotary Stage Terminology, 2012. (Cited on page 8.)

[16] S. M. Afazov, S. M. Ratchev, and J. Segal. Modelling and simulation of micro-milling cutting forces. *Journal of Materials Processing Technology*, 210(15):2154–2162, 2010. (Cited on pages 9 and 59.)

[17] Y. Altintas and X. Jin. Mechanics of micro-milling with round edge tools. *CIRP Annals - Manufacturing Technology*, 60(1):77–80, 2011. (Cited on page 96.)

[18] Emel Kuram and Babur Ozcelik. Multi-objective optimization using Taguchi based grey relational analysis for micro-milling of Al 7075 material with ball nose end mill. *Measurement: Journal of the International Measurement Confederation*, 46(6):1849–1864, 2013.

[19] Erman Gözü and Yiit Karpat. Uncertainty analysis of force coefficients during micromilling of titanium alloy, 2017. (Cited on page 9.)

[20] Keith a. Hekman and Steven Y. Liang. In-process monitoring of end milling cutter runout. *Mechatronics*, 7(1):1–10, 1997. (Cited on page 9.)

[21] Mohammad Malekian, Simon S. Park, and Martin B G Jun. Modeling of dynamic micro-milling cutting forces. *International Journal of Machine Tools and Manufacture*, 49(7-8):586–598, 2009. (Cited on pages 9 and 59.)

[22] Wasawat Nakkiew, Chi Wei Lin, and Jay F. Tu. A new method to quantify radial error of a motorized end-milling cutter/spindle system at very high speed rotations. *International Journal of Machine Tools and Manufacture*, 46(7-8):877–889, 2006. (Cited on page 9.)

[23] Xinyu Liu, Martin B G Jun, Richard E DeVor, and Shiv G Kapoor. Cutting mechanisms and their influence on dynamic forces, vibrations and stability in micro-endmilling. In *ASME 2004 International Mechanical Engineering Congress and Exposition*, pages 583–592. American Society of Mechanical Engineers, 2004. (Cited on page 10.)

[24] K. Prashanth Anandan and O. Burak Ozdoganlar. Analysis of error motions of ultra-high-speed (UHS) micromachining spindles. *International Journal of Machine Tools and Manufacture*, 70:1–14, jul 2013. (Cited on pages 10, 28, 31, 36, 42, and 116.)

[25] Martin B Jun, Richard E DeVor, and Shiv G Kapoor. Investigation of the Dynamics of Microend MillingPart II: Model Validation and Interpretation. *Journal of Manufacturing Science and Engineering*, 128(4):901–912, 2006. (Cited on pages 10 and 88.)

[26] K.Prashanth Anandan, Abhinandan S. Tulsian, Alkan Donmez, and O.Burak Ozdoganlar. A Technique for measuring radial error motions of ultra-high-speed miniature spindles used for micromachining. *Precision Engineering*, 36(1):104–120, jan 2012. (Cited on pages 10, 36, 68, 78, and 79.)

[27] R Ryan Vallance, Eric R. Marsh, and Philip T Smith. Effects of Spherical Targets on Capacitive Displacement Measurements. *Journal of Manufacturing Science and Engineering*, 126(4):822–829, 2005. (Cited on page 11.)

[28] Philip T. Smith, R. Ryan Vallance, and Eric R. Marsh. Correcting capacitive displacement measurements in metrology applications with cylindrical artifacts. *Precision Engineering*, 29(3):324–335, 2005. (Cited on page 11.)

[29] K Prashanth Anandan and O Burak Ozdoganlar. A multi-orientation error separation technique for spindle metrology of miniature ultra-high-speed spindles. *Precision Engineering*, 43:119–131, 2016. (Cited on pages 11, 12, 51, 54, 62, and 80.)

[30] Eric R Marsh, David A Arneson, and Donald L Martin. A comparison of reversal and multi-probe error separation. *Precision engineering*, 34(1):85–91, 2010. (Cited on pages 11 and 54.)

[31] Kengo Fujimaki and Kimiyuki Mitsui. Radial error measuring device based on auto-collimation for miniature ultra-high-speed spindles. *International Journal of Machine Tools and Manufacture*, 47(11):1677–1685, 2007. (Cited on page 12.)

[32] Hiroshi Murakami, Akio Katsuki, and Takao Sajima. Simple and simultaneous measurement of five-degrees-of-freedom error motions of high-speed microspindle: Error analysis. *Precision Engineering*, 38(2):249–256, 2014. (Cited on page 12.)

[33] H F F Castro. A method for evaluating spindle rotation errors of machine tools using a laser interferometer. *Measurement*, 41(5):526–537, 2008. (Cited on page 12.)

[34] Eric Marsh and Robert Grejda. Experiences with the master axis method for measuring spindle error motions. *Precision Engineering*, 24(1):50–57, jan 2000. (Cited on pages 12, 13, and 51.)

[35] A . K. Sharma. Investigation into Spindle Error Motions using a Modified Loading Device. In *ASPE Annual Meeting Annual Meeting*, pages 1–4, 1999. (Cited on page 13.)

[36] ASME. B89.3.4 - Axes of Rotation: Methods for Specifying and Testing. Technical report, 2010. (Cited on page 13.)

[37] Panart Khajornrungruang, Keiichi Kimura, Keisuke Suzuki, and Tomoki Inoue. Micro tool diameter monitoring by means of laser diffraction for on-machine measurement. *International Journal of Automation Technology*, 11(5):736–741, 2017. (Cited on page 14.)

[38] JA Doyle. *Analysis and comparison of metrology methods for quantifying micro-endmills*. Bachelor's thesis, MIT, 2009. (Cited on page 14.)

[39] R Ryan Vallance, Chris J Morgan, Shelby M Shreve, and Eric R Marsh. Micro-tool characterization using scanning white light interferometry. *Journal of Micromechanics and Microengineering*, 14(8):1234–1243, aug 2004. (Cited on pages 14 and 86.)

[40] N Loychik, M Barraja, A Khan . . . of the ASME . . . , and Undefined 2006. Mechanical design of a precision instrument for measuring the roundness profiles of micro shafts. *ebooks.asmedigitalcollection.asme . . . .* (Cited on page 14.)

[41] M Barraja, RR Vallance, N Loychik, ER Marsh Proceedings of the 21st . . . , and Undefined 2006. DESIGN AND EVALUATION OF A PROTOTYPE INSTRUMENT FOR MEASURING ROUNDNESS PROFILES OF MICRO SHAFTS. *ASPE Annual Meeting*, 2006. (Cited on page 14.)

[42] F Helmli, R Danzl, and S Scherer. Optical Measurement of Micro Cutting Tools. *Journal of Physics: Conference Series*, 311:012003, aug 2011. (Cited on pages 14 and 15.)

[43] Sudhanshu Nahata, K Prashanth Anandan, and O Burak Ozdoganlar. LDV-based Spindle Metrology for Ultra-High-Speed Micromachining Spindles. In *Proceedings of NAMRI/SME*, volume 41, pages 2–7, 2013. (Cited on pages 16 and 54.)

[44] S. Nahata and O.B. Ozdoganlar. Application of magnets in loading ultra-high-speed spindles and understanding its effects on radial spindle error motions. In *Proceedings of the 28th Annual Meeting of the American Society for Precision Engineering, ASPE*, 2013.

[45] Sudhanshu Nahata, Recep Onler, and O.Burak Ozdoganlar. Experimental investigation of radial throw in miniature spindles used for micromachining. In *International conference on micromanufacturing (ICOMM)*, 2015.

[46] Sudhanshu Nahata, Recep Onler, Emrullah Korkmaz, and O Burak Ozdoganlar. Radial Throw at the Cutting Edges of Micro-Tools When Using Ultra-High-Speed Micromachining Spindles. In *Transactions of the North American Manufacturing Research Institution of SME*, 2018.

[47] Sudhanshu Nahata, Recep Onler, Shivang Shekhar, Emrullah Korkmaz, and O Burak Ozdoganlar. Radial throw in micromachining: Measurement and analysis. *Precision Engineering*, 2018.

[48] Sudhanshu Nahata, Recep Onler, and O Burak Ozdoganlar. Radial Throw in Micromilling: The Effects on Surface Location Error, Sidewall Surface Roughness and Uncut Chip Thickness. In *World Congress on Micro and Nano Manufacturing*, 2018. (Cited on page 16.)

[49] Castinite. (Cited on page 18.)

[50] Tom Irvine. Damping properties of materials revision c. *Ratio*, 3:3–8, 2004. (Cited on page 19.)

[51] Byron Knapp and Dave Arneson. Dynamic characterization of a micro-machining spindle. In *International conference on micromanufacturing (ICOMM), No. 108*, 2014. (Cited on page 28.)

[52] K. Prashanth Anandan and O. Burak Ozdoganlar. An LDV-based methodology for measuring axial and radial error motions when using miniature ultra-high-speed (UHS) micromachining spindles. *Precision Engineering*, 37(1):172–186, jan 2013. (Cited on pages 29, 54, and 62.)

[53] Polytec. Polytec OFV-5000. (Cited on page 29.)

[54] Christophe Leys, Christophe Ley, Olivier Klein, Philippe Bernard, and Laurent Licata. Detecting outliers: Do not use standard deviation around the mean, use absolute deviation around the median. *Journal of Experimental Social Psychology*, 49(4):764–766, 2013. (Cited on page 37.)

[55] W. Y. Bao and I. N. Tansel. Modeling micro-end-milling operations. Part II: Tool run-out. *International Journal of Machine Tools and Manufacture*, 40(15):2175–2192, 2000. (Cited on page 42.)

[56] Bekir Bediz, Emrullah Korkmaz, and O. Burak Ozdoganlar. An impact excitation system for repeatable, high-bandwidth modal testing of miniature structures. *Journal of Sound and Vibration*, (13):2743–2761, 2014. (Cited on page 47.)

[57] Min Chen and Carl R Knospe. Control approaches to the suppression of machining chatter using active magnetic bearings. *IEEE Transactions on control systems technology*, 15(2):220–232, 2007. (Cited on page 52.)

[58] Matti Rantatalo, Jan-Olov Aidanpää, Bo Göransson, and Peter Norman. Milling machine spindle analysis using FEM and non-contact spindle excitation and response measurement. *International Journal of Machine Tools and Manufacture*, 47(7-8):1034–1045, jun 2007. (Cited on page 52.)

[59] Atsushi Matsubara, Taku Yamazaki, and Shinya Ikenaga. Non-contact measurement of spindle stiffness by using magnetic loading device. *International Journal of Machine Tools and Manufacture*, 71:20–25, aug 2013. (Cited on page 52.)

[60] Xiaopeng Wang, Yuzhu Guo, and Tianning Chen. Measurement research of motorized spindle dynamic stiffness under high speed rotating. *Shock and Vibration*, 2015, 2015. (Cited on page 52.)

[61] Robert R Donaldson. SIMPLE METHOD FOR SEPARATING SPINDLE ERROR FROM TEST BALL ROUNDNESS ERROR. 1972. (Cited on page 54.)

[62] Chris J Evans, Robert J Hocken, and W Tyler Estler. Self-calibration: reversal, redundancy, error separation, and absolute testing'. *CIRP Annals-Manufacturing Technology*, 45(2):617–634, 1996. (Cited on page 54.)

[63] Wei Gao, Satoshi Kiyono, and Tadatoshi Nomura. A new multiprobe method of roundness measurements. *Precision Engineering*, 19(1):37–45, 1996. (Cited on page 54.)

[64] G X Zhang, Y H Zhang, S M Yang, and Z Li. A multipoint method for spindle error motion measurement. *CIRP Annals-Manufacturing Technology*, 46(1):441–445, 1997. (Cited on page 54.)

[65] Robert Grejda, Eric Marsh, and Ryan Vallance. Techniques for calibrating spindles with nanometer error motion. *Precision engineering*, 29(1):113–123, 2005. (Cited on page 54.)

[66] D J Whitehouse. Some theoretical aspects of error separation techniques in surface metrology. *Journal of Physics E: Scientific Instruments*, 9(7):531, 1976. (Cited on page 54.)

[67] Steven Cappa, Dominiek Reynaerts, and Farid Al-Bender. A sub-nanometre spindle error motion separation technique. *Precision Engineering*, 38(3):458–471, 2014. (Cited on pages 54 and 55.)

[68] COMSOL. *AC/DC Module User's Guide*. 2013. (Cited on page 57.)

[69] Wikipedia. Maxwell Stress Tensor, 2016. (Cited on page 58.)

[70] Thomas A. Dow, Edward L. Miller, and Kenneth Garrard. Tool force and deflection compensation for small milling tools. *Precision Engineering*, 28(1):31–45, 2004. (Cited on pages 59 and 67.)

[71] Fausto Fiorillo. Measurements of magnetic materials. *Metrologia*, 47(2), 2010. (Cited on page 60.)

[72] GUM:2008. Evaluation of measurement data Guide to the expression of uncertainty in measurement. Technical report, 2008. (Cited on page 77.)

[73] Robert D Grejda. Use and calibration of ultraprecision axes of rotation with nanometer level metrology. 2004. (Cited on page 79.)

[74] Marposs <https://www.marposs.com/eng/application/technologies-laser-systems-for-tool-setting>. (Cited on page 82.)

[75] R Leach. *Fundamental principles of engineering nanometrology*. 2014. (Cited on pages 83 and 84.)

[76] Dariusz Janecki and Jaroslaw Zwierzchowski. A method for determining the median line of measured cylindrical and conical surfaces. *MEASUREMENT SCIENCE AND TECHNOLOGY*, 26(8), 2015. (Cited on pages 84 and 85.)

[77] WP SYAM. *Uncertainty evaluation and performance verification of a 3D geometric focus-variation measurement*. PhD thesis, Politicano Di Milano, 2015. (Cited on pages 90 and 93.)

[78] Tony L. Schmitz, Jeremiah Couey, Eric Marsh, Nathan Mauntler, and Duke Hughes. Runout effects in milling: Surface finish, surface location error, and stability. *International Journal of Machine Tools and Manufacture*, 47(5 SPEC. ISS.):841–851, 2007. (Cited on page 94.)

[79] Yusuf Altintas. *Manufacturing automation: metal cutting mechanics, machine tool vibrations, and CNC design*. Cambridge university press, 2012. (Cited on page 107.)